

Medizinische Klinik und Poliklinik IV
Ludwig-Maximilians-University Munich
Director: Prof. Dr. med. Martin Reincke

**3D IMAGING AND ANALYSIS OF HUMAN MESENCHYMAL STEM
CELLS AND CYTOTOXIC T LYMPHOCYTES INVADING TUMOR
SPHEROIDS**



Dissertation to obtain the Doctorate in Natural Sciences
at the Faculty of Medicine
Ludwig-Maximilians-University Munich

Submitted by
Svenja Rühland
from Hamburg

2018

**With permission of the Faculty of Medicine
Ludwig-Maximilians-University Munich**

Supervisor: Prof. Dr. rer. nat. Peter Jon Nelson

Co-supervisor: Prof. Dr. rer. nat. Elfriede Nößner

Dean of the faculty: Prof. Dr. med. dent. Reinhard Hickel

Date of submission 28.08.2018

First examiner Prof. Dr. rer. nat. Peter Jon Nelson

Second examiner Prof. Dr. rer. nat. Christian Ries

Date of oral examination: 10.01.2019

To my family

Content

Content	4
1 Summary	1
2 Zusammenfassung	3
3 Introduction	5
3.1 Cell-based tumor therapies	5
3.1.1 Tumor characteristics and hurdles for therapy	5
3.1.2 Mesenchymal stem cells	6
3.1.3 Cytolytic T lymphocytes.....	10
3.2 Multicellular tumor spheroids.....	15
3.2.1 Three dimensional cell culture	15
3.2.2 Spheroid culture techniques	15
3.2.3 Spheroids as <i>in vitro</i> tumor models.....	16
3.2.4 Analysis of three dimensional spheroids.....	18
3.3 Objectives of this thesis.....	22
4 Material.....	23
4.1 Antibodies.....	23
4.2 Cell Culture	23
4.2.1 Blood and human bone marrow samples	23
4.2.2 Primary cells.....	23
4.2.3 Cell lines	25
4.2.4 Media, supplements and others	26
4.2.5 Plasmids.....	27
4.3 Consumables and equipment	28
4.3.1 Consumables.....	28
4.3.2 General laboratory equipment	29
4.3.3 Microscopes.....	29
4.3.4 Computing server.....	30

4.3.5	Software	31
4.4	Reagents, buffers and kits.....	31
4.4.1	Reagents.....	31
4.4.2	Buffers.....	33
4.4.3	Kits.....	33
5	Methods.....	34
5.1	Cell culture techniques.....	34
5.1.1	Cultivation of cell lines and primary cells	34
5.1.2	Freezing and thawing of cells.....	34
5.1.3	Counting of cells.....	34
5.1.4	Isolation and engineering of primary hBMSCs.....	34
5.1.5	Isolation and engineering of primary human T cells	35
5.2	The Invasion Assay protocol.....	36
5.2.1	Spheroid generation.....	36
5.2.2	MSC labeling.....	36
5.2.3	MSC application and invasion.....	37
5.2.4	CTL labeling, application and invasion	37
5.2.5	Sample mounting, SPIM imaging and data processing	38
5.2.6	Analysis – cytoplasmic or nuclear single cell segmentation	38
5.3	HSV-TK expression	41
5.3.1	Immunohistochemistry on monolayer	41
5.3.2	Cryosectioning.....	41
5.3.3	Immunohistochemistry on cryosections	41
5.4	Other functional assays.....	42
5.4.1	Migration Assay	42
5.4.2	Live imaging of CTL-target interaction and Ca ²⁺ signaling.....	43
5.4.3	Standard assays to assess CTL activity.....	44
5.5	Flow cytometry analysis of SkMel23 cells.....	45

5.6	Statistical analysis	46
6	Results.....	47
6.1	Invasion assay – establishing a method for the quantification of the tumor invasion potential of therapeutic cells	47
6.2	MSCs’ invasion potential into tumor spheroids is dependent on culture conditions.....	51
6.2.1	Activation of primary MSCs with expanded culturing under standard cell culture conditions	51
6.2.2	Variability of invasive behavior between different donors and sources of MSCs	52
6.2.3	Conventional migration assays support source-dependent differences in the ability of MSCs to respond to tumor-derived signals.....	54
6.2.4	DMEM culture medium with FCS enhances the invasion potential of primary MSCs into experimental tumors.....	57
6.2.5	Continuously cultured and freshly thawed MSCs show similar invasion into tumor spheroids	58
6.2.6	Viral transduction of MSCs enhances their invasion potential.....	59
6.3	RANTES-induction in engineered MSCs within the tumor spheroid milieu.....	61
6.4	Effect of low and high avidity TCRs and chimeric co-stimulatory receptors on T cell invasion and tumor cell killing in a melanoma spheroid model.....	64
6.4.1	Effect of TCR avidity on CTLs’ response to tumor cells	64
6.4.2	Effect of chimeric co-stimulatory receptors on T cell function in 3D spheroid models.....	74
7	Discussion	81
7.1	Spheroids and their capacity as <i>in vitro</i> tumor model	81
7.2	Therapeutic mesenchymal stem cells – optimal pre-conditioning for effective tumor homing	84
7.2.1	Assays to analyze MSC recruitment to tumor sites	84
7.2.2	Biologic mechanisms underlying MSC recruitment to tumor sites.....	85
7.2.3	Pre-conditioning and growth conditions can enhance MSC homing and tumor infiltration	86
7.3	Assessing CTL activity <i>in vitro</i>	89
8	Conclusion.....	94

Content

9	Abbreviations.....	95
10	References	99
11	Appendix.....	113
11.1	Fiji macros and workflow for SPIM data processing.....	113
11.2	Fiji macros and workflow for invasion assay analysis	119
11.2.1	Cytoplasmic segmentation of MSC clusters.....	119
11.2.2	Nuclear segmentation of single MSCs	123
11.2.3	Cytoplasmic segmentation of single CTLs	126
11.3	MSC attachment to tumor spheroids depends on tumor cell line	131
11.4	Effect of thyroid hormones and tetrac on MSC invasion into tumor spheroids	132
11.5	Effect of chimeric co-stimulatory constructs on CTL cytotoxicity in SKMel23 spheroids – single experiments	133
	Curriculum Vitae.....	134
	Publications.....	135
	Acknowledgements	136
	Affidavit	137

1 Summary

Due to their innate tumor homing properties mesenchymal stem cells (MSCs) are being evaluated as potential vehicles for the targeted delivery of therapy genes deep into solid tumors. For successful therapeutic effects, engineered MSCs are required to home to and extensively infiltrate into tumor environments. To help facilitate the characterization of MSC bioactivity, a novel assay was established to quantify their tumor invasive potential *in vitro*. In this system, spheric cell aggregates, called spheroids, were generated from established tumor cell lines that then served as an invasion matrix for modeling the physiology of intervascular tumor microregions. Selective plane illumination microscopy (SPIM) was applied to image the three-dimensional distribution of MSCs within the spheroid after invasion. A strategy was developed for the automated quantification of their invasion characteristics following the pre-labeling of MSCs with a cell tracker dye. The method makes use of segmentation algorithms to detect single cells and the determination of the shortest distance of each MSC to the spheroid surface.

The invasion assay was then used to characterize diverse aspects of MSC-based biology in the context of experimental tumor infiltration. Primary human bone-marrow derived MSC invasion into hepatocellular carcinoma cell (HUH7) spheroids revealed no effect of freezing and thawing of the MSCs directly prior to their application, but an increasing effect of genetic retroviral modification on tumor spheroid invasion was found. Whereas MSCs isolated under same conditions displayed little inter-donor variances, a significant variability was detected between MSCs derived from different tissue sources. Moreover, a deeper invasion of MSCs isolated and cultured under standard cell culture conditions as compared to good manufacturing practice (GMP) protocols was found.

The general concept of immuno-oncology includes a cell-based tumor therapy where the adoptive transfer of CD8⁺ T cells or cytotoxic T lymphocytes (CTLs) expressing T cell receptors (TCRs) that recognize tumor associated antigens are applied to specifically eliminate cancer cells. Naturally occurring anti-tumor CTLs often are too weak to persist and operate within the immune-suppressive tumor micromilieu. Enhanced TCR binding affinity, resulting in so called high avidity T cells, has been linked to improved CTL function, but the overall functional significance of this in physiologic settings is a matter of contention.

Expanding the potential use of the invasion assay, CTL migration into experimental spheroids was studied and the potential effect of TCR avidity for tumor antigens on the invasive potential was analyzed. To this end, a set of primary human CTLs were analyzed for their invasive capacity into experimental melanoma SKMel23 cell spheroids. Unspecific CTLs, or CTLs engineered with either a low or a high avidity TCR for the melanoma associated antigen tyrosinase were compared. Invasion

into the tumor spheroids was shown to be specificity-dependent, but avidity-independent. While unspecific, mock transduced CTLs did not migrate deeply into SKMel23 spheroids, both low and high avidity TCR CTLs were found to deeply infiltrate the spheroids within 24 h.

Established cytotoxicity assays such as the chromium release assay, are well applied standard assays for CTL function. It is now clear, however, that they generally reflect somewhat artificial parameters. The use of the spheroid invasion assay was expanded to assess the CTL anti-tumor response in a more physiological context, with regards to spatial distribution, cellular interaction and microenvironmental influences. Higher functional responses of high avidity TCR CTLs were observed, with a complete tumor spheroid dissociation after 6 d. In addition, the surface expression of the clinically relevant and often targeted CTL inhibitor PD-L1 was found to be up-regulated in the melanoma cell line SKMel23 when cultured in 3D spheroids, but not in conventional 2D monolayer culture. This allowed the SKMel23 spheroids to be used as a suitable model system to further characterize a set of novel chimeric receptors (PD-1:28 and PD-1:BB) with regards to their potential effect on enhanced tumor killing. These constructs were generated using the extracellular domain of PD-1 and fusing it to the intracellular domains of CD28 or 4-1BB. This was done as an attempt to turn the normal PD-L1 mediated CTL inhibition seen into a potential activation. Using the spheroid invasion assay, an upgrading effect by these chimeric constructs of low avidity TCR CTLs to levels of high avidity TCR CTLs could be demonstrated *in vitro* on unmodified SKMel23 cells for the first time.

2 Zusammenfassung

Aufgrund ihrer Eigenschaft, spezifisch zu Tumoren zu wandern, werden mesenchymale Stammzellen (MSCs) als potientes Transportvehikel für Therapiegene gesehen, die diese tief in solide Tumore einbringen sollen. Therapeutische Effektivität setzt einen starken Tumortropismus und eine hohe Tumordinfiltration durch MSCs voraus. Um die Charakterisierung der biologischen Aktivität von MSCs zu erleichtern wurde hier ein neuer Assay etabliert, der ihr Tumordinvasionspotential *in vitro* quantifizieren soll. Dazu wurden aus etablierten Tumorzelllinien kugelförmige Zellaggregate generiert, sogenannte Sphäroide, die die Physiologie intervaskularer Tumor-Mikroregionen modellieren und hier als Invasionsmatrix dienen. Die Lichtblatmikroskopie erlaubte dann die Abbildung der dreidimensionalen Verteilung der MSCs im invadierten Sphäroid. Für die Auswertung wurde eine automatische Quantifizierungsstrategie der Invasionscharakteristika entwickelt, die durch eine vorherige Markierung der MSCs mit einem Zelltracker Farbstoff ermöglicht wurde. Diese Strategie basiert auf Segmentierungsalgorithmen, die Einzelzellen detektieren, und der Bestimmung der kürzesten Distanz jeder MSC zur Sphäroidoberfläche.

Mit Hilfe dieses Invasionsassays wurden verschiedene Aspekte der MSC-Biologie untersucht mit Hinblick auf ihr Infiltrationsverhalten in experimentelle Tumore. Einfrieren und unmittelbares Auftauen vor der Anwendung von primären humanen, aus dem Knochenmark isolierten MSCs zeigten keinen Effekt hinsichtlich ihres Invasionspotentials in Leberkarzinomzell (HUH7)-Sphäroide. Im Gegensatz dazu wurde ein erhöhtes Invasionspotential nach genetischer retroviraler Modifikation der MSCs festgestellt. Während unter gleichen Bedingungen isolierte MSCs eine geringe Varianz innerhalb verschiedener Spender zeigten, wurde ein signifikanter Unterschied festgestellt zwischen MSCs, die aus verschiedenen Geweben isoliert wurden. MSCs zeigten eine tiefere Invasion, wenn sie unter Standard-Zellkulturbedingungen isoliert und kultiviert wurden, verglichen mit Zellen, die unter "good manufacturing practice" (GMP-) Konditionen gewonnen wurden.

Der Begriff der Immunonkologie beinhaltet einen zellbasierten Ansatz, bei dem der adoptive Transfer von CD8⁺ T-Zellen oder cytotoxischen T-Lymphozyten (CTLs), die Tumor-assoziierte Antigen erkennende T-Zellrezeptoren (TCRs) exprimieren, Krebszellen spezifisch eliminieren soll. Natürlich vorkommende anti-Tumor-CTLs sind oft zu schwach, um im immunsuppressiven Tumormikromilieu zu bestehen und zu wirken. Erhöhte TCR-Bindeaffinität, die in so genannte hoch-afide T-Zellen resultiert, konnte mit verbesserter CTL Funktion in Verbindung gebracht werden, wobei deren letztendliche funktionale Bedeutung in einem physiologischen Umfeld umstritten ist.

Unter Ausweitung des Anwendungsfeldes des Invasionsassays wurde die Migration von CTLs in experimentelle Sphäroide untersucht sowie der mögliche Effekt der TCR-Avidität gegen

Tumorantigene auf das Invasionspotential. Dazu wurde ein Satz primärer humaner CTLs auf ihr Invasionsvermögen in experimentelle Melanomzell(SKMel23)-Sphäroide hin charakterisiert. Verglichen wurden unspezifische CTLs und CTLs, die entweder mit einem niedrig- oder einem hoch-aviden TCR gegen das Melanoma-assoziierte Antigen Tyrosinase ausgestattet wurden. Die Invasion in Tumorsphäroide zeigte sich als abhängig von der Spezifität, aber unabhängig von der Avidität. Unspezifische, mock-transduzierte CTLs wanderten nicht tief in SKMel23-Sphäroide ein, wohingegen sowohl niedrig- als auch hoch-avide TCR-CTLs innerhalb von 24 Stunden tief in die Sphäroide infiltrierten.

Etablierte Cytotoxizitätsassays wie der Chrom-Release-Assay sind gut etablierte Standardassays für die CTL Funktionalität, wobei inzwischen klar ist, dass sie im Allgemeinen eher artifizielle Parameter simulieren. Die Anwendung des Sphäroid-Invasionsassays wurde auf die Erfassung der anti-Tumor-Antwort von CTLs in einem physiologischeren Kontext ausgedehnt, mit Hinblick auf räumliche Verteilung, zelluläre Interaktion und mikroregionale Einflüsse. Beobachtet wurde eine höhere funktionale Antwort von hoch-aviden TCR-CTLs, mit einer kompletten Auflösung der Sphäroide nach 6 Tagen. Außerdem wurde festgestellt, dass die Oberflächenexpression des klinisch relevanten und oft adressierten CTL-Inhibitors PD-L1 auf der Melanomzelllinie SKMel23 hochreguliert war, wenn die Zellen in 3D Sphäroiden kultiviert wurden, nicht aber in konventioneller 2D Monolayer-Kultur. Dies erlaubte es, die SKMel23-Sphäroide als geeignetes Modellsystem zu verwenden, um einen Satz neuer chimärer Rezeptoren (PD-1:28 und PD-1:BB) hinsichtlich ihres potentiellen Effekts einer verstärkten Tumorzellabtötung zu charakterisieren. Die entsprechenden Konstrukte wurden generiert, indem die extrazelluläre Domäne von PD-1 mit der intrazellulären Domäne von CD28 oder 4-1BB fusioniert wurde, in einem Versuch, die normale PD-L1 vermittelte CTL Inhibition in eine potentielle Aktivierung umzukehren. Mit dem Sphäroid-Invasionsassay konnte eine Steigerung des Effekts niedrig-avider TCR-CTLs durch diese chimären Konstrukte auf ein Level hoch-avider TCR-CTLs demonstriert werden, und zwar das erste Mal *in vitro* gegen unmodifizierte SKMel23 Zellen.

3 Introduction

3.1 Cell-based tumor therapies

3.1.1 Tumor characteristics and hurdles for therapy

After heart disease, cancer represents the second most common cause of death worldwide with 8.8 million deaths recorded in 2015. DNA mutations, in a background defined by genetic predispositions, are generated by physical (e.g. ultraviolet radiation), chemical (e.g. tobacco smoke components) or biological (e.g. hepatitis and human papilloma virus infections) carcinogens. These factors accumulate and eventually lead to transformation of normal cells into malignant tumor cells. These cells grow rapidly, invade healthy tissue and metastasize to other organs, the latter being the major cause of death from cancer (WHO 2018).

Cancer treatment is complicated as it requires an attack on the body's own cells – targeting degenerated tumor cells, while sparing healthy tissues. Although there are phenotypes that are dominant or even exclusive for tumor cells, there's also a vast heterogeneity between cancer types as well as constant cancer cell evolution over progressing stages of tumor growth.

Classic cancer therapies include the surgical resection of solid tumors and locally restricted radiation therapy, both of which are ineffective as soon as tumor cells metastasize. Chemotherapies address cancer more systemically by attacking rapidly proliferating cells, a hallmark of tumor cells. Unfortunately, this growth characteristic is also seen in some healthy tissues including skin, hair, intestine and bone, and thus, the side effects of this systemic therapy can be severe.

Research is constantly striving to develop more effective and targeted therapeutics for cancer patients. To this end, analysis of tumor-associated tissue composition has revealed two potential allies in the fight against cancer:

- First, tumor homing mesenchymal stem cells (MSCs) that are employed as vehicles for the targeted delivery of therapy agents to tumor environments,

and

- second, anti-tumor cytolytic T lymphocytes (CTLs) that allow using the immune system itself as the most sophisticated defense system to selectively target cancer cells.

When compared to the potential of chemotherapy drugs, cell-based therapeutics are much more complex to handle. However, their more selective and efficient mode of action makes them excellent candidates in the strategic battle against cancer.

3.1.2 Mesenchymal stem cells

3.1.2.1 Biological and medicinal characteristics

The Greek term “mesenchyme” means “middle infusion” and describes the ability of mesenchymal cells to migrate to, and fill, the space between the ectodermal and endodermal layer in early embryonic development. These essential characteristics allow these cell types to play a relevant role during wound repair (Caplan 1991).

Mesenchymal stem cells - also referred to as marrow stromal cells - are adult stem cells with a multilineage potential, which are linked to tissue homeostasis and repair.

There are a variety of tissue sources of MSCs, and diverse culture conditions for their propagation have been described. Importantly, no individual marker can distinctively define them. To address this issue, the International Society of Cell Therapy (ISCT) has released a set of minimal criteria to define “multipotent mesenchymal stromal cells” in scientific and clinical studies (Dominici et al. 2006). These criteria include:

- MSCs are plastic-adherent when maintained in standard culture conditions.
- MSCs express cluster of differentiation (CD) 105, CD73 and CD90, and lack expression of hematopoietic CD45, CD34, CD14 or CD11b, CD79 α or CD19 and human leukocyte antigen – antigen D related (HLA-DR) surface molecules.
- MSCs can differentiate into osteoblasts, adipocytes and chondroblasts *in vitro*.

While originally described in bone marrow, MSCs are also present in perivascular cell populations throughout the body, and can be easily and rapidly culture-expanded *in vitro*, for example, from adipose tissue or umbilical cord blood (Crisan et al. 2008; Kern et al. 2006; Colter et al. 2000).

MSCs can specifically home to sites of injury, where they replace damaged tissue cells and support tissue repair via facilitating neovascularization and immunomodulatory paracrine stimulation (Gojo et al. 2003; Qi et al. 2014). They are thought to differentiate into adipocytes, osteocytes, chondrocytes and myocytes, as well as hepatocytes, endothelial cells, cardiomyocytes, and even neural cells (Chen et al. 2016; Barry and Murphy 2004; Chivu et al. 2009; Tao et al. 2016; Sanchez-Ramos et al. 2000).

What makes them especially applicable in the context of allogeneic transplantation is their general lack of immunogenicity: MSCs can escape T cell recognition due to low levels of MHC I, rare expression of MHC II, and a lack of the co-stimulatory molecules CD40, CD40L, CD80 and CD86 required for T cell activation (Tse et al. 2003; Chamberlain et al. 2007). Although there is still a chance for T cells to detect nonself MSCs via weakly expressed MHC I complex, they won't get activated

without further co-stimulation (see 3.1.3.3). For example, injecting allogeneic MSCs into a humanized immune mouse model did not evoke the immune responses that were seen upon allogeneic blood cell or fibroblast injections (Lee et al. 2014).

The first stem cell transplantations – transfer of hematopoietic stem cells (HSCs) in leukemia patients – was successfully performed over 45 years ago (Storb 2012). In the past few years, also the utilization of MSCs has gained ground, with currently > 800 ongoing clinical trials being conducted worldwide for a wide range of indications (NIH. U.S. National Library of Medicine 2018).

When transplanted together with HSCs in leukemia patients, MSCs can support hematopoietic cell engraftment, and act as immune suppressive agents (Lazarus et al. 2005). These immunomodulatory characteristics in MSCs have been used to reduce graft-versus-host disease and suppress autoimmune diseases, such as multiple sclerosis, where they also help in the regeneration of damaged neural tissue (Le Blanc et al. 2004; Bai et al. 2009; Yamout et al. 2010). Due to their osteogenic and chondrogenic differentiation potential, MSC transplants have been successfully used to repair bone defects or osteonecrosis (Quarto et al. 2001; Gangji et al. 2004). In vascular repair, MSCs have been shown to traffic to damaged heart tissue and to prevent myocardial scarring after infarction, as well as to help drive angiogenesis in critical limb ischemia (Maione et al. 2013; Williams et al. 2011).

3.1.2.2 Mesenchymal stem cells in tumor therapy

Tumors have been described to act like “wounds, that do not heal” (Flier et al. 1986). In that, they produce factors that help drive a constant tissue repair-like process including the mobilization and recruitment of MSCs. Indeed, both endogenous as well as adoptively applied MSCs have been shown to migrate to solid tumors and metastasis in brain, colon, liver, and skin (Nakamizo et al. 2005; Shinagawa et al. 2010; Niess et al. 2011; Wang et al. 2014).

The homing mechanisms for MSC recruitment to tumor settings are thought to be similar to those at work during leukocyte recruitment towards sites of injury, and include: Recruitment, deceleration/rolling and firm arrest on the vascular surface, which is then followed by their transmigration across the endothelium, also called extravasation (Karp and Leng Teo 2009).

Recruitment is mediated by gradients of chemokines such as stromal cell-derived factor (SDF)-1 that is secreted by inflamed or tumor tissues, and the corresponding CXC chemokine receptor (CXCR) type 4 expressed on MSCs (Zhuang et al. 2009). The arrest and extravasation of MSCs is further driven by adhesion molecules like the integrin $\alpha 4\beta 1$ heterodimer (Very Late Antigen (VLA)-4) that binds vascular cell adhesion molecule (VCAM)-1 on endothelial cells (Rüster et al. 2006).

Accordingly, the tumor homing capacity of MSCs has been shown to be improved by respective pre-conditioning *in vitro*, such as proinflammatory cytokine stimulation resulting in the upregulation of chemokine receptors like CXCR4, or by transient genetic modification, for example with $\alpha 4$ integrin (Shi et al. 2007; Fan et al. 2012; Kumar and Ponnazhagan 2007).

MSCs are thought to act as stromal progenitor cells in tumor microenvironments. Tumors depend on a close interaction with surrounding tumor stroma to persist and proliferate. Tumor stroma and its physiological contained cells are therefore cancer supporting factors. Indeed, MSCs differentiate into carcinoma-associated fibroblasts (CAFs), stimulating angiogenesis and malignant growth (Orimo et al. 2005). By chemokine (C-C motif) ligand (CCL) 5 secretion, MSCs have been shown to also promote metastasis in experimental models (Karnoub et al. 2007). Moreover, they may deregulate the anti-tumor immune response (Djouad et al. 2003).

Because of their tumor-specific homing and differentiating properties, however, it is possible to employ MSCs to treat cancer. In a Trojan horse-like approach, they are used as vehicles for the targeted delivery of anti-cancer therapies deep into tumor environments. Oncolytic viruses loaded into MSCs, for example, have been shown to more efficiently target tumor sites as when injected directly into the body (Komarova et al. 2006; Hammer et al. 2015).

Also single molecule based therapeutics often suffer from a short half-life and low stability when administered systemically. Genetic modifications of MSCs that allow continuous production of transgenic proteins, following their recruitment to tumors, have shown efficacy in diverse tumor models. For example, the immune stimulatory effects of interleukin (IL)-2, and the anti-proliferative effects of interferon (IFN)- β , when expressed by MSCs at tumor sites have been used to effectively reduce tumor growth (Stagg et al. 2004; Studeny et al. 2002). MSCs engineered to express growth factor antagonists such as the hepatocyte growth factor antagonist NK4, or pro-apoptotic proteins including tumor necrosis factor-related apoptosis induced ligands (TRAIL), have also shown positive results in various preclinical models (Kanehira et al. 2007; Reagan et al. 2012).

An additional layer of therapeutic control can be delivered by transgenic proteins that do not counteract tumor cells themselves, but enzymatically activate a co-administered prodrug in the vicinity of the tumor setting. One of the most widely applied of such suicide gene systems makes use of the herpes simplex virus thymidine kinase (HSV-TK) gene, that encodes for an enzyme that activates the prodrug ganciclovir (GCV), or similar guanine analogues, through phosphorylation to their monophosphate form. Endogenous kinases then activate the agent to triphosphate guanine analogues that inhibit DNA strand elongation which finally leads to cellular apoptosis (Moolten 1986;

Rangel-Sosa et al. 2017). The HSV-TK/GCV system has been tested successfully in a series of anti-cancer gene therapy approaches, and has been shown to be effective in killing not only the HSV-TK expressing cells, but also adjacent “bystander” cells (Mesnil and Yamasaki 2000). Niess et al. transfected MSCs with this suicide gene (Niess et al. 2011). In an *in vivo* mouse model they observed a significant therapeutic effect on hepatocellular carcinoma growth upon MSC recruitment to tumors.

An additional level of tumor-selectivity has been achieved through the use of tissue or signal specific gene promoters that are used to drive MSC transgene expression (Bao et al. 2012). One approach has linked transgene expression to the response of MSCs to tumor derived signals. Activating therapeutic transgenes through specific differentiation-linked gene promoters ensures that the adoptively applied MSCs express the transgene only after their arrival and integration at tumor sites. In their study, Niess et al. successfully used the inflammatory cytokine induced gene promoter of CCL5/RANTES (regulated on activation, normal T cell expressed and secreted) to limit HSV-TK expression to liver tumors, and prevent expression in tissues that are potential normal targets of MSCs (e.g. skin, gut, secondary lymphatics, etc.) (Niess et al. 2011). This promising approach has progressed to the stage of phase I/II clinical trials, with phase I having been completed successfully (Niess et al. 2015; Einem et al. 2017).

3.1.3 Cytolytic T lymphocytes

3.1.3.1 *The immune system*

The immune system ensures the integrity of our body by protecting us against foreign intruders and harmful disease.

From birth on, the innate immune system stands on guard, providing an immediate defense against infectious agents. It protects via epithelial barriers, components like inflammatory cytokines, and cellular leukocytes: macrophages and granulocytes, which engulf pathogens and natural killer (NK) cells, which can lyse infected cells. In addition, dendritic cells (DCs) patrol through tissues and collect and present peptides on their major histocompatibility complex (MHC) molecules. As professional antigen presenting cells (APCs), DCs mirror the antigenic composition of the body.

Upon migration to secondary lymphoid organs, and their presentation of potential pathogenic, nonself peptides to T cells, DCs act as central players in the activation of the adaptive immune system. Upon induction, the adaptive immune system creates a complex, antigen-specific response. It can also generate a memory, and thus an adaptation towards previously encountered pathogens. This ensures a fast and effective response in case of secondary infections. The adaptive immune system is composed of three main types of cells: antibody producing B cells, CD4⁺ T cells, which regulate the immune response via stimulatory and inhibitory cytokines, and CD8⁺ T-cells, that exert besides cytokine secretion also direct cytolytic activity (Murphy and Weaver 2017).

3.1.3.2 *Cytolytic T lymphocytes - hit men of the immune system*

CD8⁺ T cells, or cytolytic T lymphocytes, identify and kill targets with high specificity. This selective process occurs via their individual T cell receptors (TCRs). T cells mature within the thymus, where the TCR repertoire becomes selected. Each TCR is generally composed of an α - and a β -chain with variable regions that determine its specificity and MHC restriction. As is seen for antibodies, the enormous repertoire of TCRs is created via the random V(D)J recombination of genes encoding for variable (V), diversity (D) and joining (J) segments.

TCRs recognize nonself peptides presented on MHC class I surface proteins (**Figure 1**). Virtually every somatic cell expresses MHC I molecules on its cell surface. Bound to these are peptides that have been processed from cytoplasmic proteins. Thus, cells can be identified as either normal, or as infected or degenerated cells by the immune system. In humans, a series of MHC I proteins are individually encoded by human leukocyte antigen (HLA) genes.

During their maturation in the thymus, T cells are positively selected for TCRs that recognize endogenous MHC I molecules. In addition, to avoid auto-immune reactions, they further undergo negative selection against TCRs that bind self-peptides too strongly.

Mature, but still naïve, CD8⁺ T cells migrate to secondary lymphoid organs such as lymph nodes, where they encounter APCs. T cells can become activated when their TCRs bind cognate peptide-MHC complexes. They subsequently proliferate and differentiate into effector T cells. The now activated cells leave the secondary lymphatics and migrate through the body, and as “hit men” of the immune system, search for, and attack their targets: cells that express the appropriate peptide-MHC I complex (Murphy and Weaver 2017).

In the course of target elimination, the CD8⁺ T cells release inflammatory cytokines, including interleukin (IL)-2, interferon (IFN)- γ and tumor necrosis factor (TNF)- α that condition the general immune milieu, and most importantly, induce apoptosis of the target cells. The latter is conducted via Fas ligand - when the respective receptor is present on the target cell - or by delivery of cytotoxins. CTLs form an immunological synapse on target cells towards which they transport lytic granules. These granules contain cytotoxic enzymes that are released into the synaptic cleft: i) perforin that opens pores in the target cell's membrane resulting in influx of Ca²⁺, and ii), granzyme B that enters the cell and activates caspases (Murphy and Weaver 2017).

3.1.3.3 Regulation of cytolytic T lymphocytes

Immunological processes need to be tightly controlled to be effective, but safe. In the CTL response a series of regulatory mechanisms are seen.

The strength of the CD8⁺ T cell response is directly correlated to the strength or avidity of TCR binding. Avidity can be seen as the sum of the binding affinities of multiple TCRs expressed on a T cell, and the peptide-MHC I complexes on the target cell. Although high avidity TCRs have a proven enhanced response against targets, a mixture of low, intermediate and high avidity TCR CTLs is thought to ensure effective and persistent target elimination over the course of disease. It has been proposed that a too high TCR avidity may result in a deleterious or ineffective T cell activity and is possibly depleted naturally (Viganò et al. 2012).

The overall control of CTL activity is based on the integration of a series of receptors that induce either stimulatory or inhibitory signal cascades. A wide repertoire of co-stimulatory and co-inhibitory receptors is thought to help guide T cell action and effector function in different stages (Chen and Flies 2013). In addition to TCR-mediated antigen recognition, co-stimulatory signals are needed to activate CTLs in the first place and have to be constantly provided for ongoing CTL function. APC expressed ligands such as CD80 and CD86 stimulate CTL receptors including CD28. This leads to a T cell that becomes fully effective, as opposed to tolerant or anergic. Both naïve and active T cells, however, also express a set of inhibitory receptors. Cytolytic T lymphocyte associated protein (CTLA)-4, for example, is a competitive homologue of CD28 that counterbalances the early activation of naïve CD8⁺ T cells,

which makes a more stringent set of signals necessary to achieve effector function (Krummel and Allison 1995). Another inhibitor is the programmed cell death protein-1 (PD-1) receptor that is expressed on active CTLs to further control their action (Freeman et al. 2000). The PD-1 ligand PD-L1 is expressed on various cell types including APCs and some tumor cells. Signaling through the PD-1 receptor can block CTL effector activity. These various receptors and ligands that are able to inhibit and terminate a raising T cell response are called “immune checkpoints”.

3.1.3.4 Cytolytic T lymphocytes used for tumor therapy

In addition to pathogenic nonself antigens, T cells are also able to identify cancerous cells. This is possible due to mutation derived or highly overexpressed proteins in the cancer cells, or, for example, to the re-expression of proteins normally associated with development. These are collectively referred to as tumor associated antigens (TAAs). Tumor infiltrating lymphocytes (TILs) including T cells are found in many solid tumors (Hadrup et al. 2013). Successfully growing tumors have evolved ways to evade this immune surveillance. Most somatic cells display their inner composition via peptide presentation on MHC I on their surface. One immune evasion mechanism selects for tumor cells that have downregulated their MHC I expression, thus hiding their compromising antigens. Additional strategies include the passive or active inhibition of immune effector cells by tumor-associated conditions. The tumor milieu often lacks essential amino acids like tryptophan or arginine or displays high levels of immune suppressive cytokines or lactic acid. An also prominent hallmark of tumors is the expression of T cell inhibitory ligands like PD-L1 that can effectively block a robust CTL effector response (Hadrup et al. 2013).

Recent insight into the mechanisms controlling tumor immune surveillance and escape has opened a whole new field for cancer therapy referred to as immuno-oncology. To date, over 25 immunotherapies have been approved against cancer. These include the use of oncolytic viruses, cancer vaccines and cytokines, all of which have been shown to help drive anti-tumor immune activation. Monoclonal antibody-based drugs direct T cells to tumor cells as bispecific antibodies, or block the inhibitory PD-1/PD-L1 or CTLA-4 engagement as so called checkpoint inhibitors (Tang et al. 2018).

A promising new approach is referred to as adoptive T cell therapy (ATT). It makes use of anti-tumor CTLs as a cellular therapeutic agent. The extraction, *ex vivo* expansion and re-application of TILs with inherent tumor-specificity has already been shown to be effective in melanoma patients (Rosenberg et al. 2011). Alternatively, peripheral T cells from the patient (autologous) or taken from a donor (allogeneic) can be genetically engineered to gain an anti-tumor specificity. TAA-specific TCRs have

been identified via antigen-induced expansion of CTLs *ex vivo*. Wilde et al., for example, confronted T cells with DCs expressing a melanoma TAA, together with either an autologous or allogeneic MHC type (Wilde et al. 2009). Out of the heterogeneous T cell population, only cells with TAA-specific TCR proliferate. Against the allogeneic background, they were able to isolate melanoma specific TCRs with an unphysiologically high avidity. Re-transfected into T cells, these showed a high functional activity against melanoma cells.

Although boosting the TCR avidity to unphysiological strength seemed promising, it became clear however, that caution is advised. High TCR avidity can cause deleterious cross-reactivity to healthy tissue. TCRs with enhanced avidity against melanoma associated antigen (MAGE-A)-3 mediated lethal cytotoxicity against healthy cardiomyocytes in two patients (Linette et al. 2013). Moreover, it was proposed that low avidity TCR CTLs may be better serial killers as they detach faster from target cells, but still stay in contact long enough to deliver their toxic cargo (Jenkins et al. 2009). The range of TCR avidities that are potent but safe has to be assessed individually for each antigen.

An alternative T cell based therapy uses a different approach to target tumor-expressed antigens. Instead of employing a transgene TCR, this therapy makes use of “engineered” receptors to redirect the patient’s own T cells. These so called chimeric antigen receptors (CARs) are fusion proteins based on antibodies and CTL stimulatory domains. A CAR’s extracellular domain is derived from the variable region of an antibody that delivers a degree of tumor-specificity, but is MHC I independent. The intracellular CTL activating domain is derived from CD3 ζ , a key protein in the TCR signaling pathway. To increase persistence and activity of CAR-engineered T cells, the intracellular domain of CARs can be further extended by one or more co-stimulatory signaling domains. Without those co-stimulatory domains, the anti-tumor response from CAR T cells has been found to be not prolonged or sufficient for effective killing (Cartellieri et al. 2010). The two currently Food and Drug Administration (FDA) approved CARs contain an intracellular co-stimulatory domain derived from either CD28 or 4-1BB receptors (Sadelain 2017). T cells engineered with these CARs showed high persistence of up to 20 months and a durable response in leukemia patients (Neelapu et al. 2017; Maude et al. 2018). However, although co-stimulation is crucial for the efficacy of therapeutic T cells, the coupling of stimulatory and antigen-detecting domains within one receptor also harbors risks. These CAR T cells have a much lower activation threshold, and thus are more likely to attack healthy cells expressing the antigen at low physiological levels (Morgan et al. 2010).

Similar to the co-stimulation coupled CARs, high avidity TCRs can also cause severe side-effects via cross-reactivity or on-target effects against healthy cells expressing TAAs at physiological levels. Using low avidity TCRs like those naturally occurring in TILs, for example, may be a better choice for

clinical application. Instead of boosting T cell activity and persistence via enhanced receptor avidity, we and others are working on co-stimulation that can be introduced as a separate mechanism into a therapeutic T cell to enhance the efficacy of low-avidity CTLs.

The continuous stimulation of e.g. CD28 by CD80 expressed on target cells was found to promote durable T cell cytotoxicity (Krummel et al. 1999). By contrast, the PD-L1/PD-1 inhibitory axis counteracts CTL activity and is a prominent feature in many tumors that is linked to immune evasion. In a novel approach, chimeric receptors were designed to turn that inhibition into activation (**Figure 1**). Here, extracellular inhibitory domains derived from PD-1 were fused to intracellular stimulatory CD28 or 4-1BB signaling domains. These chimeric receptors enhance potential T cell effector function when confronted with PD-L1 positive tumor cells (Prosser et al. 2012; Ankri et al. 2013). They provide a tool to upgrade TILs or low avidity T cells and fine-tune T cell activity for effective but safe tumor treatment.

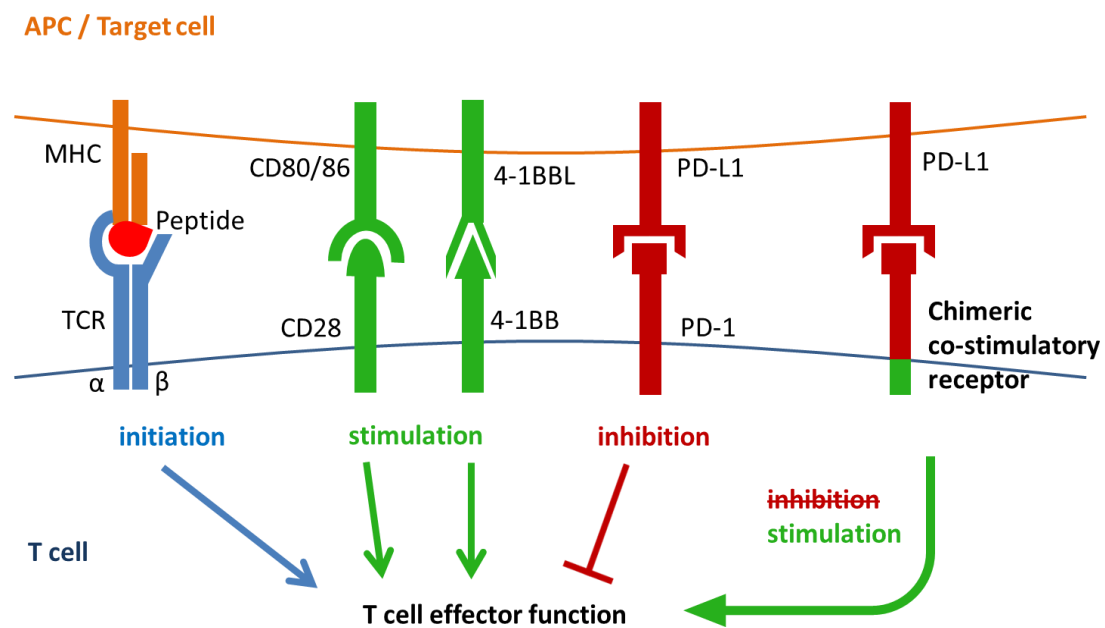


Figure 1 T cell signaling receptors. TCR binding to peptide-bound MHC initiates various T cell effector functions. Co-stimulation via CD28 bound by CD80 or CD86 or via 4-1BB bound by 4-1BB ligand (4-1BBL) is necessary for ongoing T cell effector function. T cell effector function is inhibited via PD-1 bound by PD-L1 which is often expressed on tumor cells. Fusion of extracellular inhibitory domains, e.g. from PD-1, and intracellular stimulatory domains, e.g. from CD28 or 4-1BB, leads to chimeric co-stimulatory receptors that turn inhibition into stimulation.

3.2 Multicellular tumor spheroids

3.2.1 Three dimensional cell culture

Cell-cell and cell-matrix adherence is an important physical property for tissue formation in multicellular organisms. Conventional cell culture grows cells in monolayers that adhere to the culture vessel. This culture technique has been used for decades for the investigation of cell biology.

Culturing cells in a 3D manner, however, is thought to provide a more physiological platform for *in vitro* analyses. A series of techniques have been established to rebuild and culture 3D organ structures. These approaches range from the use of multilayers, over matrix embedded or scaffold based cell cultures, and microfluidic systems, to whole “organs on a chip” (Friedrich et al. 2007; Huh et al. 2011). One classic and broadly applied method uses the culture of cells in 3D multicellular spheroids. These spheroids are comparatively easy to grow, maintain and handle, and add a significantly exploratory value when compared to monolayer cultures.

3.2.2 Spheroid culture techniques

Early studies performed in the 1950's had already demonstrated the potential of embryonic suspension cells to reaggregate into compact clusters *in vitro*, and that these clusters “re-establish tissue-like relationships” (Moscona 1957). When deprived of a surface to grow on, adherent cells tend to attach to each other instead. They then form cellular aggregates and ultimately dense and spherical shaped spheroids.

Spheroid formation can be induced via various culture techniques. For example by culture in roller tubes, spinner flasks or on gyratory shakers, settling of cells to the bottom of the culture set up is inhibited by the constant movement. These approaches allow the generation of spheroids at a large scale, but also require large amounts of media.

Alternatively, the culture of spheroids in 96-well plates, or in hanging drops allows the use of smaller quantities of growth media and, in addition, the individual manipulation and analysis of single spheroids. Dishes or plates can be pre-treated to inhibit the adhesion of cells to the culture plastic. Coating with agarose, or with the hydrogel polyhydroxyethylmethacrylate (polyHEMA), has been used effectively. Spheroid cultures in single drops hanging from the lid of a culture dish simply exploit gravity to prevent cell attachment to plastic. Portioning cell suspensions in single wells or hanging drops generally results in the formation of single spheroids of a homogeneous size and shape (**Figure 2**). This thus allows consistent results from analyses based on individual spheroids (Friedrich et al. 2007).

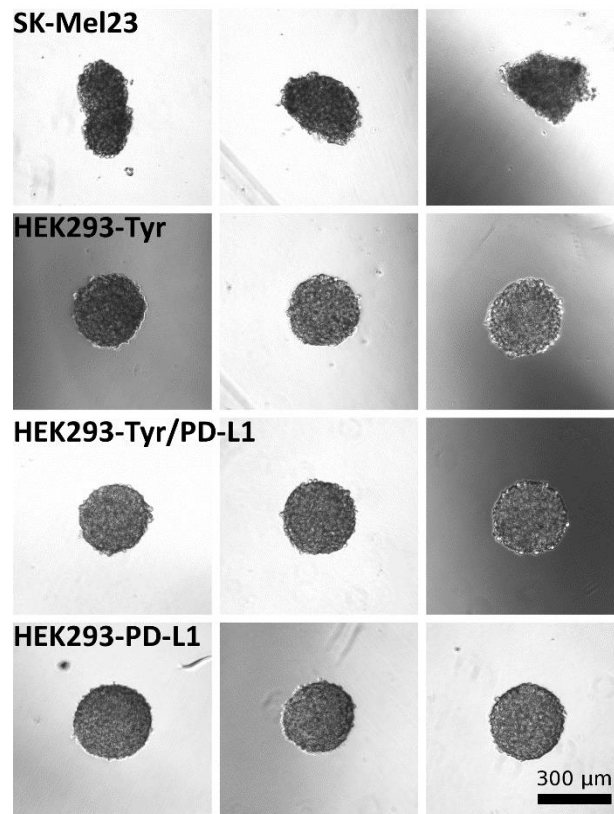


Figure 2 Tumor spheroids. Homogeneous spheroids generated from different tumor cell lines, grown in hanging drops for 3 d.

3.2.3 Spheroids as *in vitro* tumor models

The application of spheroid techniques has proven to be a valuable model system in cancer research. Sutherland and colleagues were the first to use multicellular tumor cell spheroids to test therapeutic efficacy. The authors showed that tumor cells grown as spheroids were less sensitive to radiotherapy than were monolayer cells (Sutherland et al. 1970). Bissell et al. further fueled skepticism about the reliability of results generated with 2D culture systems by showing that the environment and shape of a cell direct its gene expression profile (Bissell et al. 1982). Culturing cells in multicellular aggregates allows 3D cell-cell interactions, and hence a more physiological shape than that seen on plastic. Indeed, both proteomic and genetic expression profiles of tumor cells differ with their culture dimensionality (Gaedtke et al. 2007; Witt Hamer et al. 2008).

Another parameter that tumor spheroids are able to mimic quite precisely is the heterogeneous tumor microenvironment. Solid tumors are normally undervascularized, harboring microregions with decreased perfusion. This leads to oxygen and nutrient concentration gradients, and metabolic waste gradients. Hypoxic and acidic regions at a greater distance to blood vessels often become necrotic, whereas cells in proximity to the vasculature are highly proliferative. In between these regions the cells are generally quiescent. Tumor spheroids can reflect these intervascular microregions with

respect to heterogeneous environments and cellular phenotypes. As spheroids grow larger, the inner most cells become deprived of oxygen and nutrients and toxic metabolic waste accumulates. The undersupplied center can become necrotic. It is then surrounded by a layer of quiescent cells with an outer rim of proliferating cells (**Figure 3**, Sutherland 1988; Hirschhaeuser et al. 2010).

In addition, the general cellular growth kinetics of spheroids has been shown to reflect those seen within their *in vivo* counterparts, with an early exponential growth, followed by a period of retarded growth (Mayer et al. 2001).

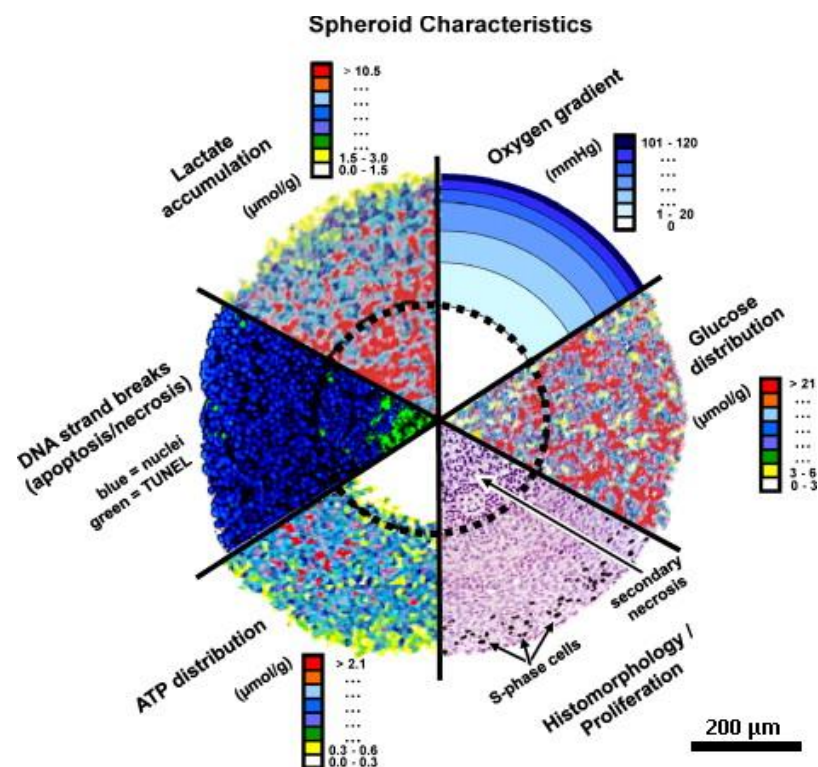


Figure 3 Composition of a spheroid's heterogeneous physiology displayed as combined images of median sections analyzed with different methods: autoradiography, the tunnel assay, bioluminescence imaging, and probing with oxygen microelectrodes (adapted from Hirschhaeuser et al. 2010).

As proposed early on by Sutherland et al., these heterogeneous tumor conditions impact tumor cell drug resistance and therefore make tumor spheroids an excellent *in vitro* model to predict potential therapeutic efficacy *in vivo* (Sutherland et al. 1970).

In addition to a decreased response to radiotherapy, tumor cells in spheroids also display increased resistance to chemotherapy. Diffusion gradients may limit the effect of therapeutic agents in cells deeper within the spheroid. Moreover, quiescent subpopulations are less susceptible to the chemotherapies that target proliferative cells (Shield et al. 2009). Spheroids also better reflect the suppressive effects seen on therapeutic immune cells in their *in vivo* solid tumor counterparts. In melanoma spheroids antigen-specific cytotoxic T lymphocytes display weaker effector activities than

that seen in 2D (Feder-Mengus et al. 2007). The authors suggest that steric hindrance within the 3D context and increased lactic acid levels, among other phenomena, are responsible for the decreased CTL effector function seen.

The literature describes many examples of decreased therapy susceptibility when switching from 2D to 3D cultures. In these settings, the spheroid systems were better at predicting the clinical outcome (Hirschhaeuser et al. 2010). Therefore, tumor spheroids are currently under development as a more efficient drug screening platform, and a bridge between classic *in vitro*, and expensive and ethically critical *in vivo* experiments. They can also act as a potential tool for the early negative selection of drugs that initially seemed promising in 2D assays.

Examples show that tumor spheroids can also be used for positive drug selection. Trastuzumab is a therapeutic monoclonal antibody that binds human epidermal growth factor receptor (HER) 2, thus blocking proliferative signaling. Tumor spheroids have shown an enhanced HER2 homodimer formation, leading to an increased activation of HER2 downstream signaling pathways. Consequently, trastuzumab evoked a stronger response in tumor cells in spheroids than that seen in 2D cultures (Pickl and Ries 2009). This demonstrates that tumor spheroid cultures have the potential to discover therapies that target alternative mechanisms that are less obvious in monolayer cell cultures.

In addition, it appears that primary tumor cells maintain their *in vivo* phenotype when cultured in spheroids. Heterogeneous spheroid cultures from tumor biopsies have been shown to maintain their tumorigenic potential and their genomic stability (Witt Hamer et al. 2008). This theoretically enables the use of primary tumor spheroids for the evaluation of different therapeutic approaches as a pre-test *in vitro*, for a personalized medicine approach (Witt Hamer et al. 2009; Halfter et al. 2016, Vlachogiannis et al. 2018).

To gain information from spheroid assays a spectrum of methods and analytical endpoints has been applied. The next section provides an overview over possible strategies.

3.2.4 Analysis of three dimensional spheroids

A 3D specimen such as seen with a tumor cell spheroid imposes special requirements on potential analysis methods.

The dissociation of spheroids into cell suspensions does allow analysis at a cellular level, using the methods that are also available for classically cultured cells. Assessment of protein, RNA or DNA composition of spheroid cells is possible and broadly applied. Thus, for instance, the genomic stability

of primary cells, or surface expression of tumor-associated antigens can be monitored (Witt Hamer et al. 2008; Feder-Mengus et al. 2007).

In addition to the characterization of a spheroid's genetic or proteomic profile, cell viability represents a crucial read-out for drug testing. After dissociation, colony formation assays have been used to assess cell viability since the first application of spheroids as tumor models (Sutherland et al. 1970). Direct cell counting or flow cytometry based approaches after live/dead staining are also feasible.

The spheroid volume, or rather its diameter, represents a faster and more direct method of assessing tumor cell viability. In high-throughput screenings, spheroids are monitored over time via widefield imaging. Treated and untreated spheroids in whole 96-well plates can be rapidly analyzed with regards to growth, stagnation, shrinkage or dissociation.

Since the spheroid volume does not always correlate with cell viability, the respiratory or proliferative activity, as well as the cellular membrane integrity, can be measured. In this instance, assays based on absorption, luminescence or fluorescence of the supernatant or the spheroid itself can be employed.

Furthermore, the potential effect of a treatment on the invasiveness of tumor cells can be assessed by determining the spheroid's potential to grow out onto, or into, a surrounding matrix (Hirschberg et al. 2006; Hirschhaeuser et al. 2010).

For an in-depth analysis of spheroids that does not destroy their spatial integrity, other methods need to be employed. Assessment of the penetration or action of a therapeutic agent in context of the tumor spheroid depth and micromilieu, for example, requires observation *in situ*. Also, the analysis of cell-cell interaction, spatial distribution of cells in mixed spheroids, or spheroid invasion by therapeutic cells depends on *in situ* measurements.

Sectioning paraffin embedded or cryopreserved spheroids does allow these types of analyses, for example through (immuno)histologic approaches (**Figure 3**). Even a reconstruction of the 3D composition via computational re-arrangement of serial histological sections can be achieved (Wang et al. 2015). As the authors state, however, re-alignment of histological sections is impeded by dissimilar quality due to tissue disruption and staining artefacts.

3D object reconstruction hugely benefits from advanced 3D imaging methods. They allow optical sectioning and reconstruction of 3D specimen without elaborate – and possibly distorting – sample processing. 3D microscopy techniques need to be able to penetrate the depth of complex and highly scattering samples. They accomplish this via different optical approaches (**Figure 4**).

The historically most widely used 3D fluorescence microscopy techniques are confocal laser scanning microscopy (CLSM) and two-photon microscopy (2PM). In confocal microscopy, a pinhole blocks out-of-focus signal, thus limiting the detected emission signal to the focal point. In contrast, two-photon

microscopy confines the excitation to the focal point. This is achieved via spatially and temporally focusing low energy photons. Only directly at the focal point is the energy high enough to excite fluorophores. Longer laser wavelengths providing low energy photons allow, in addition, deep penetration into light scattering samples.

Both CLSM and 2PM are point-scanning microscopes imaging a sample voxel by voxel. While they provide good optical sectioning, they suffer from long acquisition times that effectively limit their speed in timelapse imaging. Moreover, especially CLSM exposes the whole sample to high excitation light intensity with each detected point. This causes photobleaching and phototoxicity, which is especially deleterious with repetitive acquisition over time.

One attempt to increase acquisition speed and reduce photodamage was addressed with spinning disc confocal microscopy (SDCM). On a rapidly spinning disc an array of excitation and emission pinholes are arranged. It scans the field of view over 1000 times per second. While SDCM images faster and with lower peak excitation light density than does CLSM, it still illuminates the whole z-axis and suffers from low penetration depth (Fischer et al. 2011).

When regarding the efficiency of sample illumination and fluorophore excitation, the most elegant method at present is selective plane illumination microscopy (SPIM), also known as light sheet fluorescence microscopy (LSFM). This method is based on the illumination of the sample from the side, with a thin sheet of light perpendicular to the detection axis. Thus, excitation is confined to the focal plane. At each z-position a charge-coupled device (CCD) camera takes a widefield image from the whole plane at once. This reduces inefficient exposure of fluorophores to laser light to basically zero. It also reduces acquisition time, only requiring scanning in z-direction instead of point-to-point. Extraordinarily low bleaching and phototoxicity as well as rapid acquisition makes SPIM the perfect tool for live imaging of multicellular organisms.

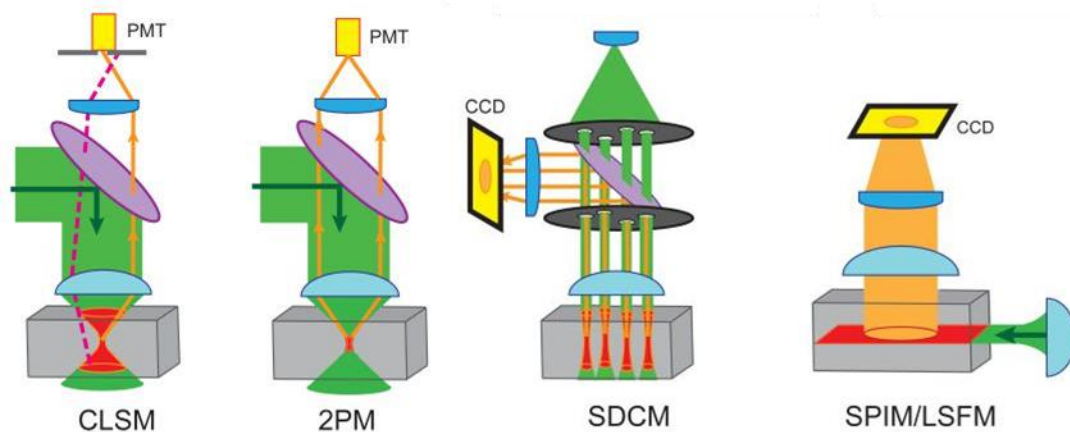


Figure 4 Optical principle of different fluorescent microscopes. Confocal laser scanning microscopy (CLSM), two-photon microscopy (2PM), spinning disc confocal microscopy (SDCM) and selective plane illumination microscopy (SPIM) or light sheet fluorescence microscopy (LSFM), compared are illumination (green) and detection (orange) paths as well as excited sample areas (red). PMT = photomultiplier tubes, CCD = charge-coupled device (adapted from Fischer et al. 2011).

Many SPIM devices implement the additional option to rotate the sample, and image it from several angles. In this setting, the illumination and the detection axes run horizontally, and the sample is mounted in a way such that it hangs parallel to gravity. Recording the image stacks from multiple directions, and subsequent fusion into one dataset improves image quality by several means. Limited penetration depth into the sample can be overcome by adding detectable cell layers from every side of the sample to the overall information. Dark regions that are in the lightpath behind an optically denser region, and therefore in shadow, can be better illuminated from another direction. And, most importantly, the inferior resolution in z can be compensated, resulting in an overall isotropic resolution. Despite the increase in acquisition time, and the need for computational post-processing, this method is widely used. Its power to generate homogeneous images over a similar depth from every side of an object makes SPIM an excellent microscope for round spheroids (Pampaloni et al. 2013). By including a so-called deconvolution algorithm to the data processing workflow, the resolution of SPIM data can be greatly increased over that of confocal microscopy (Verveer et al. 2007). Open source projects like “openSPIM” make light sheet microscopy accessible for a broad scientific community (Pitrone et al. 2013). With a set of detailed instructions provided by this source, a homemade SPIM device is achievable at a comparably low cost, and was used within the scope of this thesis.

3.3 Objectives of this thesis

Cell based cancer therapies represent new approaches for the treatment of malignancies. The goal of this thesis was to implement a new *in vitro* tool to quantify the invasion potential of therapeutic cells into experimental tumors, and to potentially assess relevant parameters linked to the biology in question. Tumor spheroids recapitulate *in vivo* intervascular microregions and thus were to be used as invasion matrix for therapeutic cells. The 3D microscopy technique SPIM was evaluated as a method to efficiently image whole infiltrated spheroids, and to localize single cells within 3D specimens.

- Because of their innate tropism for tumor environments, and their ability to be extensively expanded, MSCs are under investigation as potential therapy vehicles for the delivery of agents deep into solid tumors. It has been shown that some pre-conditioning procedures can enhance the tumor homing and infiltration potential of MSCs. The spheroid invasion assay was designed to test the influence of various, clinically relevant parameters, on the ability of primary human MSCs to migrate into experimental tumors.
- Cytotoxic T lymphocytes can selectively kill tumor cells. Increasing the avidity of a CTL T cell receptor can enhance its potential response to tumor cells. The spheroid invasion assay was adapted to measure important aspects of CTL behavior in a more physiologic tumor setting than that achieved with classic CTL assays. One question here was how the TCR avidity influences the killing capacity and the invasion of CTLs into experimental tumors.
- Strong TCR avidity also harbors the risk of unwanted side effects. Activating co-stimulatory pathways instead of enhancing TCRs represents an alternative and potentially safer approach to achieve anti-tumor response. Chimeric co-stimulatory receptors PD-1:28 and PD-1:BB were developed in our laboratory. They were designed to turn CTL inhibition mediated by PD-L1 (often overexpressed on tumor cells) into CD28 or 4-1BB related stimulation (Schlenker 2015). The tumor spheroid system with its specific milieu was to be employed in a 3D cytotoxicity assay to assess the potential effects of the chimeric co-stimulatory receptors.

4 Material

4.1 Antibodies

Immunogen	Fluorochrome	Species/ Isotype	Clone	Manufacturer	Application, Dilution
Primary Antibody					
HA	-	Rat IgG		Dr. med. E. Kremmer, Helmholtz-Zentrum, Munich, Germany	Immune fluorescence, 1:10
PD-L1 (CD274)	FITC	Mouse IgG1	MIH1	BD, Heidelberg, Germany	Flow cytometry, 1:8
PD-L2 (CD273)	APC	Mouse IgG1	MIH18	BD, Heidelberg, Germany	Flow cytometry, 1:8
HLA-A2	-	Mouse IgG1	HB54	In-house production	Flow cytometry, 1:2.75
Secondary Antibody					
Rat IgG	A594	Donkey IgG		Thermo Fisher Scientific, Schwerte, Germany	Immune fluorescence, 1:500

4.2 Cell Culture

4.2.1 Blood and human bone marrow samples

Drawing of blood and human bone marrow samples from healthy donors was performed by trained personnel and approved by the local Ethics Committee. Donors gave their consent.

4.2.2 Primary cells

Cell line	Type/ Modification	Source
hBMSC	Primary human bone marrow derived mesenchymal stem cell batches, cultured in DMEM culture medium or Bio-1	
Batch		
AP99		apceth, Munich, Germany
AP182		apceth, Munich, Germany
AP172		apceth, Munich, Germany
AP158-3		apceth, Munich, Germany
G01-AP182	Transduced with RANTES-HSV-TK construct	apceth, Munich, Germany

	G01-AP141	Transduced with RANTES-HSV-TK construct	apceth, Munich, Germany
	G01-AP194	Transduced with RANTES-HSV-TK construct	apceth, Munich, Germany
	AP182 TD #202	Transduced with (constitutive promoter) EFS-HSV-TK construct	apceth, Munich, Germany
	hBMSC 110331		AKB Gauting, Stiftung Aktion Knochenmarkspende Bayern, Germany
	hBMSC 130806		AKB Gauting, Stiftung Aktion Knochenmarkspende Bayern, Germany
	hBMSC 141007		AKB Gauting, Stiftung Aktion Knochenmarkspende Bayern, Germany
	hBMSC 140826		AKB Gauting, Stiftung Aktion Knochenmarkspende Bayern, Germany
	hBMSC 130801		AKB Gauting, Stiftung Aktion Knochenmarkspende Bayern, Germany
MSC		Primary human mesenchymal stem cell batches cultured in DMEM culture medium	PD Dr. Wolfgang Erl, Institut für Prophylaxe und Epidemiologie der Kreislaufkrankheiten, LMU Munich, Germany
	Batch		
	YI-1	Umbilical cord blood derived	
	MSC 101003M	Umbilical cord subendothelial derived	
	MSC 110501M	Umbilical cord subendothelial derived	
CTL		Primary human cytotoxic T lymphocytes, cultured in RPMI culture medium	From PBMCs, isolated, activated and engineered at Prof. E. Nöbner's lab, Helmholtz Center, Munich, Germany
	D115/Mock	Transduced with D115-pMP71 and empty medium	
	D115/PD-1:28	Transduced with D115-pMP71 and PD-1:28 TM -pMP71	
	D115/PD-1:BB	Transduced with D115-pMP71 and PD-1 TM :BB-pMP71	
	T58/Mock	Transduced with T58-pMP71 and empty medium	

	Mock/Mock	Transduced twice with empty medium	
--	-----------	------------------------------------	--

4.2.3 Cell lines

Tumor cell lines		Human tumor cell lines, DMEM culture medium	
	Batch		
	HT-29	Human colorectal adenocarcinoma cells	ATCC, Manassas, Virginia, USA
	HUH7	Human hepatocellular carcinoma cells	JCRB Cell Bank, Osaka, Japan
	LS174T	Human colorectal adenocarcinoma cells	ATCC, Manassas, Virginia, USA
Tumor cell lines		Human tumor cell lines, cultured in RPMI culture medium	
	HEK GaLV	Retroviral packaging cell line expressing gag, pol and env genes	Kindly provided by Wolfgang Uckert, Max Delbrück Center Berlin, Germany
	HEK293/PD-L1	Human embryonic kidney cells, HLA-A2 ⁺ , transduced to express PD-L1	Kindly provided by Matthias Leisegang, Max Delbrück Center Berlin, Germany
	HEK293/Tyr	Human embryonic kidney cells, HLA-A2 ⁺ , transduced to express tyrosinase	Kindly provided by Matthias Leisegang, Max Delbrück Center Berlin, Germany
	HEK293/Tyr/PD-L1	Human embryonic kidney cells, HLA-A2 ⁺ , transduced to express tyrosinase and PD-L1	Kindly provided by Matthias Leisegang, Max Delbrück Center Berlin, Germany
	SKMel23	Human melanoma cells, HLA-A2 ⁺ /tyrosinase ⁺	Monica C. Panelli, NIH, Bethesda, USA
	A375	Human malignant melanoma cells, HLA-A2 ⁺ /tyrosinase ⁻	Kindly provided by Prof Judy Johnson, LMU Munich, Germany
	K562	Human chronic myelogenous leukemia cells, HLA-A2 ⁻ /tyrosinase ⁻	ATCC, Manassas, Virginia, USA
	RCC26	Human renal cell carcinoma cells	Helmholtz Center, Munich, Germany
	WM266.4	Human melanoma cells from metastatic site, HLA-A2 ⁺ /tyrosinase ⁺	ESTDAB, Cambridge, UK

4.2.4 Media, supplements and others

Bio-1

DMEM low glucose	89 %	Biochrom, Berlin, Germany
Heparin	1 U/ml	Ratiopharm, Ulm, Germany
Platelet concentrate (TK-2)	6 %	LMU, Munich, Germany
FFP-1	5 %	LMU, Munich, Germany

DMEM culture medium

DMEM, low glucose, GlutaMAX™ Supplement, pyruvate	89 %	GIBCO Invitrogen, Darmstadt, Germany
FCS	10 %	Biochrom, Berlin, Germany
Penicillin/Streptomycin	1 %	PAA Laboratories, Marburg, Germany

Serum-free DMEM

DMEM, low glucose, GlutaMAX™ Supplement, pyruvate	100 %	GIBCO Invitrogen, Darmstadt, Germany
---	-------	--------------------------------------

RPMI culture medium

RPMI-1640 medium	87 %	GIBCO Invitrogen, Darmstadt, Germany
L-glutamine	1 %	GIBCO, Thermo Fisher Scientific, Schwerte, Germany
Non-essential amino acids	1 %	GIBCO, Thermo Fisher Scientific, Schwerte, Germany
Sodium pyruvate	1 %	GIBCO, Thermo Fisher Scientific, Schwerte, Germany
FCS	10 %	GIBCO, Thermo Fisher Scientific, Schwerte, Germany

Serum-free RPMI

RPMI-1640 medium	100 %	GIBCO Invitrogen, Darmstadt, Germany
------------------	-------	--------------------------------------

Supplements

Charcoal-stripped FCS (hormone reduced)	Provided by Prof. Christine Spitzweg's laboratory, Klinikum LMU Munich, Germany
DPBS	GIBCO Invitrogen, Darmstadt, Germany
3,3',5-Triiodo-L-thyronine (T3)	Sigma-Aldrich, Taufkirchen, Germany
L-thyroxine (T4)	Sigma-Aldrich, Taufkirchen, Germany
Recombinant human IL-2 (rIL-2)	Cancernova GmbH, Reute, Germany
3,3',5,5'-Tetraiodothyroacetic acid (Tetrac)	Sigma-Aldrich, Taufkirchen, Germany
Trypan Blue	Sigma-Aldrich, Taufkirchen, Germany
Trypsin/EDTA 1 x	GIBCO, Thermo Fisher Scientific, Schwerte, Germany

4.2.5 Plasmids

EFS-HSV-TK	Coding for HSV-TK expression under control of the constitutive EFS promoter	apceth, Munich, Germany
RANTES-HSV-TK	Coding for HSV-TK expression under control of the CCL5/RANTES promoter (Figure 5)	apceth, Munich, Germany
T58 (b23m-p-a7m)-pMP71 D115 (b8m-p-a22m)-pMP71	Sequences of the HLA-A2 restricted, tyrosinase-specific TCRs T58 and D115 cloned into the pMP71 vector backbone (Vector for retroviral transduction combining the murine myeloproliferative sarcoma virus - long terminal repeats (MPSV-LTR) promoter-enhancer sequences and improved 5' untranslated sequences derived from murine embryonic stem cell virus (MESV))	Kindly provided by Matthias Leisegang, Max Delbrück Center Berlin, Germany
PD-1:28 TM -pMP71	Sequences of the chimeric signaling receptors PD-1:28 tm or PD-1 tm :BB cloned into the pMP71 vector backbone	Generated by Ramona Schlenker (Helmholtz Center, Munich, Germany), described in (Schlenker 2015)
PD-1 TM :BB-pMP71		Generated by Stephan Weisz (Helmholtz Center, Munich, Germany), described in (Schlenker 2015)

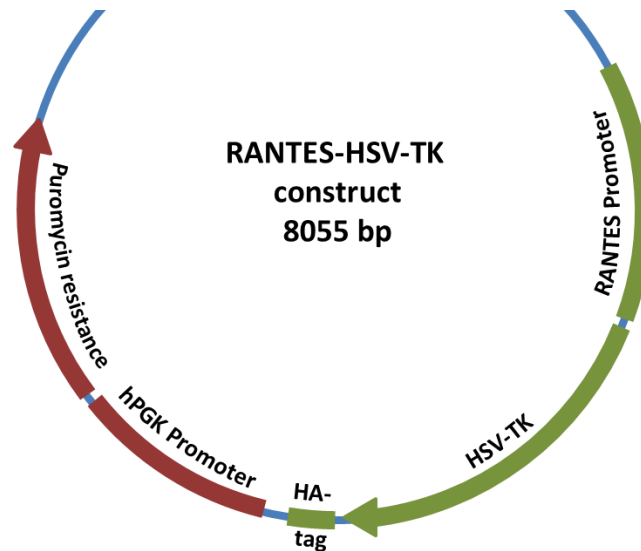


Figure 5 Therapeutic RANTES-HSV-TK construct (according to apceth, Munich, Germany). Plasmid coding for herpes simplex virus type 1 thymidine kinase (HSV-TK) expression under control of the CCL5/RANTES promoter. HSV-TK specifically phosphorylates and therefore activates ganciclovir, a guanosine analogue prodrug.

4.3 Consumables and equipment

4.3.1 Consumables

Name	Manufacturer
μ-Slide 8 well ibiTreat	Ibidi, Planegg, Germany
μ-Slide chemotaxis 3D	Ibidi, Planegg, Germany
Centrifuge tubes 15 ml, 50 ml	Corning, Kaiserslautern, Germany
Cover slips	Menzel-Gläser, Braunschweig, Germany
Cryovials 2 ml	Alpha laboratories, Hampshire, UK
Eppendorf tubes 1.5 ml, 2 ml	Eppendorf, Hamburg, Germany
LumaPlate	PerkinElmer, Rodgau, Germany
Microscope slides	Roth, Karlsruhe, Germany
Microscope slides SuperFrost® Plus	Thermo Fisher Scientific, Schwerte, Germany
Nail polish p2	dm-drogerie markt, Karlsruhe, Germany
Nylon filter cloth 315 μm pore size	Fisher Scientific, Schwerte, Germany
Petri dishes 100 mm	Sigma-Aldrich, Taufkirchen, Germany
Pipette tips 10 μl, 20 μl, 200 μl, 1000 μl	Greiner Bio-One, Frickenhausen, Germany
Serological pipettes 2 ml, 5 ml, 10 ml, 25 ml	Greiner Bio-One, Frickenhausen, Germany
Tissue culture dishes 100 mm	Corning, Kaiserslautern, Germany

Tissue culture flasks 75 cm ²	Greiner Bio-One, Frickenhausen, Germany
Tubes for flow cytometry 1 ml	Greiner Bio-One, Frickenhausen, Germany

4.3.2 General laboratory equipment

Name	Manufacturer
Bio-Plex reader	BIO-RAD, Munich, Germany
Centrifuge Megafuge 2.0 R	Heraeus Instruments, Hanau, Germany
Centrifuge Universal 320/320 R	Hettich, Tuttlingen, Germany
Flow cytometer and cell sorter LSR II BD FACSAria™ Illu	BD, Heidelberg, Germany
Incubator	Binder, Tuttlingen, Germany
Integral water purification system Milli-Q®	Millipore, Schwalbach, Germany
Multichannelpipette	Eppendorf, Hamburg, Germany
Neubauer counting chamber, depth 0.1 mm	Gesellschaft für Laborbedarf Würzburg, Würzburg, Germany
Picture frame glasses for Neubauer counting chambers 20 x 26 mm, depth 0.4 mm	Hirschmann Laborgeräte, Eberstadt, Germany
Pipette set Research® 1000 µl, 200 µl, 20 µl, 10 µl	Eppendorf, Hamburg, Germany
Pipetteboy	Eppendorf, Hamburg, Germany
Scintillator TopCount NXT	PerkinElmer, Rodgau, Germany
Sterile laminar flow hood Herasafe™ KS	Thermo Fisher Scientific, Schwerte, Germany
Thermomixer R	Eppendorf, Hamburg, Germany
Ultrasonic bath Sonorex super	Bandelin, Berlin, Germany
Vortexer MS1 Minishaker	IKA Werke GmbH & Co KG, Staufen, Germany

4.3.3 Microscopes

Microscope	Name	Parts list	Manufacturer
Binocular	SMZ745		Nikon, Düsseldorf, Germany
Fluorescence cell	EVOSfl		Thermo Fisher Scientific,

imaging system			Schwerte, Germany
Fluorescence widefield microscope	Leica DM IL		Leica Microsystems, Wetzlar, Germany
		Jenoptik ProgRes CCD camera	Jenoptik, Jena, Germany
Selective plane illumination microscope	SPIM		Assembled by Dr H. Harz (Center for Advanced Light Microscopy (CALM), Biocenter Martinsried, LMU Munich, Germany) according to (openspim.org); (Pitrone et al. 2013)
		Parts as described on (openspim.org), plus:	
		Obis LS 561-50 561 nm laser	Coherent, Santa Clara, California, USA
Spinning disk confocal microscope	Eclipse Ti-E		Nikon, Düsseldorf, Germany
		CFI P-Apo 40x NA 0.95 objective	Nikon, Düsseldorf, Germany
		Differential interference contrast	Nikon, Düsseldorf, Germany
		CO ₂ , 37°C incubator	Okolab, Pozzuoli, Italy
		IXON 888 Ultra EMCCD camera	Andor, Belfast, Northern Ireland
		SOLA SE II light source	Lumencor, Beaverton, Oregon, USA
		FL-Filterset HC BrightLine eGFP EX: 469/35 , DM: 497 , BA: 525/39 BP	Semrock, Rochester, New York, USA

4.3.4 Computing server

Server	sysGen/SUPERMICRO SuperServer SYS-1028GQ-TRT
Processor	2 x Intel® Xeon® Broadwell-EP Series Processor E5-2680 v4, 2.40 GHz, 14-Core

RAM	256 GB DDR4
Hard disk	3 x 960 GB Samsung SM863 Serie SSD
Graphic card	NVIDIA Geforce GTX Titan X

4.3.5 Software

Name	Application	Source
Chemotaxis and Migration Tool Software	Migration assay analysis	Ibidi, Planegg, Germany
Fiji (Fiji is just ImageJ) 1.48q	Image analysis	Schindelin et al. 2012
Fiji 3D Manager plugin	SPIM data invasion analysis	Ollion et al. 2013
Fiji 3D Object Counter plugin	SPIM data cell segmentation	Bolte and Cordelières 2006
Fiji 3D Watershed plugin	SPIM data cell segmentation	Ollion et al. 2013
Fiji Manual Tracking plug-in	Migration assay cell tracking	Fabrice Cordelières, Orsay, France
Fiji Multiview Reconstruction plugin	SPIM data bead registration, fusion and deconvolution	Preibisch et al. 2010; Preibisch et al. 2014
Fiji μ Manager plugin	Leica DM II and SPIM control software	Edelstein et al. 2010
GIMP 2.8.20	Image editing	Free Software Foundation, Boston, Massachusetts, USA
NIS elements, version 4.51.01	Eclipse Ti-E control software	Nikon, Düsseldorf, Germany
R Studio Version 3.0.2	Statistical analysis	The R Foundation for Statistical Computing, Vienna, Austria

4.4 Reagents, buffers and kits

4.4.1 Reagents

Name	Manufacturer
2-Hydroxyethylagarose, type VII, low gelling temperature	Sigma-Aldrich, Taufkirchen, Germany
^{51}Cr Sodium chromate	Hartmann Analytic, Braunschweig, Germany
7-AAD	Thermo Fisher Scientific, Schwerte, Germany

BSA	Thermo Fisher Scientific, Schwerte, Germany
CellTracker™ Green CMFDA	Thermo Fisher Scientific, Schwerte, Germany
Collagen I Bovine Protein	GIBCO Invitrogen, Darmstadt, Germany
DAPI	Thermo Fisher Scientific, Schwerte, Germany
DMSO	Sigma-Aldrich, Taufkirchen, Germany
EDTA	Sigma-Aldrich, Taufkirchen, Germany
Ethanol ≥ 99.5 %	Roth, Karlsruhe, Germany
Fluo-3, AM	Thermo Fisher Scientific, Schwerte, Germany
Fluorescent microspheres, F-XC 050 Estapor	Merck, Darmstadt, Germany
Fluorescent microspheres, F-Y 030 Estapor	Merck, Darmstadt, Germany
Formaldehyde solution 30 %, methanol-free	Roth, Karlsruhe, Germany
Ganciclovir	Sigma-Aldrich, Taufkirchen, Germany
H ₂ O, Milli-Q® purified	In-house production
HEPES (1M)	GIBCO Invitrogen, Darmstadt, Germany
Isopentane	Chemos GmbH, Regenstauf, Germany
KCl	Roth, Karlsruhe, Germany
KH ₂ PO ₄	Merck, Darmstadt, Germany
KHCO ₃	Sigma-Aldrich, Taufkirchen, Germany
L-Glutamine, 200 mM	Biochrom, Berlin, Germany
Na ₂ CO ₃	Sigma-Aldrich, Taufkirchen, Germany
Na ₂ HPO ₄	Roth, Karlsruhe, Germany
NaCl	Roth, Karlsruhe, Germany
NaHCO ₃	GIBCO Invitrogen, Darmstadt, Germany
NaN ₃	Sigma-Aldrich, Taufkirchen, Germany
NaOH	Merck, Darmstadt, Germany
NH ₄ Cl	Sigma-Aldrich, Taufkirchen, Germany
polyHEMA	Sigma-Aldrich, Taufkirchen, Germany
Propidium iodide	Sigma-Aldrich, Taufkirchen, Germany
Propidium iodide solution	Sigma-Aldrich, Taufkirchen, Germany
Silica gel particles	Fisher Scientific, Schwerte, Germany

SiRHoechst	Spirochrome, Stein am Rhein, Switzerland
Sucrose	Sigma-Aldrich, Taufkirchen, Germany
Tissue-Tek® O.C.T.™ Compound	Sakura Finetek Europe B.V., Alphen aan den Rijn, Netherlands
Titriplex III Na ₂ -EDTA	Sigma-Aldrich, Taufkirchen, Germany
Triton X-100	Appli-Chem, Darmstadt, Germany
Trypan blue	Sigma-Aldrich, Taufkirchen, Germany
Tween 20	Merck, Darmstadt, Germany
Vectashield® mounting medium	Vector Laboratories, Peterborough, UK
Verapamil	Spirochrome, Stein am Rhein, Switzerland

4.4.2 Buffers

Name	Formula
10 x PBS	137 mM NaCl, 2.7 mM KCl, 10 mM Na ₂ HPO ₄ , 1.8 mM KH ₂ PO ₄ in H ₂ O, adjust to pH 7.4 with HCl
4 % PFA	4 % (v/v) formaldehyde in PBS
1 x PBS	10 % (v/v) 10 x PBS in H ₂ O
Blocking solution	2 % BSA (v/v) in 1 x PBS
Permeabilization buffer	0.5 % (v/v) Triton X-100 in PBST
PBST	0.05 % (v/v) Tween® 20 in 1 x PBS
Lysis buffer	8.29 g/l NH ₄ Cl, 1 g/l KHCO ₃ , 37 mg/l Titriplex III Na ₂ -EDTA in H ₂ O
Flow cytometry buffer	2 mM EDTA, 2 % (v/v) FCS, 0.1 % (v/v) NaN ₃ in DPBS
ELISA coating buffer	8.4 g/l NaHCO ₃ , 3.56 g/l Na ₂ CO ₃ in H ₂ O, pH 9.5

4.4.3 Kits

Name	Manufacturer
Cytokine Bio-Plex Human, Th1/Th2 Cytoplex	BIO-RAD, Munich, Germany
ELISA Kit, human IL-2, IFN- γ , TNF- α	BD, Heidelberg, Germany

5 Methods

5.1 Cell culture techniques

5.1.1 Cultivation of cell lines and primary cells

All cells were cultured at 37°C and 5 % CO₂. Cell culture work was conducted in a laminar flow hood to prevent contamination. All reagents were warmed to room temperature prior to use.

For subculturing, adherent cells at 70 – 90 % confluency were washed with DPBS and then detached using 1 × Trypsin-EDTA solution at 37°C for approximately 5 min. The reaction was stopped by adding an at least equal volume of medium containing 10 % FCS. Cells were passaged at ratios suiting their proliferation rate.

Human CTLs from healthy donors were cultivated at 1-1.5 × 10⁶ cells/ml in RPMI culture medium supplemented with 50 U/ml rIL-2 and split every 2-3 days. They were cultivated in 24-well plates.

5.1.2 Freezing and thawing of cells

Cells were frozen in their respective culture medium plus 10 % DMSO in cryo-tubes. They were cooled to -80°C for at least 24 h in an isopropanol container and subsequently transferred to the gas phase of a liquid nitrogen container.

To thaw cells, the frozen cell suspensions were rapidly warmed to 37°C in a water bath. They were immediately transferred into a cell culture vessel filled with medium to dilute DMSO to a non-toxic concentration. Medium was exchanged immediately or within 24 h to remove DMSO completely.

5.1.3 Counting of cells

To determine cell numbers a Neubauer counting chamber was used. Cell suspensions were mixed 1:1 with Trypan blue solution in order to differentiate viable from dead cells. 10 µl of the mixture was applied onto the Neubauer counting chamber and the number of cells/ml was calculated from the average number of cells per square × 10⁴.

5.1.4 Isolation and engineering of primary hBMSCs

MSCs used for this work were isolated and engineered at apceth, Munich, or have been previously established in our laboratory according to the following protocol.

Briefly, human bone marrow stromal cells were extracted from bone marrow of normal donors provided by AKB Gauting, Stiftung Aktion Knochenmarkspende Bayern. For isolation, the

erythrocytes were first removed by mixing the bone marrow 1:1 with lysis buffer. After incubation at room temperature for 10 min, stromal cells were pelleted for 5 min at 500 g and washed with DPBS. They were then resuspended in medium at a volume of 2 ml per ml bone marrow, plated and cultivated at 37°C and 5 % CO₂. After two days medium was changed to remove all non-plastic-adherent cell types.

To verify isolation of MSCs, they were characterized according to the minimal criteria released by the International Society of Cellular Therapy (ISCT, Dominici et al. 2006). In addition to plastic-adherence, the cells were tested for their ability to differentiate into osteoblasts, adipocytes and chondroblasts. Furthermore, their flow cytometry-profile was verified to be CD14, CD19, CD34, CD45 and HLA-DR negative, as well as CD73, CD90 and CD105 positive.

5.1.5 Isolation and engineering of primary human T cells

Primary human T cells were isolated and engineered in Prof. Elfriede Nößner's laboratory (Helmholtz Center, Munich, Germany) as described by Dr. Ramona Schlenker (Schlenker 2015).

Briefly, peripheral blood mononuclear cells (PBMCs) were isolated from fresh human blood samples of healthy donors. From these, activated T cell blasts were expanded. To this end, PBMCs were activated for 2 d in anti-CD3 and anti-CD28 antibody coated wells in rIL-2 containing medium.

Viral transduction was performed using non-replication competent retroviruses in an S2 laboratory. The respective virus particles were harvested from the supernatant of the retrovirus packaging cell line HEK GaLV that expresses *gag* (Group Antigen encoding), *pol* (reverse transcriptase encoding) and *env* (envelope protein encoding) genes and have been transfected with one of the TCR or chimeric protein encoding retroviral vectors. Wells were coated with culture medium of retrovirus packaging cells with virus particles or, for mock transduction, without virus particles. Activated T cells were cultured in virus-coated wells for 4 d with rIL-2, then transferred into fresh wells and cultured with rIL-2 for another 9 d before they were used in experiments or frozen.

To obtain comparable results, for every experiment only groups of T cells isolated from the same donor and with the same transduction and cultivation history were used. T cells from one donor were split into 3 groups and transduced first with either D115-TCR or T58-TCR or mock transduced. For a following second transduction T58-TCR and mock T cells were mock transduced. D115-TCR T cells were split into 3 groups, one was mock transduced and the others were transduced with either PD-1:28 or PD-1:BB chimeric co-stimulatory receptor. All batches were cultured and frozen simultaneously.

5.2 The Invasion Assay protocol

5.2.1 Spheroid generation

The various methods used to generate spheroids are largely based on the general phenomenon that many adherent cell lines tend to attach to each other when deprived of a surface to grow on.

5.2.1.1 Liquid overlay technique

Cell attachment was inhibited by coating the culture flasks and dishes with the hydrogel polyHEMA. They were covered with 2 % polyHEMA in 95 % Ethanol and allowed to dry completely. This step was repeated once to create an even and smooth hydrogel layer. Tumor cells were cultivated in polyHEMA coated flasks at 37°C and 5 % CO₂. After five to seven days, spheroids were grown to an appropriate size of 200 to 300 µm diameter. To exclude larger spheroids they can be filtered through a nylon filter with 315 µm pores.

5.2.1.2 Hanging drop technique

Tumor cell suspensions at specific cellular concentrations (**Table 1**) were seeded in drops of 25 µl culture medium in a petri dish lid (not treated for tissue culture, since the drop's shape is more convex on a hydrophobic surface). The lid was flipped, put on the bottom filled with PBS and cultured in these hanging drops for 3 d. For proper spheroid formation an absolute protection from any vibrations has to be ensured. Spheroids with a diameter of ~ 300 µm were harvested and used for invasion.

Table 1 Spheroids in hanging drops. Numbers of different cell types to generate spheroids with the hanging drop technique.

Cell line	Number of cells per ml	Number of cells per 25 µl drop
Hek293	2.4×10^4 cells/ml	600
HUH7	2.4×10^4 cells/ml	600
SkMel23	3.2×10^4 cells/ml	800

5.2.2 MSC labeling

Prior to invasion, MSCs were labeled with CellTracker™ Green CMFDA using the protocols provided by the company (Thermo Fisher Scientific, Schwerte, Germany). CMFDA belongs to the acetoxymethyl (AM) ester derivatives of fluorescent dyes. The modification of the dye's carboxylic acids with AM ester groups results in an uncharged molecule that can permeate cell membranes. Within the cytoplasm, nonspecific esterases cleave the lipophilic blocking groups, resulting in a

charged form that leaks out of cells far more slowly. DMSO stock solutions must be kept anhydrous, since the solvent will readily take up moisture, leading to spontaneous hydrolysis of the dye. To ensure desiccated conditions, DMSO was stored anhydrous under nitrogen until used to prepare 10 mM CMFDA stocks. To avoid several freezing and thawing cycles, small aliquots were prepared from the stock and stored well sealed, frozen, and desiccated in 50 ml centrifuge tubes with silica gel particles.

MSCs were grown to a confluent layer. After washing once with PBS, they were incubated in serum-free DMEM with 1 μ M CMFDA for 30 min at 37°C and 5 % CO₂. To allow the cells to regenerate and modify the dye to its impermeable and fluorescent form, they were incubated in culture medium containing FCS for an additional 30 min. The cells were then detached and used for the invasion assay. Staining of cells could also be conducted in suspension. Therefore, the same protocol was used with an additional pelleting (centrifugation 300 g for 5 min) and resuspension of cells for each washing or staining step.

5.2.3 MSC application and invasion

1.5 x 10⁴ cells per spheroid were mixed in a volume of 50 μ l each in a 1.5 ml reaction tube and shaken for 30 min at 37°C. MSCs that hadn't attached within this period were washed away with 3 x 100 μ l culture medium under a binocular. Spheroids were seeded back into hanging drops of 25 μ l and incubated for 24 h under normal cell culture conditions. Subsequently, they were fixed for 2 h in 100 μ l 4 % PFA, washed with 3 x 100 μ l PBS and stored at 4°C until imaging.

5.2.4 CTL labeling, application and invasion

CTL staining was conducted as described above for MSCs in suspension, but with 0.5 μ M CMFDA in serum-free RPMI and centrifugation at 1200 g for 10 min.

Application and invasion procedures were essentially the same as described above for MSCs, with one adjustment: It was observed that high avidity TCR T cells were washed away to a higher degree than low avidity TCR T cells, probably due to stronger attachment to dead tumor cells killed within the 30 min of co-incubation. To avoid any ensuing unequal loss of T cells expressing differently avid TCRs, T cells were not washed away, but only thinned down by adding 1 ml medium to the 50 μ l co-incubation volume. Spheroids were then re-seeded into 25 μ l drops from this diluted T cell suspension.

Spheroids were fixed after 1 h, 1 d, 3 d, 4 d and 6 d.

5.2.5 Sample mounting, SPIM imaging and data processing

Post-fixation nuclear staining allowed for later sub-segmentation of single cells and proper spheroid volume measurement. Fixed spheroids were incubated in 1 $\mu\text{g/ml}$ 7-AAD (a DNA intercalator) in PBS overnight at room temperature. They were washed subsequently 3 \times 5 min with PBS.

Selective plane illumination microscopy is based on the principle of laser excitation confined to the focal plane. Specimens are illuminated by a laser light sheet perpendicular to the detection axis thereby depleting the out of focus signal to a minimum. Samples can be rotated to acquire stacks from several angles prior to computation of 3D reconstructions.

The spheroids were embedded in 2 % low-gelling 2-hydroxyethylagarose in PBS mixed with fluorescent microspheres (F-XC 050 or F-Y 030 Estapor) at a 1:4000 dilution and aspirated into a glass capillary (for information about SPIM sample holders, refer to openspim.org). Mounted on an openSPIM set-up, they were imaged with the solidified agarose hanging directly in PBS in front of the detection lens. The SPIM application is available via open access hardware and open source software (Pitrone et al. 2013; openspim.org). SPIM imaging was performed using a 488 nm (2 mW laser power, 80 - 120 ms exposure time) and a 561 nm laser (5 mW laser power, 60 - 120 ms exposure time) from five different angles equally spaced over 360°. Fusion and deconvolution of the five angles to one homogeneous image were performed using the fluorescent microspheres as fiducial beads via the Fiji Multiview Reconstruction plugin (Preibisch et al. 2010; Preibisch et al. 2014). All image processing steps were conducted in a semi-automated fashion via macros developed with Fiji. Codes were written by David Hörl. Workflow and macros are included in the appendix (11.1).

To minimize data volume, images were acquired with a 2 \times 2 binning. The resolution acquired with a 20 \times water immersion objective (NA 0.5) and a lightsheet thickness of 15 μm full width at half maximum is 540 nm \pm 112 in x, 599 nm \pm 128 in y, and 3908 nm \pm 954 in z for raw image stacks, 1159 nm \pm 185 in x, 862 nm \pm 99 in y, and 1933 nm \pm 1089 in z for fused data, and 378 nm \pm 127 in x, 355 nm \pm 67 in y, and 978 nm \pm 58 in z after deconvolution.

5.2.6 Analysis – cytoplasmic or nuclear single cell segmentation

The invasion potential of cell types was quantified by measuring the shortest distance of each invaded MSC to the surface of the spheroid, and of each CTL to the centroid of the spheroid.

The automated detection of MSCs within the SPIM-imaged spheroids was originally conducted via threshold-based segmentation of the cytoplasmic CMFDA signal. This didn't allow for sub-segmentation of clustering MSCs. Therefore, the analysis macro was optimized to a watershed-based segmentation of 7-AAD nuclear signals of every cell and further selection of those lying within the CMFDA signal mask.

For small and non-clustering CTLs direct watershed segmentation of cytoplasmic CMFDA signal turned out feasible.

All image processing and analysis steps were conducted in a semi-automated fashion via macros developed with Fiji. Workflow and exemplary macros are included in the appendix (11.2).

5.2.6.1 Cytoplasmic MSC cluster segmentation

This strategy was used before including 7-AAD nuclear staining in the workflow. The 488 nm channel CMFDA signals were segmented using the Fiji 3D Object Counter plugin (Bolte and Cordelières 2006). The fused 32-bit grayscale images were down sampled by a factor of 4 and converted into 8-bit by linearly scaling the display range from 0 to 9000 pixel values from the original. Hence, a segmentation threshold was typically set to 70 pixel values and the minimum size filter was set to 200 voxels (to exclude fiducial beads and artifacts). The autofluorescent spheroid was segmented in the same manner with a threshold between 14 and 18 pixel values (tested in advance) and a minimum size of 10^5 voxels. Invasion depths were quantified by the measurement of distances from the center of each MSC cluster to the border of the spheroid using the Fiji 3D Manager plugin (Ollion et al. 2013).

5.2.6.2 Nuclear single cell MSC segmentation

Using the 7-AAD signals, all nuclei within the MSC-invaded spheroid were segmented. For the quantification of invasion depths, only nuclei within the CMFDA signal mask were taken into account and their shortest distances to the spheroid surface was measured.

For nuclear segmentation, the fused and deconvolved 32-bit grayscale images from the 561 nm channel were converted into 8-bit by linearly scaling the display range from 0 to 0.6 pixel values from the original. A Difference of Gaussians filter (Rodieck 1965) enhanced image features by subtracting one image version blurred with 3D Gaussian kernels of $\delta = 2$ pixel from a less blurred version with 3D kernels of $\delta = 4$ pixel. Then, downsampling by a factor of 2 in x, y and z was used to accelerate all subsequent steps. The final nuclear segmentation was performed using the Fiji 3D Watershed plugin (Ollion et al. 2013) with a seeds threshold of 3 pixel values, an image threshold of 0 pixel values and a radius of 7.5 pixel. The segmentation mask of the CMFDA signal created via the 3D Object Counter plugin (Bolte and Cordelières 2006) (threshold determined individually for each 488 nm channel dataset, minimum size of 10^4 voxel) was applied to the nuclear segmentation file. The MSC nuclei detected were further filtered by size (> 300 voxel) to exclude tumor cell nuclei that partly overlap with the CMFDA signal. The spheroid object was also segmented with the 3D Object Counter plugin (threshold determined individually for each 488 nm channel dataset, minimum size of 10^4 voxel).

Finally, the MSC invasion depths were quantified by the measurement of distances from the center of each MSC nucleus to the border of the spheroid using the Fiji 3D Manager plugin (Ollion et al. 2013).

5.2.6.3 Cytoplasmic single CTL segmentation and spheroid volume measurements

Fused and deconvolved 32-bit grayscale images from both 488 nm and 561 nm channels were converted into 8-bit by linearly scaling the display range from 0 to 0.01 pixel values and 0 to 2 pixel values, respectively, from the original. Downsampling by a factor of 2 in x, y and z accelerated all subsequent steps.

The spheroid object was segmented with the 3D Object Counter plugin (threshold determined individually for each 561 nm channel dataset, minimum size of 10^4 voxel). To exclude fiducial beads and restrict further CTL segmentation to the spheroid area, the mask of this segmented spheroid was applied to the 488 nm channel.

Within the latter, the cytoplasmic segmentation was performed using the Fiji 3D Watershed plugin with a seeds and image threshold determined individually and a radius of 3 pixels. The CTLs detected were further filtered by size (≥ 100 voxel) to exclude oversegmented watershed objects. Finally, the CTL invasion depths were quantified by the measurement of distances from the center of each CTL to the centroid of the spheroid using the Fiji 3D Manager plugin. The spheroid object volumes were determined using the Fiji 3D Manager plugin as well.

5.3 HSV-TK expression

5.3.1 Immunohistochemistry on monolayer

Cells were seeded on coverslips and treated according to the respective experiment. Then, they were washed once with PBS and fixed with 4 % PFA for 10 min at room temperature. The fixing solution was exchanged stepwise with PBST to not dry out the cells completely. After permeabilizing the cells 10 min with permeabilization buffer, they were incubated in blocking solution for 1 h. Anti-HA primary antibody was diluted 1:10 in blocking solution and added to the cells for 1 h. After three times washing with PBST, cells were incubated with the secondary antibody anti-rat-A592, diluted 1:500 in blocking solution, for 1 h. Cells were washed for another three times with PBST, postfixed with 4 % PFA for 10 min and washed again three times with PBST. DNA was counterstained with 200 ng/ μ l DAPI in PBST for 5 min. Cells were washed one last time with PBST, mounted on microscope slides in vectashield and sealed with nail polish.

5.3.2 Cryosectioning

Immunohistochemistry on whole mount 3D samples such as spheroids is not practicable as slow diffusion rates hinder a feasible workflow. Thus, spheroids were cryosectioned before immunostaining. Spheroids were collected into a plastic mold and embedded in 30 % sucrose solution overnight in a humid chamber. Sucrose solution was removed and the whole mold filled with Tissue Tek O.C.T™ Compound. Samples were frozen in isopentane at -80°C for 2 min. The cryostat's knife temperature was adjusted to -21°C and the outer temperature to -24°C. The whole Tissue Tek block was cut into 18 μ m sections. Spheroid sections were collected on SuperFrost® Plus microscope slides and stored at -20°C.

5.3.3 Immunohistochemistry on cryosections

Frozen sections on slides were thawed at room temperature for about 20 min. They were washed once with PBS and incubated for 30 min in 0.5 % Triton X-100 in PBS. After washing with PBS again, the samples were incubated overnight in anti-HA primary antibody diluted 1:10 in blocking solution. Samples were washed three times for 10 min with 0.05 % Triton X-100 in PBS. Subsequently, samples were incubated for 3 h in 1:500 anti-rat-A594 antibody and 1 μ g/ μ l DAPI in blocking solution. They were washed three times 10 min with PBS, embedded in vectashield under cover slips and sealed with nail polish.

5.4 Other functional assays

5.4.1 Migration Assay

MSC migration was analyzed using the μ -slide Chemotaxis 3D system from ibidi. MSCs were seeded in collagen I matrix (**Table 2**) and subjected to a gradient between serum-free unconditioned medium and serum-free HUH7 conditioned medium (taken from 48 h HUH7 cultures).

Table 2 Migration assay. Mixture of cells in a 1 mg/ml collagen matrix.

Reagent		Volume	
H ₂ O		10.11 μ l	} 15 μ l medium
10 x DMEM	1:10	2.50 μ l	
200 mM L-Glutamin	1:50	0.5 μ l	
7.5 % NaHCO ₃	1:20	1.25 μ l	
1 M NaOH	V _{Collagen} *0.025	0.25 μ l	
HEPES	1:64	0.39 μ l	
Collagen I 5 mg/ml	1:1.56 bzw 2.5		10 μ l collagen I
Cell suspension	1-3x10 ⁶ /ml		25 μ l cells

Chemotaxis was monitored by time-lapse microscopy over a 24 h period on a Leica DM IL widefield microscope. Pictures were taken every 15 min. Twenty-five randomly selected cells per sample were tracked with the Fiji Manual Tracking plug-in and analyzed using the Chemotaxis and Migration Tool Software from ibidi (**Figure 6**). The migratory behavior of cells was quantified by several parameters: i) forward migration index (FMI), a measure of the efficiency of the migration of cells in relation to the conditioned medium gradient, ii) centre-of-mass (CoM) displacement, so called directionality, that is calculated from the averaged point of all cell endpoints, iii) cell velocity in μ m/min, iv) mean Euclidean distance and v) mean accumulated distance of tracked cells in μ m.

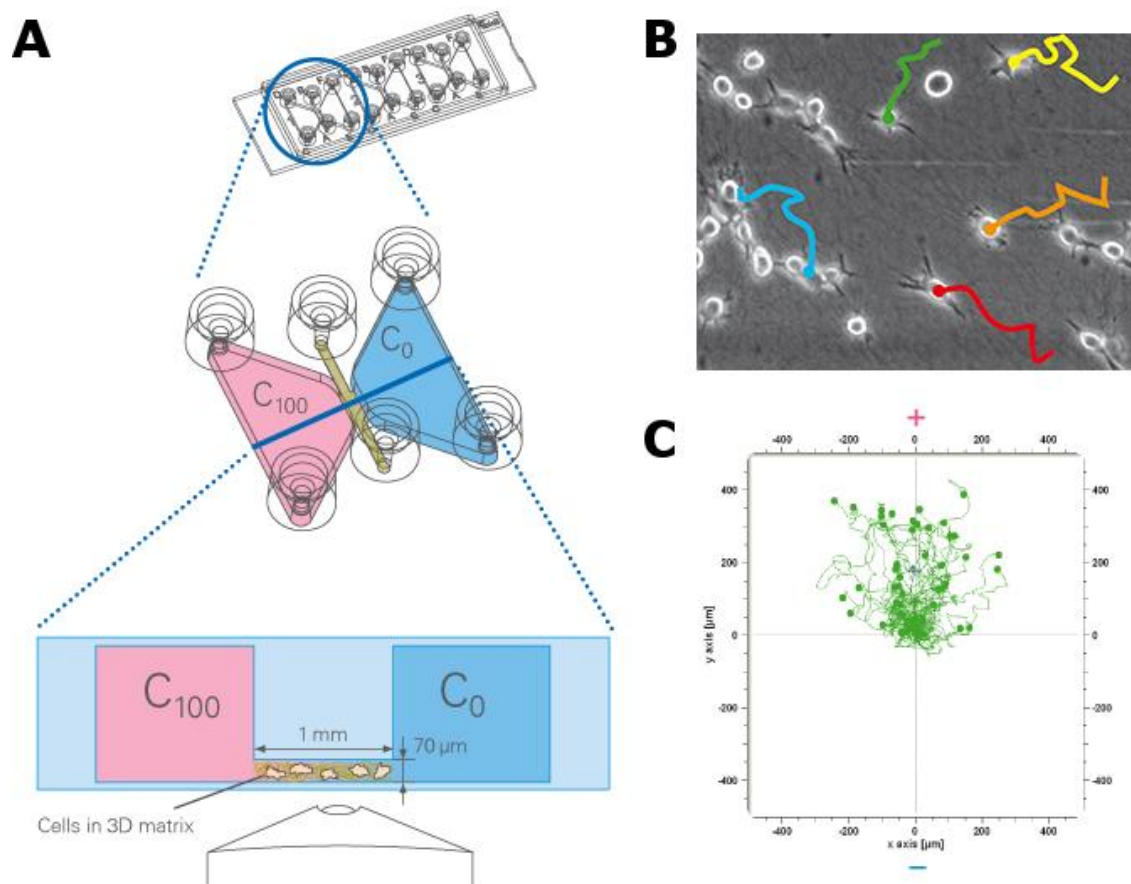


Figure 6 μ -slide Chemotaxis 3D migration assay, ibidi. (A) Cells are seeded into a 3D collagen gel matrix between two chambers filled with chemoattractant or chemoattractant free medium. (B) Time lapse imaging allows tracking of migrating cells. (C) Chemotaxis is analyzed with Chemotaxis and Migration Tool software from ibidi (adapted from ibidi, Munich, Germany).

5.4.2 Live imaging of CTL-target interaction and Ca²⁺ signaling

Fluo-3 AM is a membrane-permeable calcium ion indicator that exhibits an > 100-fold increase in fluorescence intensity upon binding Ca²⁺ (Thermo Fisher Scientific, Schwerte, Germany). Like CMFDA, it belongs to the acetoxymethyl ester derivatives and is handled and stored accordingly (see methods, 5.2.2).

SKMel23 target cells were seeded into μ -slide ibidi 8-well plates at 3×10^4 cells in 300 μ l overnight. Both target cells and CTLs were separately pre-incubated in 2.5 μ M Fluo-3 AM for at least 45 min. μ -slide imaging well plates were mounted onto a Nikon TiE microscope stage at 37°C and 5 % CO₂ under humidified atmosphere. Focus was adjusted, 3×10^4 CTLs in 300 μ l 2.5 μ M Fluo-3 AM containing culture medium exchanged with the medium in the well and imaging started immediately. Both differential interference contrast (DIC) and 488 nm fluorescence widefield images were taken every 30 s for 90 min.

Lethal interactions of single CTLs with single target cells were analyzed manually regarding the chronologic occurrence of contact/immunological synapse formation, Ca²⁺ peaks in and membrane blebbing of target cells.

5.4.3 Standard assays to assess CTL activity

The following assays for quantifying CTL activity were performed by Anna Brandl and Barbara Mosetter at the Helmholtz Center Munich in the laboratory of Prof. Elfriede Nößner.

5.4.3.1 Enzyme-linked-immunosorbent assays (ELISA) for cytokine detection

T cell and target cell mono- and co-culture supernatants were analyzed for IL-2, IFN- γ and TNF- α by “sandwich” ELISA according to the kit’s manufacturer’s protocol.

Briefly, samples were analyzed on 96-well plates coated with antibodies against IL-2, IFN- γ or TNF- α . Once bound, the cytokine was detected using a second antibody via a different epitope. The second antibody was labeled with biotin which in turn was bound by peroxidase-conjugated avidin. Peroxidase converts the substrate 3,3',5,5'-tetramethylbenzidine to a diimine that can be quantified in a spectrophotometer. From this intensity the cytokine concentration was interpolated from a standard curve generated using a standard cytokine dilution series.

Samples for specificity tests were collected from co-cultures of D115/Mock, T58/Mock or Mock/Mock transduced T cells with SKMel23, WM266.4, A375 or K562 cells at an E:T ratio of 1:2. 0.5×10^5 T cells and 1×10^5 target cells were cultured in 200 μ l RPMI culture medium. T cell and tumor cell mono-cultures served as control. Supernatants were harvested after 24 h.

For analysis of chimeric co-stimulatory receptors, the samples were collected from co-cultures of D115/Mock, D115/PD-1:28, D115/PD-1:BB and T58/Mock T cells with SKMel23, HEK293/Tyr or HEK293/Tyr/PD-L1 cells. At an E:T ratio of 1:1 2.5×10^4 cells of each type were cultured in 200 μ l RPMI culture medium. Co-culture supernatants were harvested after 10 h and 24 h and analyzed for IFN- γ levels.

All culture and co-culture supernatants were acquired as triplicates.

5.4.3.2 Bio-Plex analysis for cytokine detection

Cytokine secretion of T cells invading SKMel23 spheroids was assessed via Bio-Plex according to the kit’s manufacturer’s protocol. Cytokines were measured in supernatants harvested from hanging drop invasion cultures described earlier (see 5.2.4). Briefly, SKMel23 spheroids were incubated with T cells

for 30 min and individually seeded into hanging drops. After 24 h supernatants from these drops were collected for Bio-Plex analysis.

Cytokines within the sample were bound by antibodies coupled to beads that were labeled with fluorescent dyes. Via a different epitope, cytokines were detected by biotinylated antibodies that bind to streptavidin-PE conjugates. Cytokines within the samples were quantified on a Bio-Plex-Array-Reader. Various cytokines were detected simultaneously and distinguished via the fluorescent dyes within the beads. The concentration of each cytokine correlated with the signal emitted by PE, and was interpolated from a standard curve generated with a standard cytokine dilution series. The cytokines analyzed here and the corresponding detection limits were IL-2 with 0.001 ng/ml, IL-4 with 0.004 ng/ml, IL-5 with 0.02 ng/ml, IFN- γ with 0.1 ng/ml, TNF- α with 0.1 ng/ml and GM-CSF with 0.04 ng/ml.

5.4.3.3 Chromium release assay

The lytic activity of T cells was assessed by chromium release assay. Target cells were labeled with radioactive ^{51}Cr isotope and incubated with T cells. Target cells lysed by T cells release ^{51}Cr into the supernatant. The amount of lysed cells was calculated from radioactivity levels in the co-culture supernatant.

1×10^6 target cells were re-suspended in 100 μl FCS and labeled with 50 μCi ^{51}Cr for 1 h at 37°C. Target cells were washed twice with culture medium. 50 μl with T cells of serial dilutions were added to each well of a 96-well plate. A constant number of 2×10^3 ^{51}Cr -labeled target cells were added to each well to yield respective effector to target cell ratios. Parallel wells included target cells without T cells to determine the spontaneous chromium release. After 4 h at 37°C, 50 μl of supernatants were pipetted to a filter plate (Luma plate). The maximal amount of radioactivity was assessed from 50 μl of ^{51}Cr -labeled target cells that were pipetted to a filter plate directly after labeling. The filter plates dried overnight. Radioactivity was detected with a scintillator and specific cell lysis was calculated with the following formula:

$$\% \text{ cell lysis} = \frac{\text{measured } ^{51}\text{Cr-release} - \text{spontaneous } ^{51}\text{Cr-release}}{(\text{max. } ^{51}\text{Cr-release}/2) - \text{spontaneous } ^{51}\text{Cr-release}} \times 100$$

5.5 Flow cytometry analysis of SkMel23 cells

All centrifugation steps were performed at 472 g for 5 min at room temperature. All incubation steps were performed in the dark and on ice. $0.05\text{-}0.1 \times 10^6$ cells were transferred into 1 ml FACS tubes,

washed with 500 μ l flow cytometry buffer and the supernatant removed leaving 50 μ l in the tube. Antibodies to surface markers were added and incubated for 30 minutes. When staining included a non-labeled primary antibody, cells were washed again as described above and incubated with the secondary antibody for 30 minutes. After a final washing step as described above, flow cytometry analysis of cells was conducted. Fluorochromes were excited with respective lasers and emission detected with respective filters as shown in **Table 3**.

Table 3 Flow cytometry. Characteristics of used fluorochromes, lasers and filters for detection at the LSRII.

Fluorochrome	Excitation maximum (nm)	Emission maximum (nm)	Laser wavelength (nm)	Detection filter (center/width in nm)
APC	650	660	633	660/20
FITC	494	520	488	530/30
PE	496	578	488	575/26

5.6 Statistical analysis

Statistical tests were performed using R Studio software. The Mann-Whitney U test (or Wilcoxon rank sum test) is a non-parametric test for the comparison of unpaired groups. The Wilcoxon signed rank test is a non-parametric test for the comparison of paired groups. The Kolmogorov Smirnov test is a non-parametric test to compare the distribution of two groups. The Chi-squared test is a non-parametric test to analyze frequency distributions of nominal data. The Student's t test is a parametric test, used within the scope of this thesis to compare independent groups after using a Fisher's F-test to verify the homogeneity of variances. p-values < 0.05 were regarded as significant (*p<0.05; **p<0.01; ***p<0.001).

6 Results

6.1 Invasion assay – establishing a method for the quantification of the tumor invasion potential of therapeutic cells

Based on their excellent homing potential to solid tumors and the fact that they can be relatively easily engineered to express various therapy genes, MSCs are under development as therapy vehicles for the treatment of cancer. Their efficacy relies on their ability to migrate to and infiltrate solid tumors and metastases. A tumor spheroid invasion assay was established to act as a new *in vitro* tool for the characterization of culture parameters linked to the infiltrative ability of MSCs into experimental tumor models.

To this end, a standardized protocol was developed to compare the invasive capacity of MSCs under defined conditions.

Because both numbers of therapeutic cells that had attached to a tumor spheroid, as well as their distance traveled in the spheroid in a specific period of time were relevant parameters, the following workflow was established (**Figure 7**). Spheroids were generated from human hepatocellular carcinoma (HUH7) cells using the liquid overlay technique, or in hanging drops, and selected at a size of approximately 300 μm . One spheroid and 1.5×10^4 labelled MSCs were co-incubated in a volume of 50 μl culture medium in an Eppendorf tube, and placed for 30 min on a shaker. This ensured that each spheroid came in contact with a similar number of cells. A minimum of 1.5×10^4 cells were found to be necessary for the spheroid to be coated after 30 min with a sufficient number of cells to allow subsequent measurement. Cells that had not undergone attachment to the spheroid were washed away. The careful application of this protocol ensured a well synchronized initial starting point for all cells to evaluate their invasive ability. Invasion was stopped by fixation of the spheroids after 24 h (**Figure 7 A**). Selective plane illumination microscopy was then used for 3D imaging to determine the localization of therapeutic cells within the tumor spheroids. MSCs were segmented and their invaded distances were measured as representative value for their invasive potential (**Figure 7 B**).

To accelerate performance of the assay system, the processing and analysis of multiple SPIM datasets was implemented as a semi-high-throughput, semi-automatic workflow based on macros written in Fiji (see appendix, 11.1 and 11.2). This method ensured that each step, from the processing of raw SPIM data, to fused and deconvolved datasets up to segmentation of spheroid and cell objects, had to be manually initiated only once for a whole file containing multiple datasets.

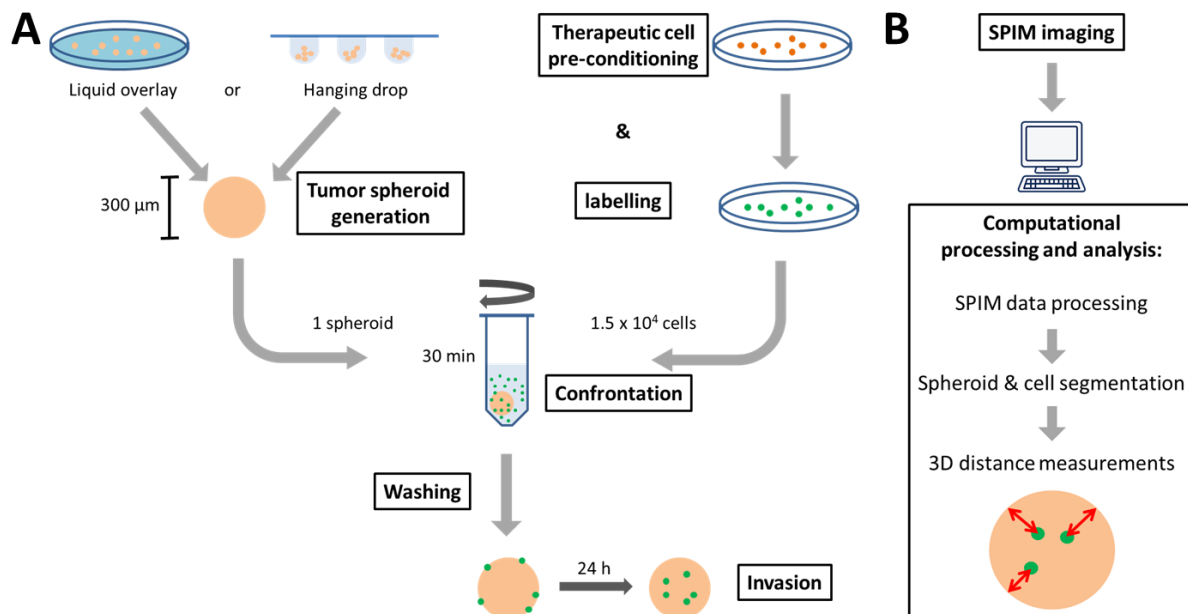


Figure 7 Invasion assay. (A) Wet laboratory protocol and (B) imaging, data processing and analysis workflow.

An initial version of the invasion assay was based on the generation of spheroids using the liquid overlay technique with polyHEMA coated culture vessels, and a semi-automated detection and analysis of MSCs via the segmentation of their cytoplasmic CMFDA CellTracker signal was developed (published in Rühland et al. 2015). This protocol was then modified and optimized with respect to i) the generation of more homogeneous spheroids via the hanging drop method, and ii) an automated analysis which uses additional single cell nuclear staining, and a 3D watershed algorithm to subsegment MSC-clusters. Within clusters of MSCs, single cells could not be detected via CMFDA staining because of a continuous cytoplasmic signal of adjacent cells. To overcome this issue, but still make use of the easy-to-handle and low-toxic CMFDA CellTracker dye, 7-AAD nuclear staining of the whole fixed spheroid was implemented in addition to CMFDA labeling of the MSCs. Since nuclei of adjacent cells do not touch each other, the nuclear signal allowed segmentation of every single cell within the spheroid. This was achieved using Difference of Gaussians, and a 3D watershed algorithm implemented in Fiji (see methods, 5.2.6, and appendix, 11.1 and 11.2). MSC nuclei were then identified as those lying within the CMFDA positive areas (**Figure 8**).

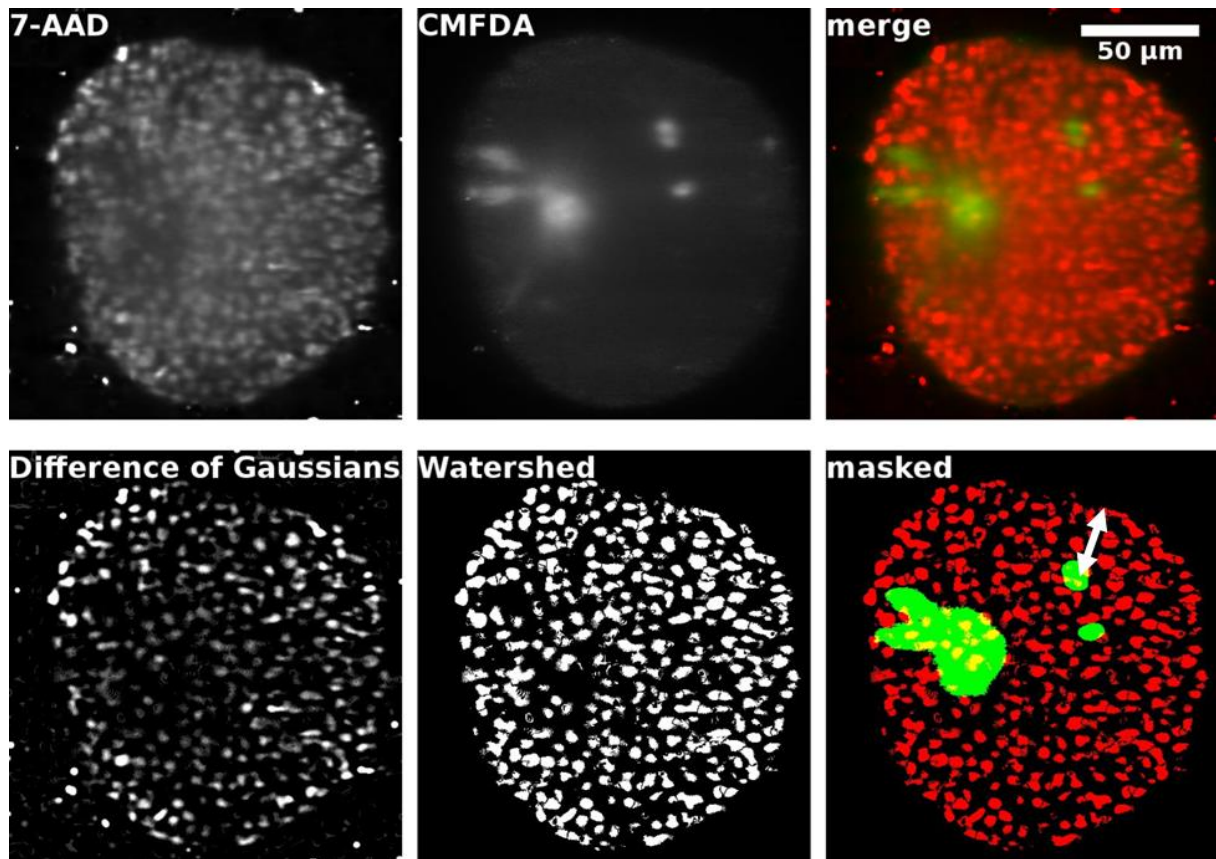


Figure 8 Invasion analysis. Nuclear single cell segmentation of a 7-AAD stained HUH7 spheroid invaded by CMFDA labeled MSCs, imaged with SPIM. A section at a depth of 65 μm of a 3D 2-channel dataset, acquired with a 488 nm and a 561 nm laser is shown. Segmentation was performed via Difference of Gaussians method and a 3D watershed algorithm. For the analysis of the invasion potential of MSCs, the shortest distance of each detected cell lying within the CMFDA mask to the spheroid surface is measured (white arrow).

Within the 3D datasets, the shortest distance from the centroid of each segmented cell to the spheroid surface was measured to extrapolate their invasive potential. **Figure 9** shows that single cell segmentation significantly shifts measured distances to higher values. This is due to the fact that single cell based analysis now takes into account every cell in the larger MSC clusters. These clusters are mostly found in greater depths within the spheroids than are single cells. Thus, invaded distances were previously underrated when all cells within a cluster were only counted as one cell.

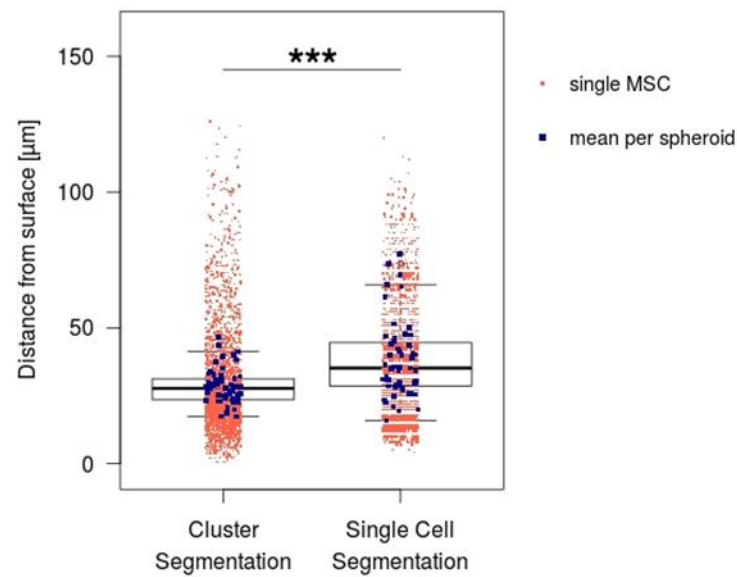


Figure 9 Invasion potential into HUH7 spheroids of primary human bone marrow-derived MSCs analyzed via cytoplasmic cluster, or nuclear staining based single cell segmentation. Cells were CMFDA stained before cryopreservation and thawed directly prior to invasion. MSCs were in passage three at the time of invasion. For a 24 h period, they were allowed to invade HUH7 tumor spheroids grown in hanging drops for 3 d to a size of approximately 300 µm in diameter. After invasion, spheroids were fixed, stained with 7-AAD and imaged via SPIM. Red scatterplots show measurements of the shortest distance from the centroid of each MSC or MSC cluster to the spheroid surface analyzed based on both cytoplasmic cluster and nuclear single cell segmentation. Blue scatterplots depict mean distances per spheroid and whisker-boxplots their distribution, with boxes showing the quartiles and median values and whiskers the rest of the distribution without outliers; Mann-Whitney U test comparing mean values per spheroid, ***p-value < 0,001.

6.2 MSCs' invasion potential into tumor spheroids is dependent on culture conditions

The clinical application of MSC-based therapeutics requires the establishment of robust cell isolation and *ex vivo* culture protocols. Because MSCs comprise only 0.001 – 0.01 % of all nucleated cells in the bone marrow, and enter replicative senescence after about 30 population doublings, an efficient protocol for their expansion to obtain a maximum yield of therapeutic MSCs represents an important issue (Fekete et al. 2012). Controlled conditions and the monitoring of cells are crucial to guarantee a stable medicinal cell product. In addition, the *in vitro* culture needed to generate these cells allows a window for the selective pre-conditioning of MSCs to enhance or modulate their potential to home to and migrate into tumor sites (Shi et al. 2007).

In cooperation with apceth (Munich, Germany), a company producing therapeutic human MSCs under good manufacturing practice conditions, the spheroid invasion assay was employed to screen the effects of various parameters important for the clinical handling and production of cells, specifically as they may influence the invasive behavior of the MSCs.

6.2.1 Activation of primary MSCs with expanded culturing under standard cell culture conditions

It is controversially discussed if increased passaging of MSCs has an enhancing or attenuating impact on tumor recruitment *in vivo*. Whereas downregulation of some chemokine receptors and loss of homing property has been described in higher passaged MSCs, the paracrine signaling of chemotactic cytokines in MSC cultures could also increase MSC migration *in vitro* (Honczarenko et al. 2006; Kyriakou et al. 2008; Boomsma and Geenen 2012).

Using the invasion assay detailed above and HUH7 spheroids, the tumor infiltrating capacity of primary human bone marrow-derived MSCs from increasing culture passages was evaluated.

The MSCs for this assay were isolated and cultured at apceth under GMP conditions using a proprietary apceth culture medium without FCS (Bio-1). From passage three on, the cells were subsequently cultured in our laboratory under standard cell culture conditions using DMEM culture medium. Cells were taken after three, five and seven culture passages, and the spheroid invasion assay was performed based on the initial version of the implemented protocol with polyHEMA derived spheroids and cytoplasmic segmentation based image data analysis (see methods, 5.2.1.1 and 5.2.6.1).

A comparison of samples with increasing culture passages revealed a constant trend towards an enhanced invasion potential. Between passages three and five this increment was significant (**Figure 10**).

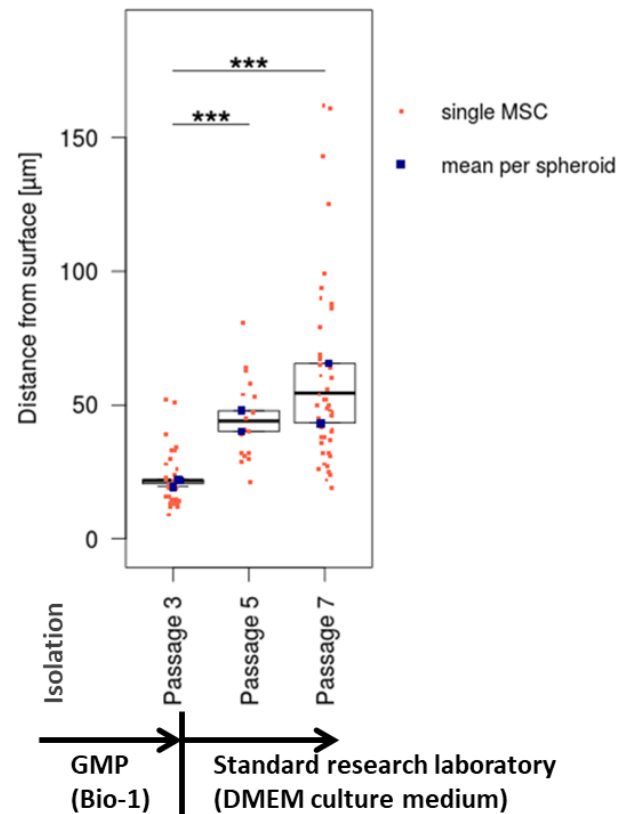


Figure 10 Invasion potential of primary MSCs after different *in vitro* passages. Human bone marrow-derived MSCs obtained at passage three from good manufacturing practice (GMP) production and cultured in Bio-1 medium (DMEM low glucose, 1 U/ml Heparin, 6% platelet concentrate, 5% human fresh frozen plasma) were harvested directly or at passage five or seven, while from passage three on continuously cultured using standard cell culture conditions in DMEM culture medium (DMEM low glucose with GlutaMAX™ Supplement and pyruvate, 10 % FCS, 1 % Penicillin/Streptomycin). The cells were CMFDA labeled and invasion was conducted for 24 h into HUH7 tumor spheroids grown on polyHEMA to a size of approximately 300 µm in diameter. After invasion, spheroids were fixed and imaged via SPIM. Red scatterplots show measurements of the shortest distance from the centroid of each MSC or MSC cluster to the spheroid surface based on automated analysis of invasion depths via cytoplasmic segmentation. Blue scatterplots depict mean distances per spheroid and whisker-boxplots their distribution, with boxes showing the quartiles and median values and whiskers the rest of the distribution without outliers; Mann-Whitney U test comparing mean values per spheroid, *** p-value < 0.001.

6.2.2 Variability of invasive behavior between different donors and sources of MSCs

Due to their limited expansion potential the extraction of primary MSCs from a succession of different donors is inevitable. Therefore, the potential inter-donor variability of MSCs regarding their invasion potential was evaluated. Invasion assays were performed with MSCs derived from different donors and tissues, and extracted in different laboratories. These included GMP conforming and nonconforming procedures.

HUH7 spheroids grown on polyHEMA were used to compare the invasive capacity between three apceth-derived MSC batches (AP), and five MSC isolates established in our laboratory (hBMSC). AP and hBMSC both were bone marrow-derived, and were in passage three. AP were isolated and cultured with GMP conforming protocols in Bio-1, and hBMSC with GMP nonconforming protocols in DMEM culture medium. The invasion potential did not differ significantly between the various batches obtained from apceth (AP, **Figure 11 A**). In contrast, the variability between MSCs extracted from different donors in our laboratory was greater (hBMSC, **Figure 11 A**). Pooling all samples from each source revealed an overall higher difference between different source laboratories that was greater than that seen between different donors (**Figure 11 B**). A significantly deeper invasion was detected with cells extracted and cultured in our laboratory. A third source of MSCs was then evaluated. Two umbilical cord subendothelial-derived batches (MSC 101003M and MSC 110501M) and one umbilical cord blood-derived MSC isolate (YI-1) were established at the LMU Institut für Prophylaxe und Epidemiologie der Kreislaufkrankheiten (PD Dr. Wolfgang Erl), and cultured in DMEM culture medium to passage three. The subendothelial umbilical cord MSCs reached an invaded depth that was different in its median, but similar in the maximal distance measured (**Figure 11 A**). When pooled, their invasion potential was found to be significantly higher than that seen for the bone marrow derived isolates, whereas blood-derived umbilical cord YI-1 was shown to invade at a significantly reduced efficiency into the experimental tumor spheroids (**Figure 11 B**).

Overall, the variability in their invasion potential into tumor spheroids between MSC isolates was only marginally dependent on the donor, but appeared to be dominated by differences in the isolation and culture conditions in the respective source laboratory. In addition, the tissue from which the MSCs are isolated appeared to have a significant impact on the migratory behavior. As reported elsewhere, MSCs isolated from different sources indeed displayed a different composition of homing molecules (Becker and van Riet 2016).

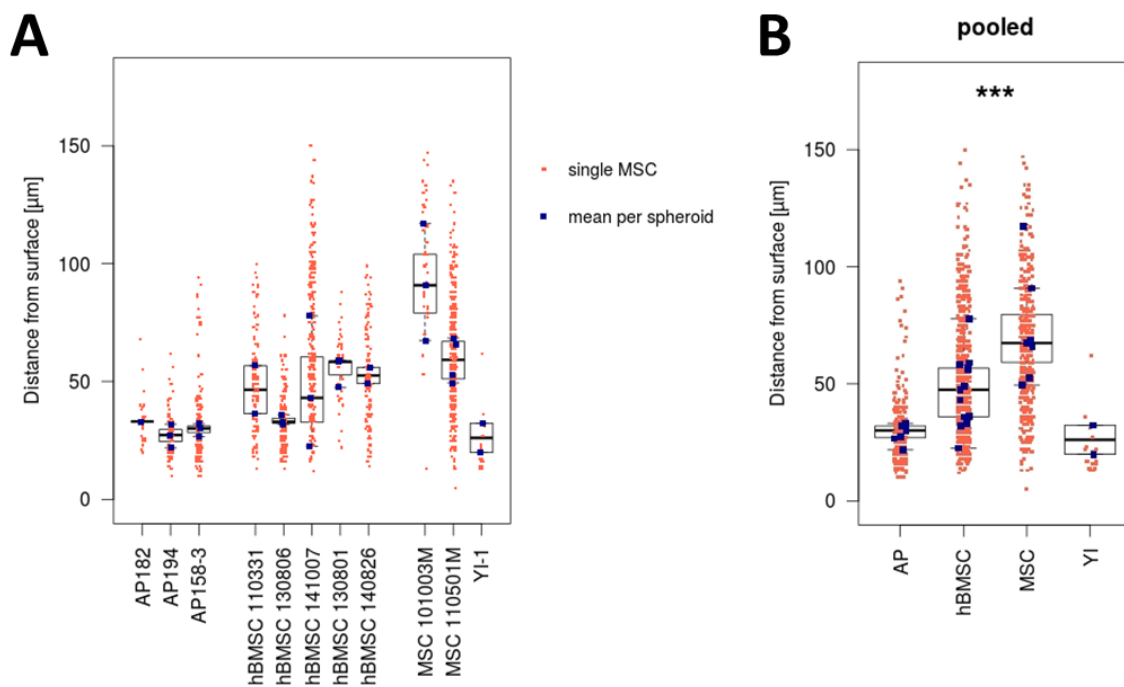


Figure 11 Invasion potential of different MSCs from different donors and sources into HUH7 tumor spheroids.

(A) Comparison of primary MSCs extracted from the bone marrow of three different donors at apceth (AP) and derived from five different donors in our laboratory (hBMSC), as well as MSCs extracted from the umbilical cord at the Institut für Prophylaxe und Epidemiologie der Kreislaufkrankheiten, LMU Munich, two batches subendothelial tissue-derived (MSC) and one blood-derived (YI-1). AP were cultured in Bio-1 and hBMSC, MSC and YI-1 in DMEM culture medium. All cells were in passage three. Invasion was conducted for 24 h into HUH7 spheroids grown on polyHEMA to a size of approximately 300 μm in diameter. (B) For direct comparison of tissues and extraction conditions, results were pooled according to the four sources. Red scatterplots show measurements of the shortest distance from the centroid of each MSC to the spheroid surface based on automated analysis of invasion depths via nuclear single cell segmentation. Blue scatterplots depict mean distances per spheroid and whisker-boxplots their distribution, with boxes showing the quartiles and median values and whiskers the rest of the distribution without outliers; Mann-Whitney U test comparing mean values per spheroid, ***p-value < 0.001 between all sources.

6.2.3 Conventional migration assays support source-dependent differences in the ability of MSCs to respond to tumor-derived signals

In addition to the tumor spheroid invasion potential, the migratory ability of MSCs along a tumor cell-derived chemoattractant gradient was characterized using a μ-slide Chemotaxis 3D system from ibidi (Munich, Germany). In this assay, primary bone marrow-derived MSCs from apceth (GMP conforming conditions), or cells established in-house were seeded into a collagen gel matrix between

two chambers that were filled with chemoattractants or control media. Cell movement within the inter-chamber observation area was then imaged and analyzed as described (see Methods, 5.4.1).

Of the MSC isolates analyzed above, three apceth-derived batches (AP182, AP194 and AP158-3) as well as four batches derived from our laboratory (hBMSC 110331, hBMSC 130806, hBMSC 141007 and hBMSC 140826) were investigated regarding their migratory behavior towards HUH7-conditioned medium. All MSCs were in passage three, while the AP cells were cultured in Bio-1, and the hBMSCs were grown in DMEM culture medium. In addition to the HUH7-conditioned chemoattractant gradient in the inter-chamber area, two controls were performed for each experiment, where both chambers were filled either with fresh culture medium (negative control) or with HUH7-conditioned medium. Five migration parameters were subsequently analyzed: forward migration index along the gradient axis y (yFMI), directionality, velocity, accumulated migrated distance, and euclidean migrated distance. Results were then pooled according to the source laboratory, apceth (AP) or our laboratory (hBMSC). All five values were found to be significantly higher when a HUH7 supernatant gradient condition was compared to both controls (**Figure 12 A and B**). The results for migration relevant parameters of both controls indicated a lower variability between the apceth-derived cells in general, and an additional synchronizing effect of the HUH7-conditioned medium (**Figure 12 C**). When comparing both sources, every parameter assessed under the gradient condition revealed a significantly enhanced migration potential of the in-house derived hBMSCs over that seen with the AP cells (**Figure 12 D**).

Thus, in line with the enhanced invasion into tumor spheroids, MSCs from our laboratory also displayed a significantly higher migratory activity in a 3D collagen matrix in response to tumor-derived chemoattractant gradients.

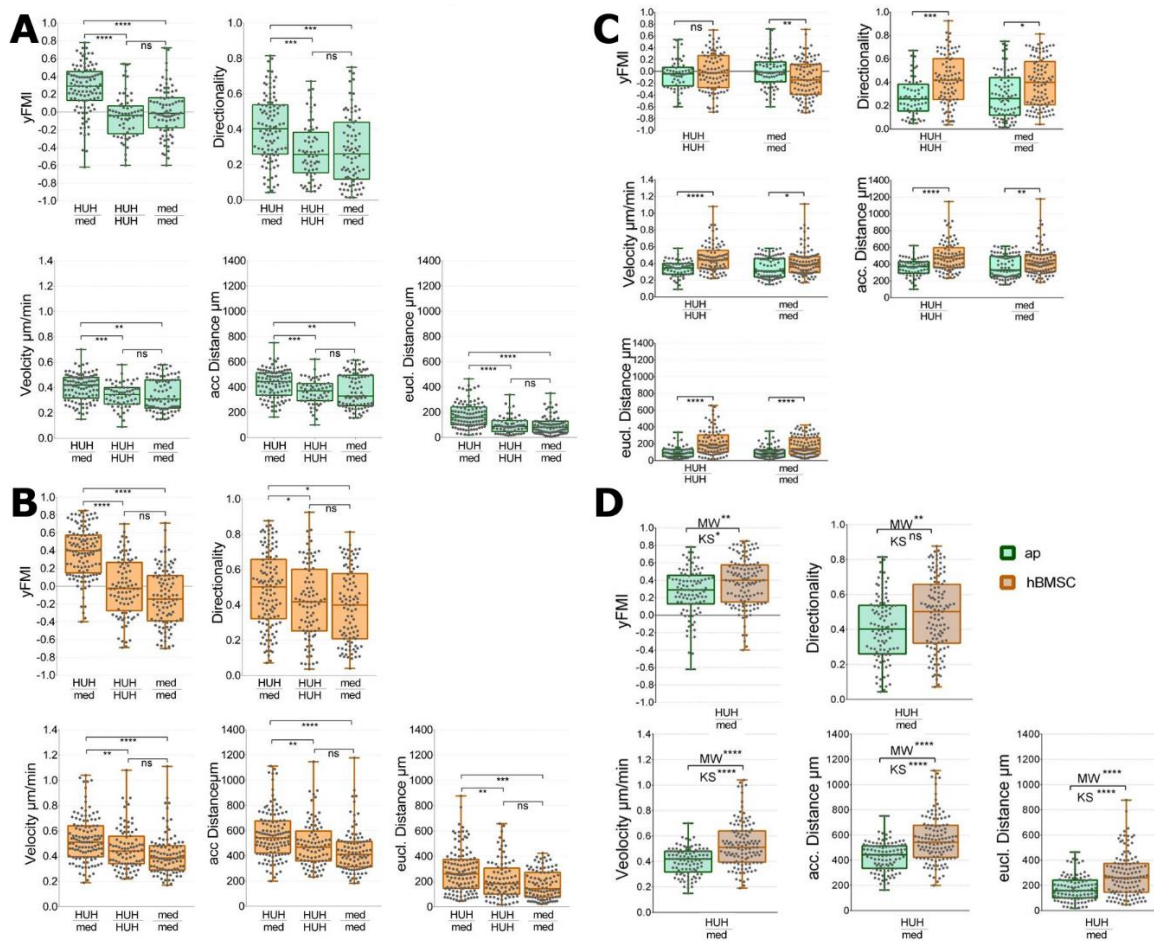


Figure 12 Migration of human bone marrow-derived MSCs derived from different donors towards HUH7 conditioned supernatant, pooled according to their source laboratory. MSCs (three batches from apceth – AP, four batches from our laboratory - hBMSC) were in passage three. AP cells were cultured in Bio-1, and hBMSC in DMEM culture medium. The cells were seeded in a collagen gel matrix in the 3D observation area of ibidi μ -slides. The chambers were filled with HUH7-conditioned medium on the one side, and fresh medium on the other, or as controls with either HUH7-conditioned medium, or fresh medium in both chambers. Cells were imaged over-night using widefield microscopy. Cell movement was tracked and migration relevant parameters analyzed using the ibidi chemotaxis and migration tool. Shown are the pooled results from each source, AP MSC (blue) (A) and hBMSC (orange) (B) alone, and in comparison in control conditions (C) and gradient-dependent (D); Scatterplots show measurements of single cells and whisker-boxplots their distribution, with boxes showing the quartiles and median values and whiskers the rest of the distribution; Kolmogorov-Smirnov test (KS) and, if indicated, Mann-Whitney U test (MW), ns = not significant, *p-value < 0.05, **p-value < 0.01, ***p-value < 0.001, ****p-value < 0.0001; the assay was performed in cooperation with Alexandra Wechselberger (Prof. Peter Nelson’s laboratory).

6.2.4 DMEM culture medium with FCS enhances the invasion potential of primary MSCs into experimental tumors

The significant deviation in the migratory capacity of MSCs extracted and cultured in different laboratories suggested an effect of differing isolation or culture conditions on the ability of MSCs to respond to experimental tumor signals, and on their resulting potential to invade into tumor spheroids.

The primary bone marrow-derived MSCs were isolated and cultured in apceth's GMP conforming laboratory using a proprietary medium containing human serum (Bio-1). To determine if the migratory capacity of the MSCs could be altered by culture media components, a GMP-derived MSC isolate was split into two and cultured in parallel using the GMP conditions and standard culture DMEM medium containing 10 % FCS for 48 h. The latter was shown to significantly enhance invasion into spheroids, approximately doubling the average migrated distances seen with the GMP medium (Figure 13).

This result suggests that the variances found between MSCs derived from apceth and our laboratory as shown above (Figure 11) are likely due to the effects of differing media supplements. The enhanced invasion potential shown in Figure 10 is probably due to culturing MSCs in FCS containing DMEM culture medium from passage three onward.

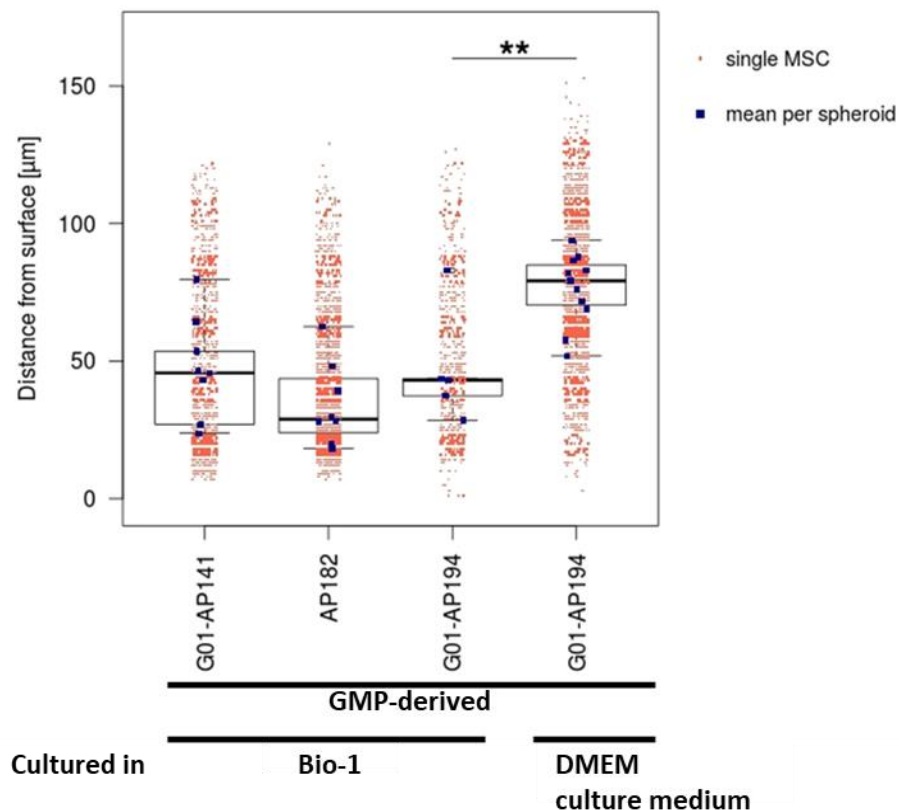


Figure 13 Invasion potential of differently cultured primary human bone marrow-derived MSC batches into HUH7 tumor spheroids. Invasion of GMP derived MSC batches G01-AP141, AP182 and G01-AP194 cultured

under GMP conditions with Bio-1 medium (DMEM low glucose, 1 U/ml Heparin, 6% platelet concentrate, 5% human FFP), and G01-AP194 cultured in parallel in DMEM culture medium with 10 % FCS (DMEM low glucose with GlutaMAX™ Supplement and pyruvate, 10 % FCS, 1 % Penicillin/Streptomycin) for 48 h. Invasion was conducted for 24 h in spheroids that were grown in hanging drops for 3 d to a size of approximately 300 µm in diameter. On average 10 spheroids per condition were analyzed. Red scatterplots show measurements of the shortest distance from the centroid of each MSC to the spheroid surface based on automated analysis of invasion depths via nuclear single cell segmentation. Blue scatterplots depict mean distances per spheroid and whisker-boxplots their distribution, with boxes showing the quartiles and median values and whiskers the rest of the distribution without outliers; Mann-Whitney U test comparing mean values per spheroid, ** p-value < 0.01.

6.2.5 Continuously cultured and freshly thawed MSCs show similar invasion into tumor spheroids

The storage and transport of engineered MSCs in a frozen state would facilitate their use in clinical settings. To rule out an effect of freezing and thawing, cryopreserved MSCs were thawed directly prior to invasion and compared to MSCs taken from continuous culture. The former were CMFDA stained before freezing so that they could be confronted with spheroids directly after thawing. The same experiment was then conducted with native and genetically modified (transduced with the RANTES-HSV-TK therapy construct) MSCs from the same donor (AP182 and G01-AP182). All batches were cultured in Bio-1 and were in passage three when applied to the spheroids. **Figure 14 A** depicts the results from both experiments, revealing no significant differences between cultured and frozen MSCs of each batch.

This suggests that storage and transport of MSCs in a frozen state, or thawing directly before application can be implemented into the clinical workflow.

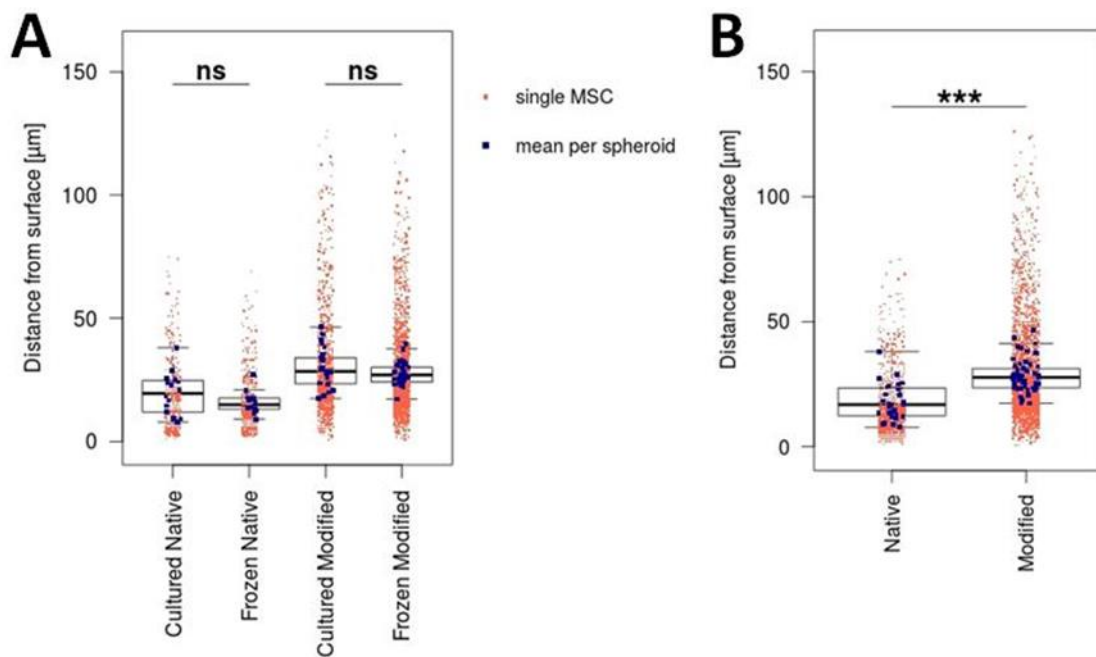


Figure 14 Invasion potential into HUH7 spheroids of native or genetically modified primary bone marrow-derived MSCs taken from continuous culture or frozen stocks. Cells thawed immediately prior to invasion were CMFDA stained before cryopreservation. All MSCs were cultured in Bio-1 and were in passage three at the time of invasion. Invasion occurred for 24 h into HUH7 tumor spheroids grown in hanging drops for 3 d to a size of approximately 300 μm in diameter. Spheroids were fixed, stained with 7-AAD and imaged via SPIM. MSCs were analyzed based on cytoplasmic segmentation and measurement of the shortest distance of each MSC or MSC cluster to the spheroid surface. At least 12 spheroids per condition were analyzed (A). (B) shows pooled results of cultured and frozen MSCs according to their native or modified condition. Red scatterplots show measurements of single MSCs, blue scatterplots depict mean distances per spheroid and whisker-boxplots their distribution, with boxes showing the quartiles and median values and whiskers the rest of the distribution without outliers; Mann-Whitney U test comparing mean values per spheroid, ns = not significant, ***p-value < 0.001.

6.2.6 Viral transduction of MSCs enhances their invasion potential

To introduce the therapeutic transgene into MSCs genetic modification is required. Viral transduction was employed here as the method of choice to stably engineer transgenes into primary human MSCs. The invasion assay was employed as described above to determine if the procedures involved during viral transduction impacted MSC invasion potential.

Figure 14 B shows the invasion depths of pooled cultured and frozen lots for a comparison of native versus modified MSCs. Viral transduction with the RANTES-HSV-TK therapy construct significantly enhanced the invasion potential of those primary bone marrow-derived MSCs.

The results presented suggest that the exposure of primary human MSCs to procedures such as viral transduction, and expansion in xenogeneic FCS enhanced their invasion potential into *in vitro* tumor spheroids. These modifications appear to modify MSCs in a way that they are more actively invasive than naive MSCs extracted and cultured under GMP conditions.

6.3 RANTES-induction in engineered MSCs within the tumor spheroid milieu

Recruitment to tumor sites is essential for the use of engineered MSCs as vehicle for therapeutic agents. However, when the cells are systemically applied, they not only home to tumors and metastases, but they may also migrate to healthy and injured non-tumor tissues. Expression of the therapy transgene in normal tissue settings may then represent a potential side effect of this MSC-based approach. The selectivity of transgene expression can be controlled to a degree by the use of tissue-specific gene promoters. Since MSCs are known to respond to different tumor-derived signals and to differentiate into specific tumor-associated cell types, related promoters have been used to limit therapy gene expression to cancer sites.

As a next set of experiments, we sought to determine if invasion of MSCs into tumor spheroids could also be used to measure the induction of transgene expression driven by a cancer-tissue associated gene promoter that is currently being used in the context of phase I and II clinical trials (Niess et al. 2015; Einem et al. 2017). Niess et al. first published the use of MSCs engineered with the therapy gene herpes simplex virus thymidine kinase under control of the human RANTES gene promoter (Niess et al. 2011). The RANTES gene promoter is generally thought to be activated by proinflammatory stimuli. Tumors *in vivo* have been shown to result in a robust induction of RANTES (Niess et al. 2011), but it was not clear if this could be efficiently modeled using *in vitro* cell culture. To test this, co-cultures of engineered primary bone marrow-derived MSCs and HUH7 tumor cells in 2D and 3D cultures were analyzed with regards to RANTES-driven induction of gene expression.

MSCs engineered with a constitutively expressed HSV-TK construct (EFS-HSV-TK construct in AP182 TD) were used to implement immunohistochemistry detection of a HVS-TK attached hemagglutinin (HA)-tag after invasion into HUH7 spheroids. **Figure 15** shows reliable detection of HSV-TK expression in the engineered MSCs on cryosectioned spheroids.

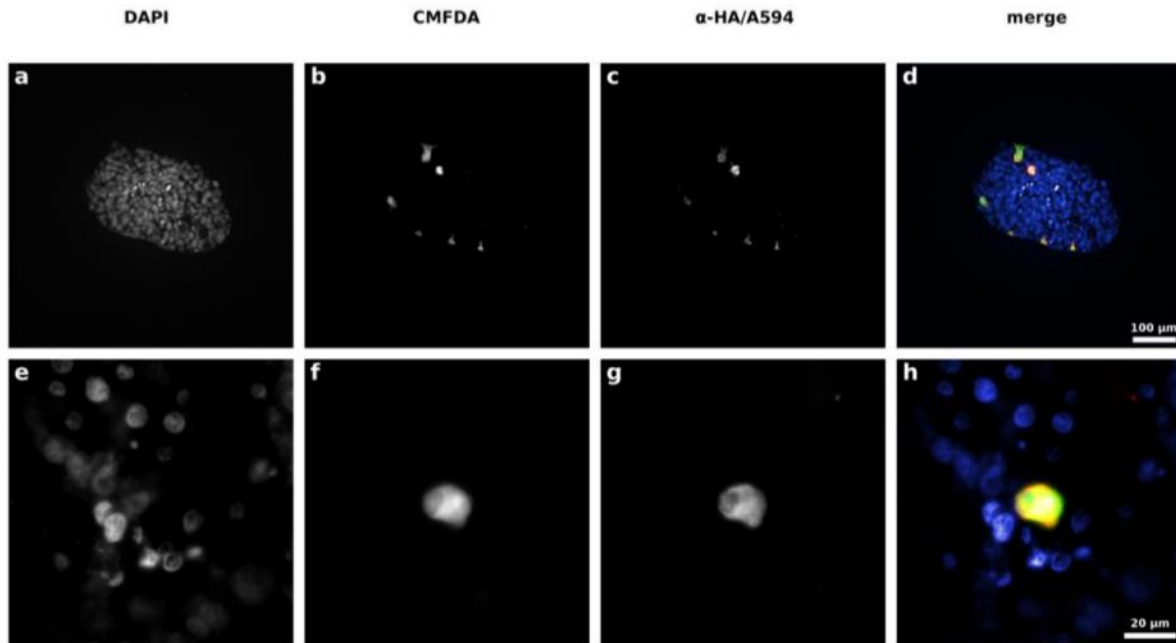


Figure 15 HSV-TK expression in MSCs engineered with a constitutive therapy gene construct after invasion into HUH7-spheroids. Primary human bone-marrow derived MSCs engineered with a constitutive EFS-HSV-TK construct were CMFDA labeled prior to a 24 h invasion into HUH7 spheroids. After fixation, the spheroids were cryosectioned and HSV-TK expression visualised via immunohistochemistry against an integrated HA-tag.

MSCs engineered with the therapeutic RANTES-HSV-TK construct (G01-AP182) were then used to investigate environment-dependent RANTES-induction. The results are summarized in **Figure 16**. MSCs cultured as a monolayer with, or without, 10 % FCS for 24 h showed no HSV-TK expression (**Figure 16 A**). Co-cultures with HUH7 tumor cells in monolayer for 24, 48 or 72 h at a ratio of 1:1, revealed a RANTES-induction in 44, 36 and 59 % of MSCs, respectively. However, when the MSCs were tested in the spheroid assay, after an invasion period into HUH7 spheroids of 24, 48, and 72 h only 26, 23 and 14 % of MSCs showed gene expression, respectively. In spheroids, the decrease over time was significant (**Figure 16 B and C**).

This reduced transgene expression over time indicated impeding parameters within the 3D spheroid milieu, the individual determination of which would require further investigation.

A

	t	Total n MSCs	n HSV-TK+ MSCs	Induction ratio	
Monolayer	+ FCS	24 h	364	0	
	- FCS	24 h	200	0	
	Co-culture with HUH7	24 h	39	17	0.44
		48 h	22	8	0.36
		72 h	81	48	0.59
Spheroid	Invaded into HUH7 spheroids	24 h	238	62	0.26
		48 h	275	62	0.23
		72 h	363	51	0.14

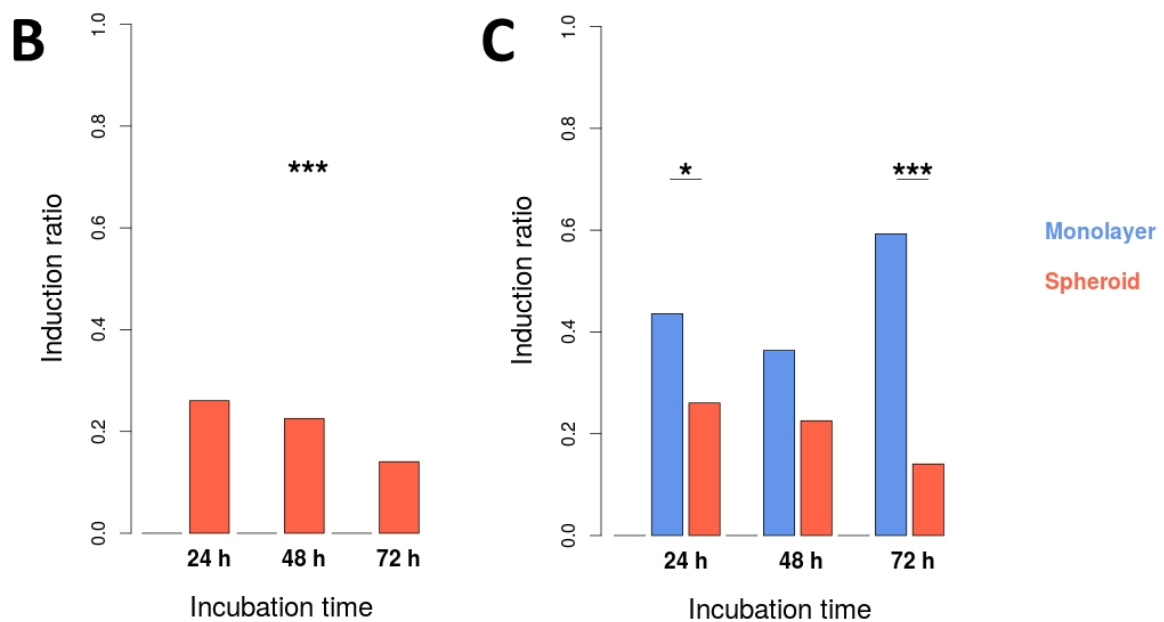


Figure 16 HSV-TK expression under the control of the RANTES-promoter in engineered primary bone marrow-derived MSCs in monolayer or after invasion into HUH7 spheroids. MSCs engineered with therapeutic RANTES-HSV-TK construct were CMFDA stained and cultured with or without FCS, or in co-culture with HUH7 cells, or invaded into HUH7 spheroids for 24, 48 or 72 h. Spheroids were fixed and cryosectioned. (A) Summary of HSV-TK expression in all conditions detected via immunohistochemistry against the integrated HA-tag. (B) Ratios of HSV-TK positive MSCs to total MSC numbers, comparing spheroids alone over time or (C) to monolayer co-cultures; Chi-squared test, *p-value<0.05, ***p-value<0.001.

6.4 Effect of low and high avidity TCRs and chimeric co-stimulatory receptors on T cell invasion and tumor cell killing in a melanoma spheroid model

The adoptive transfer of CTLs represents a second important class of cell-based therapy approaches for the treatment of cancer. For the second part of this thesis, the potential application of the tumor spheroid assay was tested for the characterization of functional aspects of CTLs and related platforms in the context of experimental tumor invasion.

An open question in CTL-based tumor therapy is the impact of TCR avidity on the functional efficiency of CTLs. We hypothesized that the TCR avidity would influence the ability and speed of a CTL to migrate into experimental tumors. In addition, we proposed that the tumor spheroid model, with its specific milieu, could be exploited to obtain insight into the control of tumor growth by cytolytic T cells. Using a modified invasion assay protocol, various parameters linked to the effect of TCRs with either low or high avidity were studied, namely invasiveness, cytokine secretion and tumor growth control. In addition, the potential effect of a set of novel chimeric co-stimulatory receptors on similar parameters was evaluated.

For all subsequent experiments, primary human CTLs generated from peripheral blood mononuclear cells (PBMCs) of healthy donors were used. For each experiment, CTLs from one donor that had undergone two rounds of viral transduction were used. In the first transduction, the T cells were divided into three parts and transduced with either a low avidity D115-TCR, or with a high avidity T58-TCR, or mock transduced as controls. Transduction efficiency was generally approximately 60 % for both the D115- and T58-TCR vectors. In the second transduction, the D115-TCR transduced CTLs were divided into three parts. One D115 population was transduced with the chimeric co-stimulatory construct PD-1:28 and one with PD-1:BB, while the third D115-TCR as well as T58-TCR and Mock CTLs were mock transduced. The resulting CTL populations D115/Mock, D115/PD-1:28, D115/PD-1:BB, T58/Mock and Mock/Mock were stored frozen, thawed and cultured in parallel before used in experiments.

6.4.1 Effect of TCR avidity on CTLs' response to tumor cells

6.4.1.1 *TCR-gene modified CTLs react antigen-specific and with TCR avidity controlled intensity*

Low avidity D115- and high avidity T58-TCRs recognize the same tyrosinase (AA₃₆₆₋₃₇₇)-peptide, a well characterized melanoma associated antigen, presented on the MHC I allotype HLA-A2 (Wilde et al. 2009).

High avidity T58-TCR CTLs have been previously shown to elicit a stronger functional response in standard CTL assays (Wilde et al. 2009), an effect that was confirmed within this thesis. Using the

chromium-51 release assay as established standard assay for the quantification of cytotoxicity mediated target cell lysis, D115- and T58-TCR-transduced T cells showed specific recognition and functional response against HLA-A2⁺/Tyr⁺ melanoma cells SKMel23 and WM266.4, but no unspecific response was seen against HLA-A2⁺/Tyr⁻ A375 or HLA A2⁻/Tyr⁻ K562 tumor cells (**Figure 17 A**). Specific lysis of SKMel23 cells tended to be slightly higher by high avidity T58-TCR transduced CTLs. Anti-tumor Th1 type cytokine quantification from supernatants of 24 h co-cultures at a 1:2 effector to target cell (E:T) ratio also revealed HLA-A2/Tyr specificity for both TCRs, and a significantly higher cytokine secretion of the high avidity T58-TCR T cells (**Figure 17 B**).

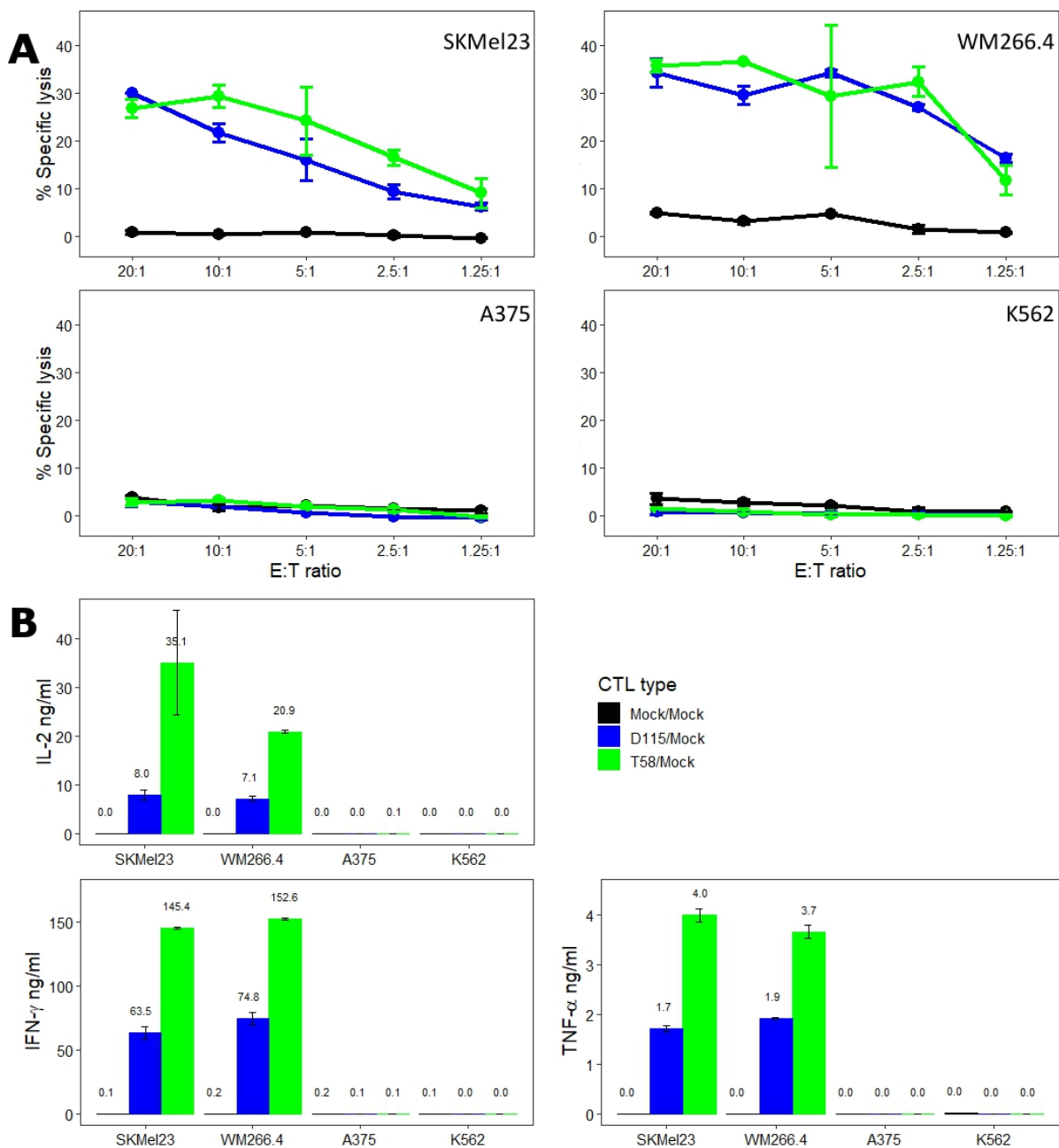


Figure 17 Cytotoxicity and cytokine responses of CTLs engineered with low or high avidity TCRs, or without TCR construct. Low avidity TCR (D115/Mock), high avidity TCR (T58/Mock) and unspecific non- (Mock/Mock)

transduced CTLs were stored frozen and thawed 4 to 10 d before the experiment. During culture, they were supplied with 50 U/ml rIL-2 every 3 days, with a final addition of 50 U/ml 2 d or 20 U/ml 1 d before the assay. (A) T cells were used as effector cells against ^{51}Cr -labelled SKMel23 (HLA-A2⁺/Tyr⁺), WM266.4 (HLA-A2⁺/Tyr⁺), A375 (HLA-A2⁺/Tyr⁻) and K562 (HLA-A2⁻/Tyr⁻) cells at depicted effector:target cell (E:T) ratios. Target cell lysis was assessed by detecting released ^{51}Cr after 4 h of co-culture. Shown are mean values of two replicates +/- standard deviation (SD). (B) T cells were stimulated with SKMel23, WM266.4, A375 or K562 cells at an E:T ratio of 1:2 (0.5×10^5 CTLs with 1×10^5 targets in 200 μl RPMI culture medium). Co-culture supernatants were harvested after 24 h and analyzed for IL-2, IFN- γ and TNF- α contents by ELISA. Depicted is the amount of cytokine secreted by 0.5×10^5 T cells (mean ng/ml of triplicates +/- SD). Cytokines in cultures of only tumor cells or only T cells were below 0.07 ng/ml for all cytokines.

6.4.1.2 High avidity TCR CTLs attack with higher frequency and kill significantly faster

Upon contact and antigen recognition, CTLs form immunological synapses and attack target cells via perforin and granzyme B release (Murphy and Weaver 2017). Accumulating hits by CTLs ultimately induce apoptosis of the target cells. Since perforin-mediated pore-formation also elicit Ca^{2+} influx (Keefe et al. 2005), time-resolved imaging of 2D co-cultures of CTLs and target cells loaded with the Ca^{2+} indicator Fluo-3 allowed monitoring of the chronology of T cell/target interactions (**Figure 18 A**). Formation of the immunological synapse and initial Ca^{2+} peak in the target cell were observed mainly within 3 - 8 min for both D115- and T58-TCR CTLs. After this first hit, however, the high avidity T58-TCR CTLs induced membrane blebbing, a sign of apoptosis (Coleman et al. 2001), after approximately 17 min, within a minimum of 8 and a maximum of 24 min. By contrast, the target cell blebbing mediated by the low avidity D115-TCR T cells occurred only after approximately 24 min, with a much higher variation ranging from a minimum of 1 to a maximum of 45 min (**Figure 18 B**).

Although the high avidity T58-TCR CTLs killed significantly faster, the target cells did not receive significantly less hits until membrane blebbing occurred (around 3 to 4, **Figure 18 C**). This suggests that the high avidity CTL delivered its hits within a shorter period of time, indicating a higher frequency. This is in accordance with Jenkins et al., who postulated that delivery of granules to the immunological synapse is triggered more efficiently with high avidity TCRs (Jenkins et al. 2009).

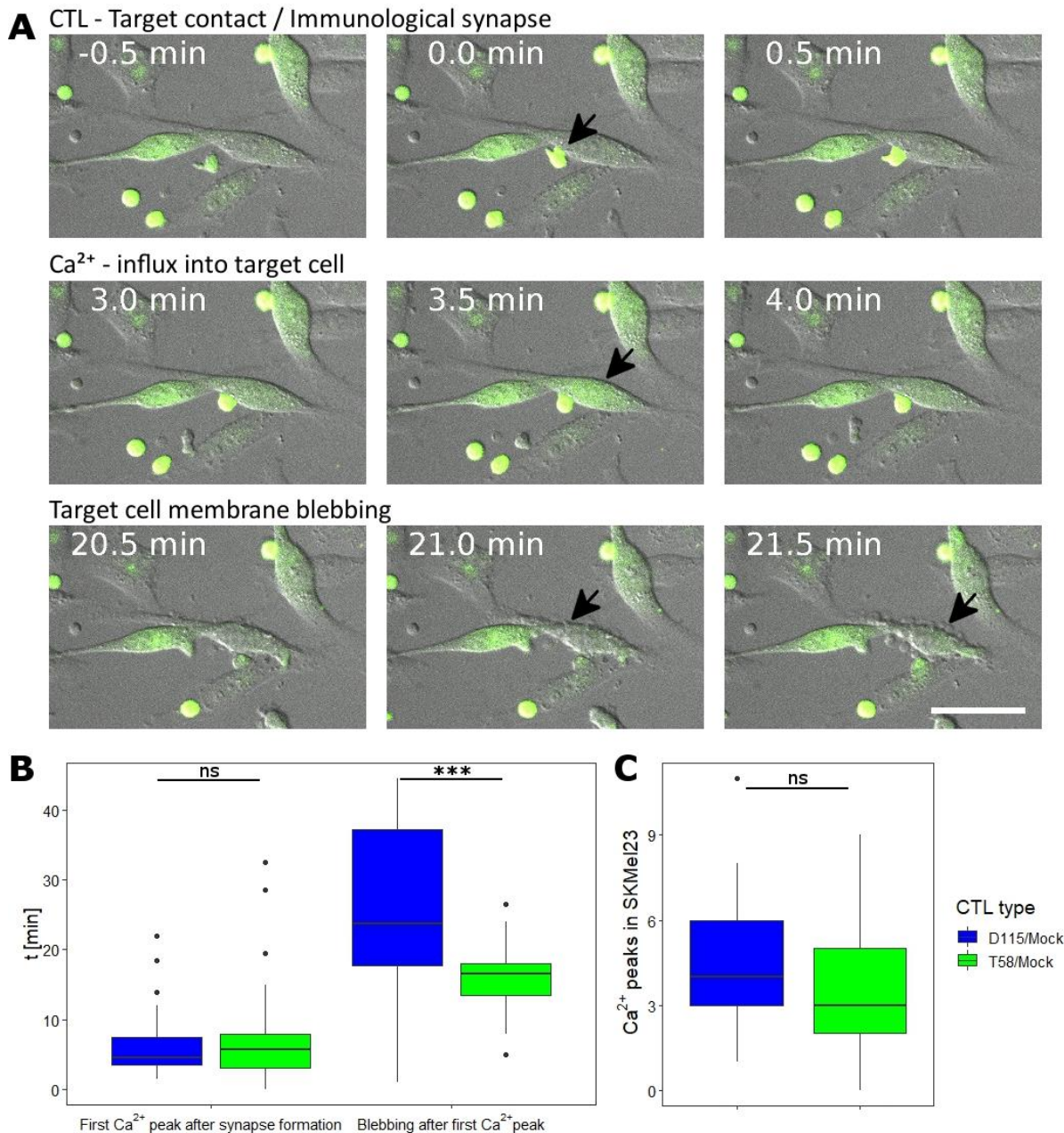


Figure 18 Chronology of interaction between D115/Mock or T58/Mock engineered CTLs and target cells. TCR engineered CTLs and SKMel23 were pre-stained with and then co-cultured in the presence of 2.5 μM Fluo-3 AM Ca^{2+} indicator staining (green). Images were taken every 30 sec. **(A)** Time series of microscopic images of T58-TCR CTLs (small and round) interacting with adherent SKMel23 target cells. CTLs form an immunological synapse (0 min), resulting in Ca^{2+} influx into the target cell (3.5 min) and target cell membrane blebbing (21 min); scale bar 50 μm . **(B)** Duration from synapse formation to first Ca^{2+} peak in the target cell and then to target cell blebbing, compared between D115/Mock and T58/Mock CTLs. **(C)** Numbers of Ca^{2+} peaks in target cells during the period from first Ca^{2+} peak to target cell membrane blebbing; $n = 30$ for each D115- and T58-TCR CTLs; whisker-boxplots show the distribution of cells, with boxes showing the quartiles and median values and whiskers the rest of the distribution, with outliers marked separately; Mann-Whitney U test, *** p -value < 0.001.

6.4.1.3 CTLs show TCR dependent invasion, tumor cell killing and cytokine secretion in a 3D spheroid model

As a next step, the effects of low and high avidity TCRs on CTL function were tested in the experimental 3D tumor models. The spheroid invasion assay was employed to assess potential differences in the invasion efficacy, and also in their cytotoxic response.

Three day old melanoma cell SKMel23 spheroids grown in hanging drops were confronted with CTLs for 30 min, washed, and further incubated for 1 h to 6 d individually in hanging drops, then fixed and imaged. CTLs did not form clusters as was seen with MSCs (compare **Figure 8** and **Figure 19**), thus they could be directly segmented via their cytoplasmic CMFDA signal using a 3D watershed algorithm. Nevertheless, whole spheroids were additionally stained with the nuclear dye 7-AAD after fixation to allow exact volume measurements.

Figure 19 shows midsections through 3D light sheet microscopy acquisitions of nuclear stained spheroids invaded by CellTracker CMFDA-labelled CTLs and controls. As can be seen, the spheroids offered a matrix for CTL attachment and invasion. After three days in the spheroid, however, the CellTracker signal was found to be heterogeneous and weak such that reliable detection of CTLs within different depths of the light scattering spheroids was not possible. Thus, further analysis of CTL numbers and invaded depths was only conducted for the shorter time frames of 1 h and 24 h.

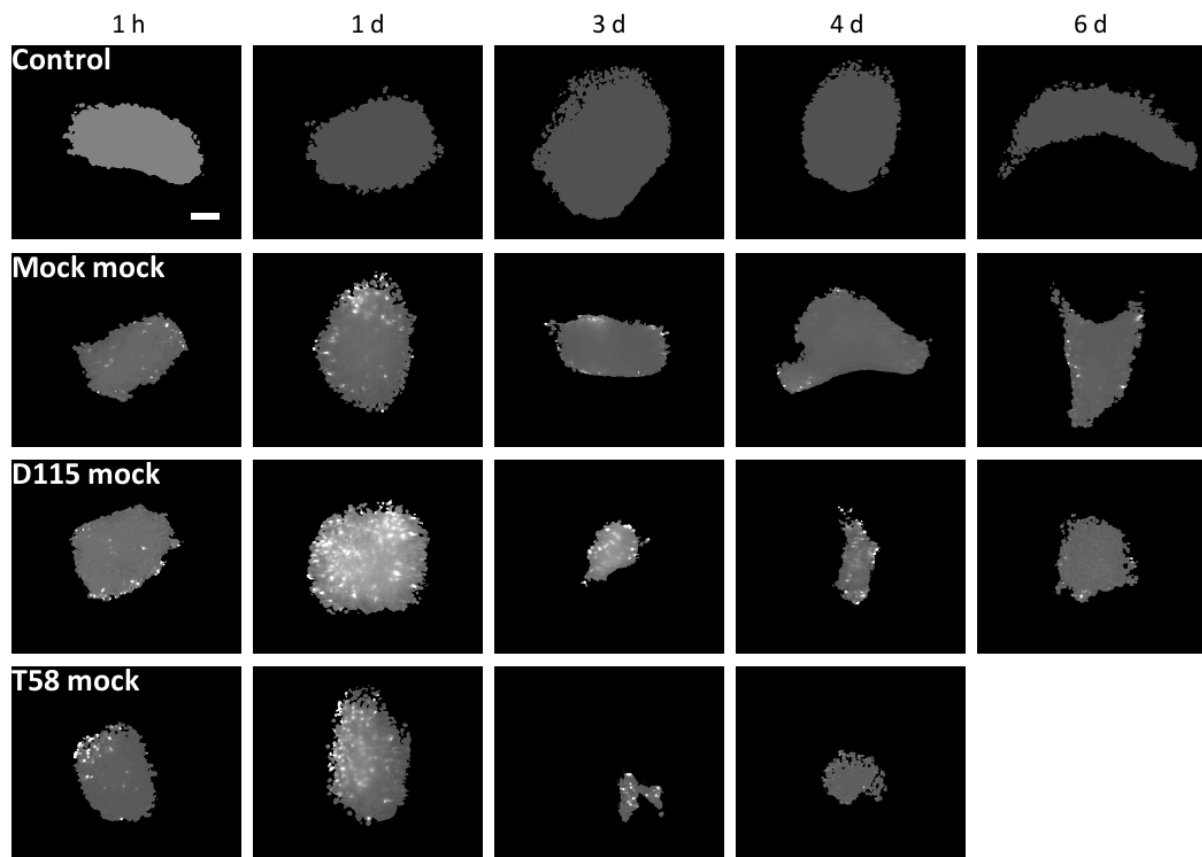


Figure 19 Imaging invasion of TCR-engineered CTLs into SKMel23 spheroids. D115/Mock, T58/Mock and unspecific Mock/Mock transduced CTLs were thawed 4 to 10 d prior to the experiment. During culture they were supplied with 50 U/ml rIL-2 every 3 days, with a final addition of 50 U/ml 2 d or 20 U/ml 1 d before the invasion assay. 1.5×10^4 CMFDA labeled CTLs each were confronted with single 3 d old SKMel23 spheroids grown in hanging drops to a size of approximately 300 μm diameter. After shaking for 30 min, the co-cultures were filled with 1 ml of medium to dilute CTLs that were still in suspension. The CTL-coated spheroids were recovered from the suspensions and re-seeded into hanging drops for 1 h, 1 d, 3 d, 4 d or 6 d. After fixation, spheroids were nuclear stained with 7-AAD and imaged via SPIM. Shown are midsections through 3D spheroid data sets, masked onto 7-AAD positive area (7-AAD signal not shown), displaying invaded CMFDA labeled CTLs; scale bar 100 μm .

In addition, the original protocol for invasion as established for the MSCs had to be modified to yield an equal starting number for the low and high avidity TCR engineered T cells attached to the spheroids. It was observed that after 30 min of co-incubation and subsequent washing of the spheroid to remove non-attached T cells, the numbers of the high avidity T58-TCR CTLs attached to the spheroid were always lower compared to those of the low avidity D115-TCR CTLs (data not shown). As a possible explanation we reasoned that the quicker killing activity of the high avidity T58-TCR CTLs (see section above, 6.4.1.2) caused the death of tumor cells at the spheroid rim within the 30 min attachment time. The subsequent three rounds of washing to get rid of excess CTLs then resulted in

the dissociation of this rim of dead or dying tumor cells from the spheroid and with it in the loss of T cells which were still attached to these tumor cells. The protocol was therefore modified omitting the washing step and, instead, applying a high dilution step to minimize the transfer of non-attached T cells to the further invasion culture.

Using the modified protocol, the analysis of T cell numbers on spheroids 1 h after washing still yielded lower values for the high avidity T58-TCR T cells than the low avidity D115-TCR T cells (**Figure 20 A**), but the effect was less pronounced. Mock-transduced CTLs without killing specificity were observed at highest numbers. After 24 h, the detected numbers in spheroids of the low and high avidity D115- and T58-TCR T cells were similar and both significantly higher compared to the numbers of the mock-transduced T cell control as well as to their numbers observed at 1 h of invasion time. Apparently, T cell numbers in spheroids increased by 2- to 3-fold within 24 h upon specific TCR recognition of cognate peptide-MHC complexes on tumor cells. While that increase required TCR specificity, it was independent of the avidity.

Now, it was asked if the avidity of the TCR influenced invasion depth into tumor spheroids. The method for measuring the invaded depths of CTLs was modified compared to that used for MSCs (see 6.1), which used the spheroid surface as the reference position. CTLs were observed to reduce spheroid volumes already within 24 h, possibly due to tumor cell killing mechanisms that caused tumor cell loss from the spheroid rim inwards. Therefore, the spheroid surface was no longer a constant reference position for the quantification of invaded depths as it was for MSCs. As an alternative, the distance of each T cell to the spheroid centroid was used as a new measurement for invasion, with a closer position to the centroid indicating deeper invasion. Applying this principle, it was observed that CTLs with a TCR specific for a cognate peptide-MHC complex on the spheroid tumor cells invaded closer to the spheroid centroid than CTLs with unspecific TCRs (**Figure 20 B**). However, the invaded depths were similar for low and high avidity D115- and T58-TCR CTLs.

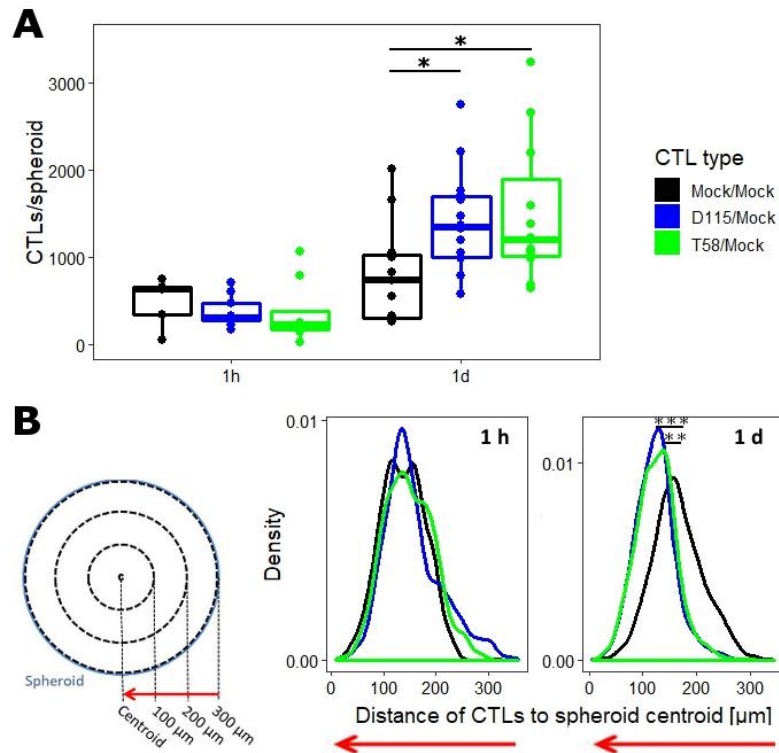


Figure 20 Analysis of TCR-engineered CTLs invaded into SKMel23 spheroids. Unspecific Mock/Mock, low avidity TCR D115/Mock and high avidity TCR T58/Mock CTL invaded spheroids were prepared as described in **Figure 19**. Three independent invasion experiments have been conducted with a total number of at least 5 analyzed spheroids per group. Shown are: **(A)** Numbers of watershed segmented CTLs per spheroid after 1 h or 1 d of invasion; each dot represents the number of CTLs in one spheroid and whisker-boxplots show their distribution, with boxes showing the quartiles and median values and whiskers the rest of the distribution without outliers; Mann-Whitney U test, * p-value < 0.05; **(B)** density estimation of the distribution of invaded distances to the respective spheroid centroid after 1 h and 1 d of invasion; Mann-Whitney U test, ** p-value < 0.01, *** p-value < 0.001 comparing mean distances per spheroid.

In a next step, the activity of the T cells to kill tumor cells grown as experimental 3D tumors was assessed. It turned out that detecting CTL cytotoxicity within spheroids on a single target cell level was problematic. SKMel23 spheroids were too dense to be efficiently penetrated by apoptosis marker dyes, or to optically segment and count the number of living, nuclear stained tumor cells. As an alternative, spheroid volumes were measured after different times of CTL invasion and used as a general read-out for CTL-associated control of experimental tumor growth. As depicted in **Figure 21 A**, after 1 h of CTL invasion, the volumes of all spheroids were largely similar independently whether the invading CTLs had no specific TCR (Mock/Mock CTLs) or a tumor-reactive TCR with low (D115/Mock CTLs) or high (T58/Mock CTLs) avidity, or whether no CTLs were present (Control). After 1 d of invasion, however, spheroid volumes were significantly reduced when invaded by CTLs with tumor-reactive TCRs, when compared to spheroids without CTLs, or non-tumor reactive CTLs.

Yet, there was no difference between the T cells expressing the low avidity D115-TCR or the high avidity T58-TCR. CTLs with antigen-specific TCRs D115 and T58 continued to reduce spheroid volumes until day 4, while volumes of spheroids without T cells or with antigen-unspecific T cells increased. After 6 d invasion, all spheroids that were invaded by T58-TCR CTLs had dissolved, whereas 11 % of the spheroids invaded by D115 CTLs were still intact, albeit presented with smaller volumes than the spheroids without or with unspecific T cells (**Figure 21 B**).

In addition to direct tumor cell killing cytokine secretion of T cells in spheroids was assessed. After 24 h of CTL invasion into spheroids supernatants from the hanging drop cultures were harvested and screened for CTL-secreted cytokines using the Bio-Plex Th1/Th2 kit. It was observed that supernatants of spheroids invaded by the T58-TCR T cells contained higher amounts of Th1 type cytokines IL-2, IFN- γ , TNF- α and GM-CSF than did the supernatants of spheroids with D115-TCR CTLs (**Figure 21 C**). This pattern recapitulated the results seen in the 2D co-cultures (**Figure 17 B**). Anti-inflammatory Th2 type cytokines IL-4 and IL-5 were below detection limits (data not shown).

The invasion assay has revealed that CTLs were able to reduce 3D tumor volumes if they expressed TCRs reactive to cognate peptide-MHC complexes on the tumor cells. CTLs with high avidity TCRs were able to dissolve all spheroids after 6 d while T cells with low avidity TCRs were less efficient. A stronger functional response of high avidity TCR CTLs within spheroids was also reflected by a higher Th1 cytokine secretion.

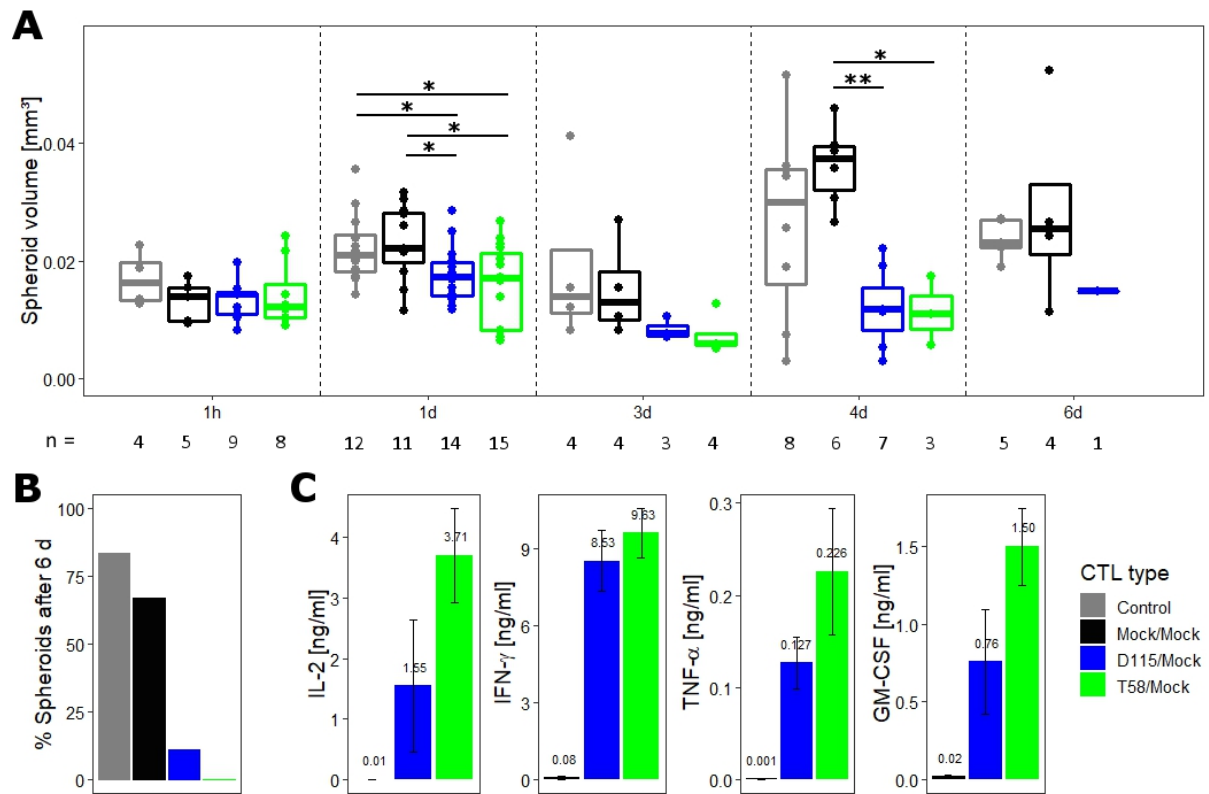


Figure 21 Effector function of TCR-engineered CTLs in SKMel23 spheroids. Unspecific Mock/Mock, low avidity TCR D115/Mock and high avidity TCR T58/Mock CTL invaded spheroids were prepared as described in **Figure 19**. Per condition a number of spheroids as indicated (n) were analyzed regarding: **(A)** spheroid volumes after incubation for the times indicated; each dot represents one spheroid and whisker-boxplots show their distribution, with boxes showing the quartiles and median values and whiskers the rest of the distribution without outliers; Mann-Whitney U test, * p-value < 0.05, ** p-value < 0.01; **(B)** percentages of spheroids still present after 6 d of all spheroids prepared for that timepoint; **(C)** cytokine IL-2, IFN- γ , TNF- α and GM-CSF levels detected by Bio-Plex in pooled hanging drop supernatants after 1 d of CTL invasion into SKMel23 spheroids (corresponds to approximately 5×10^7 CTLs/ml; mean ng/ml of triplicates +/- SD).

6.4.2 Effect of chimeric co-stimulatory receptors on T cell function in 3D spheroid models

CTLs used for adoptive T cell therapy often display low persistence and lose efficacy after injection into the patient. The co-stimulation pathway through CD28 provides survival signals to T cells and enhances the T cell's functional capacity. Based on this knowledge and integrating new information on tumor-expressed proteins a novel strategy for enhancing the functional activity of CTLs uses chimeric receptors for CTL co-stimulation (Prosser et al. 2012; Ankri et al. 2013). Here, the developed 3D spheroid system was applied to characterize the effect of two novel chimeric co-stimulatory proteins on T cells in the context of low and high avidity TCRs.

6.4.2.1 Chimeric co-stimulatory receptors upgrade CTL response in dependency of PD-L1 expression on targets

The surface proteins CD80 and CD86 that interact with the co-stimulatory CD28 molecule on T cells are often absent on tumor cells of solid tumors. By contrast, the inhibitory PD-1 ligand (PD-L1) is typically upregulated on tumor cells which is thought to help protect the tumor cell from CTL activity. Dr. Ramona Schlenker (Prof. Elfriede Nölsner's laboratory) has linked the external domain of the inhibitory PD-1 protein to an internal domain of one of the co-stimulatory proteins CD28 or 4-1BB creating two chimeric co-stimulatory receptors, PD-1:28 and PD-1:BB (Schlenker 2015). In case of the PD-1:28 construct, the extracellular domain of the PD-1 construct was fused with the transmembrane and intracellular domains of CD28, whereas for the PD-1:BB construct the transmembrane domain of PD-1 was used successfully (**Figure 22 A**). Interacting with PD-L1 on tumor cells these PD-1 chimeric proteins should induce the CD28 or 4-1BB co-stimulatory pathway in the T cells instead of the inhibitory pathway the native PD-1 protein would activate (**Figure 22 B**).

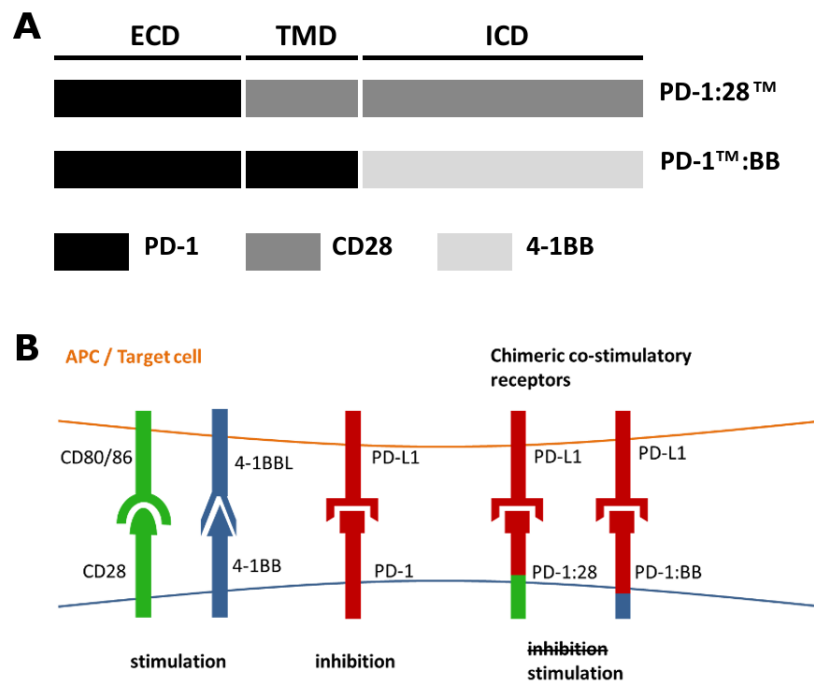


Figure 22 Chimeric co-stimulatory receptors PD-1:28 and PD-1:BB. (A) Scheme of extracellular (ECD), transmembrane (TMD) and intracellular domains (ICD) of chimeric co-stimulatory receptors that (B) turn inhibition through native PD-1 into stimulation through CD28 or 4-1BB induced pathways.

These constructs were transduced in concert with the low avidity TCR D115 to evaluate potential boosting effects that were compared to CTLs expressing the high avidity TCR T58. Since the functional performance of T cells changes with culture conditions (cytokines, time of culture) all differently transduced cell types (D115/Mock, D115/PD-1:28, D115/PD-1:BB and T58/Mock) had the same transduction and culture history when used in the same experiment (as described in 5.1.5).

The cytotoxicity of D115 T cells expressing either PD-1:28 or PD-1:BB was first compared to that of D115/Mock and T58/Mock T cells in a standard chromium release assay. It was observed that the killing activity against the natural melanoma cell line SKMel23 grown in standard monolayer culture was similar for all four T cell lines, independently of the TCR avidity (D115 or T58) with no effect seen for the chimeric proteins PD-1:28 or PD-1:BB (**Figure 23 A**). To further assess effects in dependency of the crucial target markers tyrosinase and PD-L1 a HEK293 model system established in our laboratory was used. HEK293 expressing PD-L1 only (HEK293/PD-L1) were not killed by any of the T cells specific for the tyrosinase peptide-MHC complex, indicating that the chimeric receptors did not induce effector function by themselves. Using HEK293 expressing tyrosinase alone (HEK293/Tyr) or in addition to PD-L1 (HEK293/Tyr/PD-L1) as target cells induced higher killing activity in CTLs expressing high avidity T58-TCR compared to low avidity D115-TCR. Importantly, expression of the chimeric receptors PD-1:28 or PD-1:BB only enhanced killing activity in D115 T cells confronted with

HEK293/Tyr/PD-L1, while no effect was seen when HEK293 expressed tyrosinase alone without PD-L1.

T cell secreted cytokine IFN- γ levels after 10 h and 24 h co-culture with target cells were measured as an additional effector function (**Figure 23 B**). While SKMel23 target cells provoked a stronger response by CTLs expressing the high avidity T58-TCR, IFN- γ secretion was comparable between CTLs expressing D115-TCR alone or together with one of the chimeric receptors PD-1:28 or PD-1:BB. With the HEK293 system the cytokine secretion assay again revealed an enhancing effect of the chimeric receptors only when PD-L1 was expressed, similar to the results of the chromium release assay. Confronted with HEK293/Tyr/PD-L1 D115-TCR CTLs expressing PD-1:28 or PD-1:BB secreted IFN- γ at levels higher than CTLs with D115-TCR alone, but lower than CTLs with T58-TCR.

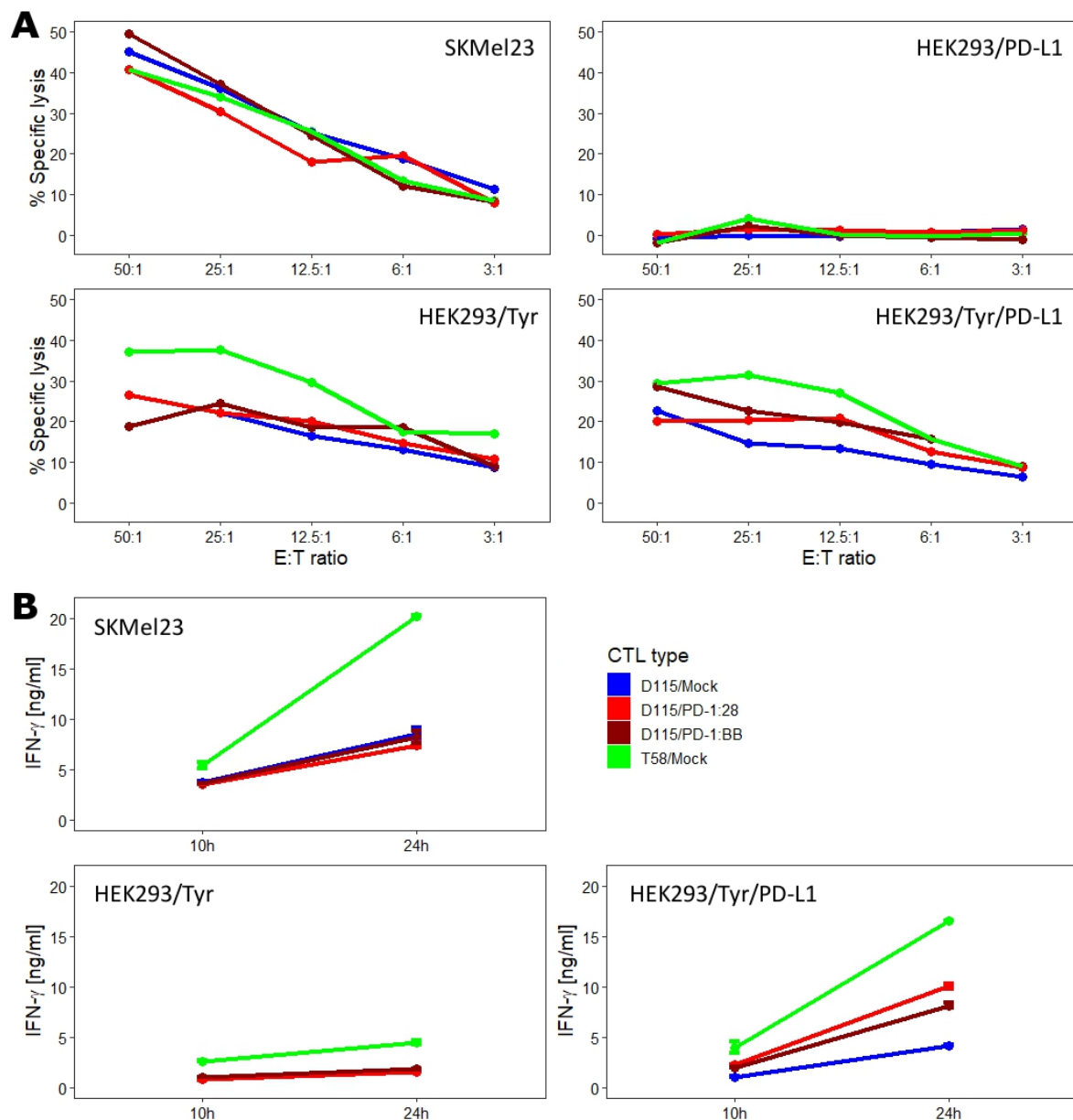


Figure 23 Cytotoxicity and cytokine responses of CTLs engineered with low avidity D115-TCR alone or together with chimeric co-stimulatory proteins. D115/Mock, D115/PD-1:28, D115/PD-1:BB and T58/Mock CTLs were stored frozen and thawed 4 to 10 d before the experiment. During culture, they were supplied with 50 U/ml rIL-2 every 2 or 3 d, with a final addition of 50 U/ml 2 d or 20 U/ml 1 d before the assay. (A) T cells were used as effector cells at depicted E:T ratios against ^{51}Cr -labelled SKMel23 melanoma cells or HEK293 cells transduced to express PD-L1 (HEK293/PD-L1), tyrosinase (HEK293/Tyr) or both (HEK293/Tyr/PD-L1). Target cell lysis was assessed by detecting released ^{51}Cr after 4 h of co-culture. (B) T cells were stimulated with SKMel23 or HEK293/Tyr or HEK293/Tyr/PD-L1 cells at an E:T ratio of 1:1 (2.5×10^4 of each cell type in 200 μl RPMI culture medium). Co-culture supernatants were harvested after 10 h and 24 h and analyzed for IFN- γ levels by ELISA. Depicted is the amount of cytokine secreted by 2.5×10^4 T cells (mean ng/ml of triplicates \pm SD).

6.4.2.2 PD-L1 surface expression gets upregulated in spheroid culture

To determine why no enhancing effect was seen for melanoma cell lines expressing the cognate Tyr/HLA-A2 endogenously, the PD-L1 expression on melanoma lines was determined by flow cytometry analysis (Figure 24). It was observed that SKMel23 cells grown in standard monolayer had very low to no detectable PD-L1 expression on the cell surface, while PD-L1 was readily detected on a renal cell carcinoma cell line RCC26. Culturing SKMel23 in hanging drops and growing them to spheroids of a size of 0.015 to 0.02 mm³ within 3 d increased PD-L1 expression on tumor cells.

The alternative PD-1 ligand PD-L2 was found to be expressed at similar levels in both 2D and 3D cell culture conditions. Additionally, a significantly higher HLA-A2 surface expression was observed when SKMel23 cells were cultured in spheroids compared to 2D cultures.

Since triggering the chimeric receptors requires the expression of its ligand PD-L1, the spheroid model seemed suitable to evaluate the biologic effects of the stimulatory receptors PD-1:28 and PD-1:BB in a more physiologic setting with unmodified tumor cells.

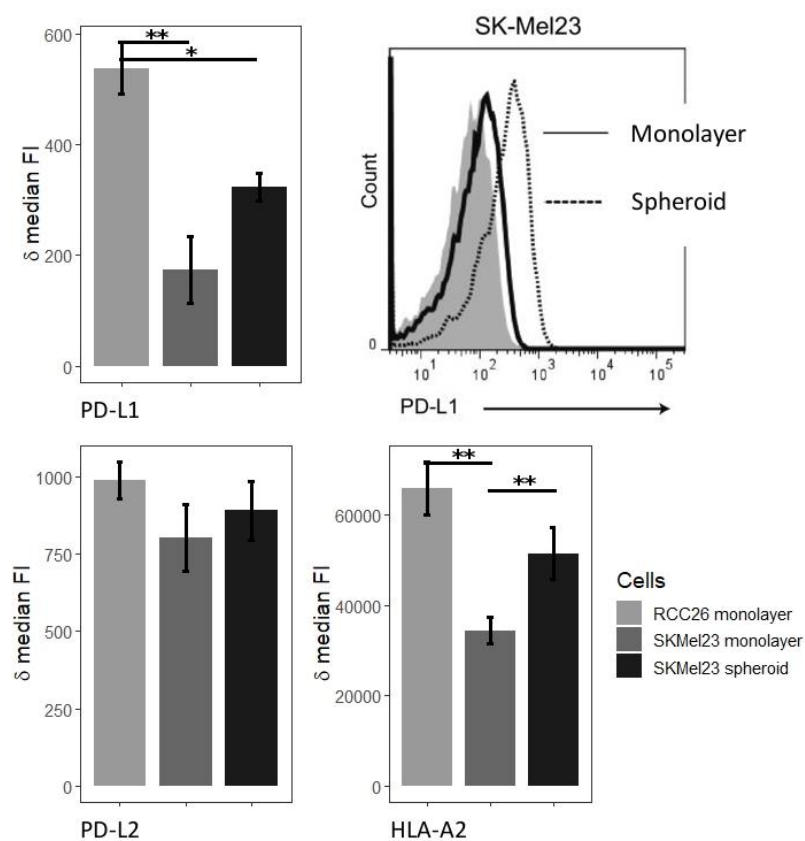


Figure 24 PD-L1, PD-L2 and HLA-A2 expression on SKMel23 melanoma cells. Surface expression on SKMel23 cells grown in 2D monolayer or 3D spheroids for 3 d in hanging drops was assessed via flow cytometry analysis. RCC26 renal cell carcinoma PD-L1 positive cells grown in monolayer served as control. Depicted are one exemplary histogram of PD-L1 antibody signals and delta (δ) median fluorescence intensity (FI) values of 4 experiments +/- standard error of the mean (SEM); Student's t test, *p-value < 0.05, **p-value < 0.001.

6.4.2.3 Chimeric co-stimulatory receptors mediate enhanced tumor cell control in the SKMel23 spheroid model

Monolayer cultures of melanoma cells are inappropriate to study the effects of PD-1 based chimeric receptors due to low expression levels of the respective ligand PD-L1. Increased PD-L1 expression on SKMel23 cells grown in spheroids, in contrast, seemed to open the possibility to evaluate effects of PD-1:28 and PD-1:BB in a more physiologic setting without the need of genetically engineering the melanoma cells. This was tested using the 3D spheroid assays as established above (6.4.1.3) and D115 CTLs expressing PD-1:28 or PD-1:BB in comparison to D115 CTLs without chimeric proteins and T58 CTLs.

Upon invasion into spheroids, D115 CTLs engineered to express PD-1:28 secreted more of the cytokines IL-2, IFN- γ , TNF- α and GM-CSF, although levels secreted by T58 CTLs were still higher. Expression of the PD-1:BB protein did not alter cytokine secretion of D115 CTLs (**Figure 25 A**). Measuring spheroid volumes as surrogate of tumor growth control revealed that both chimeric receptors enhanced D115 CTLs enabling them to reduce spheroid size over 3 d of co-incubation to extents similar as observed with the high avidity T58 CTLs (**Figure 25 B**). Spheroids that were invaded by D115 CTLs without chimeric proteins remained significantly larger than those seen with T58 CTLs, while the volume reduction between D115/Mock and D115/PD-1:28 or D115/PD-1:BB did not reach significance. This was due to observed high variability in the results of three independently conducted experiments with different lots of T cells (see appendix, 11.5, **Figure 28**). A stronger tumor control by CTLs expressing chimeric constructs or high avidity T58-TCR compared to D115/Mock CTLs was not detected reliably, especially in the two first experiments where initial spheroid sizes were below 0.02 mm³. Whether smaller spheroids display different surface expression levels of the crucial markers tyrosinase peptide-MHC complex or PD-L1 or whether a different tumor milieu conditioned an altered immunological response was not further analyzed, but these spheroid volume reduction results should be interpreted carefully. After 6 d, however, PD-1:28 as well as PD-1:BB proteins enabled D115 CTLs to dissolve all of the spheroids, similar to the T58/Mock CTLs, while around 33 % of the spheroids that were invaded by D115/Mock CTLs were still present (**Figure 25 C**). This attests enhancing effects of the chimeric proteins for D115 CTLs despite the variability in the volume reduction measurements seen on day 3 and 4.

The invaded distances into the SKMel23 spheroids were similar for all CTLs independently of the TCR or the chimeric proteins (**Figure 25 D**).

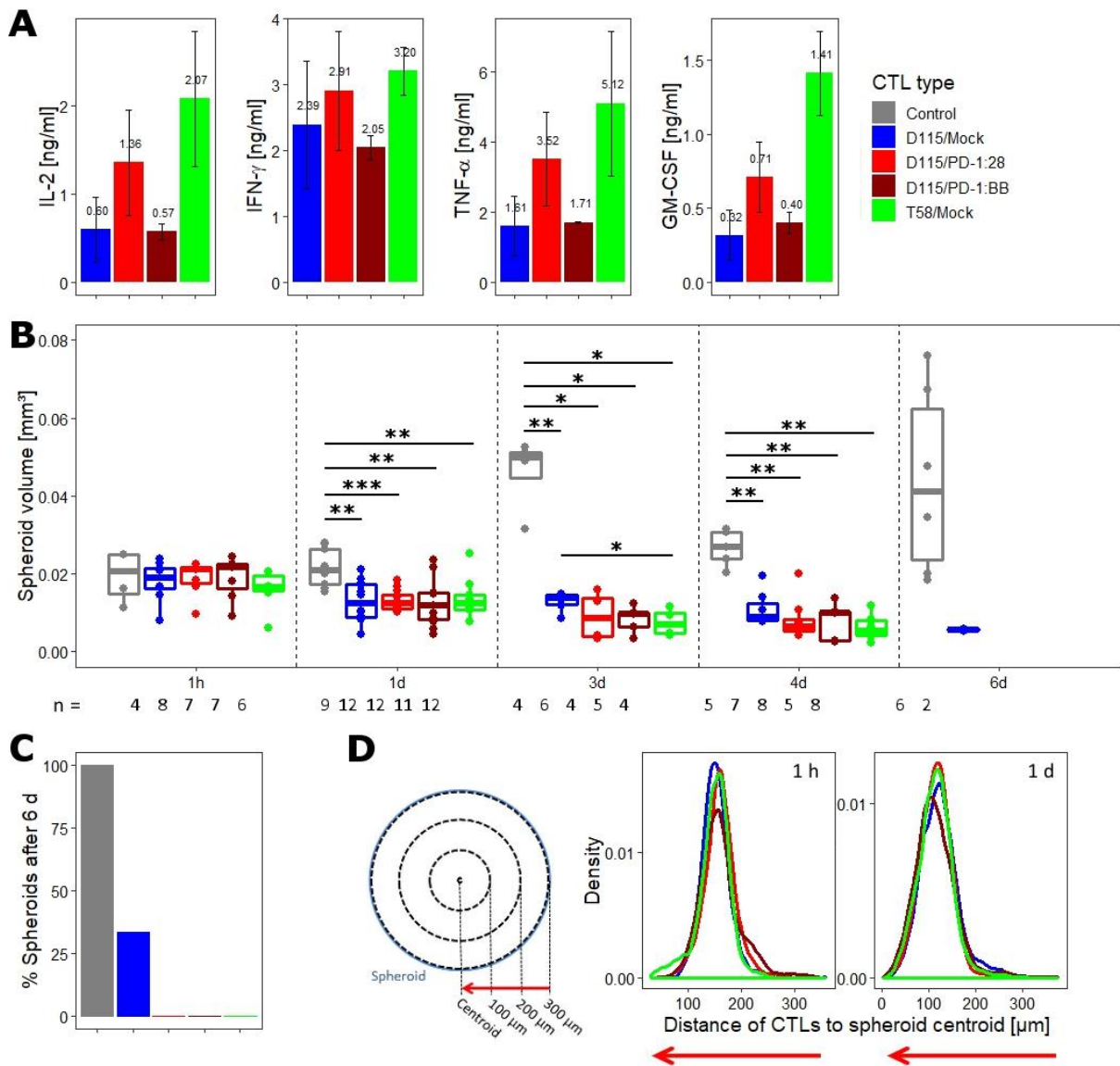


Figure 25 Invasion of chimeric co-stimulatory receptor-engineered CTLs into SKMel23 spheroids. D115/Mock, D115/PD-1:28, D115/PD-1:BB and T58/Mock CTL invaded spheroids were prepared as described in **Figure 19**. Three independent invasion experiments have been conducted with a total number of analyzed spheroids per group as indicated (n). Shown are: **(A)** Cytokine IL-2, IFN- γ , TNF- α and GM-CSF levels detected in hanging drop supernatants after 1 d of CTL invasion into SKMel23 spheroids (mean ng/ml of triplicates +/- SD); **(B)** spheroid volumes after indicated time points; each dot represents one spheroid and whisker-boxplots show their distribution, with boxes showing the quartiles and median values and whiskers the rest of the distribution without outliers; Mann-Whitney U test, * p-value < 0.05, ** p-value < 0.01, *** p-value < 0.001; **(C)** percentage of spheroids still intact after 6 d; and **(D)** density estimation of the distribution of invaded distances to the respective spheroid centroid after 1 h and 1 d of invasion.

7 Discussion

7.1 Spheroids and their capacity as *in vitro* tumor model

Due to their unique characteristics, tumor spheroids represent an essential tool in research and drug development. Comparison to monolayer cell cultures strongly demonstrates the potential impact of a 3D cellular environment on the phenotype of cells. The shape and interaction of cells in three dimensions as well as chemical gradients that develop with additional cell layers strongly influence gene expression, cell metabolism and proliferation (Bissell et al. 1982; Sutherland 1988). Although they still do not replicate a whole multifaceted tumor, spheroids are able to mimic certain physiological aspects of intervascular tumor microregions that monolayer cell cultures lack. The invasion assay developed here makes use of tumor spheroids as a dense 3D matrix, reflecting the cancer tissue that infiltrating cells have to navigate through *in vivo*. In addition, spheroids can mimic characteristics inherent to intervascular tumor microregions, such as oxygen and chemical gradients, and altered tumor cell phenotypes. The influence of these features on therapeutic cells could be investigated with regard to migration as well as anti-tumor action.

The size and age of a spheroid determines its characteristics. Sutherland et al. observed that undervascularized tumors with a size of 1 mm diameter show necrotic regions and induce angiogenesis (Sutherland 1988). The distance that oxygen can diffuse in solid tumor tissue was measured to be 100 – 200 μm (Olive et al. 1992). Accordingly, spheroids with a diameter up to 150 – 200 μm are reported to reflect gene expression profiles that are attributable to 3D cell-cell and cell-matrix interactions, but not hypoxic conditions. Gradients of oxygen, nutrients and catabolites are only seen in spheroids that are larger than 200 μm in diameter. A necrotic core is generally formed when the spheroids reaches a size of 500 – 600 μm , while those typically display a 100 – 300 μm rim of viable cells (Friedrich et al. 2007; Friedrich et al. 2009; Hirschhaeuser et al. 2010). The tumor spheroids used within this thesis generally measured between 300 – 500 μm in diameter. Therefore, they provided a 3D tumor matrix that could model oxygen as well as other chemical gradients. Although lacking a necrotic center, a heterogeneous division into highly proliferative and quiescent cells was likely present.

There are many techniques available for the characterization of various physiological stages of spheroids. These include measurements with microelectrodes to probe oxygen at different depths. Autoradiography has been used to track the distribution of radioactively labeled substrates, thus

localizing ATP, glucose or lactate metabolites. In addition, immunofluorescent and histological staining of spheroid sections allows the specific localization of proliferating or apoptotic cells (see **Figure 3**, Hirschhaeuser et al. 2010).

To identify an appropriate size and age for the spheroids used here, we adhered to consistent values about the development of a tumor-like milieu throughout the different microlayers of a spheroid reported in literature and refrained from directly analyzing them. However, the following findings did suggest a tumor reflecting milieu within the spheroids employed.

The first finding was a higher PD-L1 surface expression on SKMel23 melanoma cells grown in spheroids compared to cells grown in monolayer cultures. PD-L1 is generally overexpressed in tumors, whereas tumor cells grown *in vitro* often lack this expression (Flies and Chen 2007). It has been proposed that PD-L1 upregulation in tumor cells is mainly induced by IFN- γ , and occurs as a result of lymphocyte recruitment (Spranger et al. 2013). In addition, recent studies have identified a direct positive regulation of PD-L1 via the transcription factor hypoxia-inducible factor (HIF)-1 α (Noman et al. 2014). Since elevated PD-L1 levels on SKMel23 cells in spheroids were detected here in the absence of infiltrating T cells that produce IFN- γ , hypoxia is the likely factor leading to the upregulation seen in our setting. Low PD-L1 on SKMel23 cells grown in 2D cultures has been a confounding issue in our attempts to evaluate the PD-L1 dependent effects of the chimeric co-stimulatory proteins PD-1:28 and PD-1:BB (**Figure 23** and **Figure 24**). In addition to xenograft mouse models, where PD-L1 could be re-established on SKMel23 cells as well, the application of spheroid models now offers a viable *in vitro* alternative.

A second finding indicating tumor-like conditions in spheroids was the observation of increased expression of MHC I type HLA-A2 on the SKMel23 cells when grown as a spheroid, as compared to monolayer cultures. Like PD-L1 expression, MHC I expression has been linked to hypoxia. Hypoxia leads to upregulation of the endoplasmic reticulum oxidoreductase (ERO) 1- α , which in turn mediates oxidative folding of MHC I heavy chains in the ER. This results in enhanced surface presentation of MHC I, and subsequently enhanced recognition of tumor cells by CTLs (Kajiwara et al. 2016). The latter is the reason why tumor cells *in vivo* are subject to immune selection. Tumor cells that despite hypoxia downregulate MHC I are in general those that persist (Garrido et al. 2016). Altogether, elevated MHC I on tumor cells suggests that tumor-like conditions with regard to oxygen levels may be established in spheroids, but comprises an artificial phenotype itself by failing to reflect immune selection mechanisms. This should be considered with regard to the strength of target cell recognition by CTLs that might be unphysiologically high in *in vitro* spheroids.

Regarding the induction of the therapy gene HSV-TK under control of the CCL5/RANTES promoter in engineered MSCs the spheroid model conditions did not replicate the *in vivo* biology. Whereas studies

in a mouse model showed strong activation of the RANTES promoter in tumor settings (Niess et al. 2011), its induction was found to be reduced in spheroids over time.

A limitation for the use of spheroid based assays is the fact that not all tumor lines form those 3D cell aggregates. The renal cell carcinoma lines RCC26 and RCC53, for example, did not establish spheroids under the conditions employed here. To form compact spheroids, cells require expression of specific membrane adhesion proteins (Cui et al. 2017). A tumor cell line's capacity to grow in spheroid culture is likely linked to differing levels of these critical surface molecules. Also, the ability of other cell types to attach and invade tumor spheroids is probably associated with the tumor cell's specific surface molecule composition. For example, other than the cell lines HUH7 and LS174T tested here, the HT29 cell line did not seem to offer an appropriate substrate for MSC attachment (see appendix, 11.3, **Figure 26**). The analysis of HT29 cell membrane composition has revealed a lack of connexin Cx43 and reduced E-cadherin expression which could limit formation of gap or adherens junctions, curtailing the necessary physical and chemical cell-cell interactions for attachment (Nicholas et al. 2003; Han et al. 2013). Thus, the ability of cells to form spheroids, as well as their adhesive characteristics, could provide additional important information regarding a tumor's characteristics and behavior upon therapy.

Migration and metastasis linked proteins that tumor cells express when grown as spheroids are under investigation in assays that model the tumor spheroid's potential to invade a surrounding tissue or matrix (Hirschberg et al. 2006; Vinci et al. 2015). The ability of primary tumor single cell suspensions to form spheroids relies both on their proliferative and adhesive characteristics, and has been proposed as a general measure of cancer cell "stemness" (Ishiguro et al. 2017). Accordingly, the adhesion of therapeutic cells to tumor spheroids as measured here (see appendix, 11.3, **Figure 26**) may provide useful information with regards to cell - tumor interaction characteristics and clinical outcome. This may be especially relevant for the culture of primary tumor cells extracted from biopsies, or tumor resections, which have been shown to benefit from spheroid technologies. Because primary tumor cells grown in spheroid culture maintain important phenotypes seen *in vivo* (Witt Hamer et al. 2008), they are used for "personalized medicine" approaches to devise patient-specific therapy. Parameters tested in primary tumor cell spheroids allow a prediction of epithelial - mesenchymal transition (EMT) characteristics, invasive capacity or cancer stemness, and susceptibility to drug treatment (Lin et al. 2015; Ishiguro et al. 2017; Vlachogiannis et al. 2018). Defining the adhesive and invasive features of therapeutic cells on different tumor spheroids as well as their capacity to kill the tumor cells, as performed within the scope of this thesis, integrate well into such diagnostic assays.

7.2 Therapeutic mesenchymal stem cells – optimal pre-conditioning for effective tumor homing

The pre-conditioning that occurs during *ex vivo* expansion of therapeutic MSCs can influence the tumor homing behavior of these cells. Since spheroids can reflect conditions of intervascular tumor microregions, they were employed here as a potential platform to study conditions that impact the MSCs capacity of tumor infiltration before applying the cells *in vivo*. Since mechanisms driving tumor homing and infiltration are complex, it remains to be clarified if the effects seen here are stable and predictive of the behavior upon application to a patient and still retain a safe therapeutic cell product without side effects at non-tumor sites. MSC migration mechanisms as well as safety issues shall be discussed in the following.

7.2.1 Assays to analyze MSC recruitment to tumor sites

Therapeutic MSCs that are systemically applied via intravenous injection undergo a series of steps during their recruitment to tumor sites (Karp and Leng Teo 2009). These include de-acceleration and arrest on the endothelium, extravasation and migration towards the depth of a tumor. The alternative direct intratumoral injection is not possible for every tumor type and excludes the effective treatment of metastases. Moreover, it has been discussed that each of the steps involved in tumor homing can impact and prime MSCs for optimal differentiation in a therapeutic context (Bao et al. 2012). Thus, *in vitro* modelling of only one aspect of recruitment might not be able to completely reflect *in vivo* cell behavior.

A series of *in vitro* assays have been applied to investigate specific steps in the recruitment process. Smith et al. employed an array of analyses to study a broad spectrum of MSC recruitment characteristics. The authors used a microfluidic adherence assay to investigate the attachment of MSCs to an endothelial cell monolayer under physiologic flow. They then employed a modified Boyden chamber as a transendothelial migration assay to analyze the extravasation capacity of MSCs by means of their ability to cross an endothelial cell monolayer. And finally, chemotaxis was analyzed via monitoring cell migration along a chemotactic gradient within a channel of a microfluidic device, or from the upper to the lower chamber of a transwell plate. The authors reported that the pre-conditioning of MSCs with glioma-conditioned medium, fibronectin or laminin, enhanced their activity in all homing steps *in vitro*, and the general effects could eventually be validated *in vivo* (Smith et al. 2015). By comparison, the methods used here, namely migration in a collagen matrix and invasion into tumor spheroids, largely analyze processes downstream of MSC extravasation. However, both the migration assay performed using a 3D collagen matrix, and the tumor spheroid invasion assay provide an additional 3D matrix context, and model cell locomotion in a potentially

more physiological manner. The invasion assay into tumor spheroids developed here may represent the first *in vitro* assay reported that mimics MSC locomotion within the three dimensional tumor micromilieu.

Hypoxia was found to specifically induce chemokine IL-6 secretion in breast cancer cells. IL-6 has been shown to attract MSCs towards hypoxic tumor cells by inducing an enhanced migratory activity via cytoskeletal reorganization to actin stress fibers (Rattigan et al. 2010). As discussed above, a hypoxic inner core is probably present within the spheroids used here and should presumptively result in chemokine gradients. Invaded distances of MSCs along this gradient should thus be an appropriate measure to quantify the cells' potential for directional migratory activation within the tumor spheroid.

7.2.2 Biologic mechanisms underlying MSC recruitment to tumor sites

The individual steps in MSC homing are mediated by a series of molecules. Key proteins in this regard include chemokine receptors, of which the following have been described to be expressed on MSCs: CCR1, CCR2, CCR3, CCR4, CCR7, CCR8, CCR9, CCR10, CXCR1, CXCR2, CXCR3, CXCR4, CXCR5, and CXCR6 (Lüttichau et al. 2005; Bao et al. 2012). Chemokine receptors mediate the tissue-specific homing of diverse cell types, including stem cells and leukocytes, and may also play a role in the tissue distribution of tumor metastases (Kakinuma and Hwang 2006). The binding of chemokines to chemokine receptors can be redundant, or specific. The chemokine CXCL12 (SDF-1) / receptor CXCR4 axis represents a highly specific interaction and has been proposed to play a dominant role in MSC recruitment to tumors. CXCL12 binding to CXCR4 activates cells for adhesion and extravasation. This signal alters the affinity of MSC-expressed integrins for their respective adhesion molecules, for example VCAM-1, on endothelial cells, thus supporting arrest on the vasculature surface (Kakinuma and Hwang 2006). Moreover, it has been reported that CXCR4 also triggers downstream activation of Akt and MAP kinase pathways, and induces the expression of matrix metalloproteinase MMP-9 (Chinni et al. 2006). MMPs are essential in cellular extravasation and for their migration through tissue as they help degrade the extracellular matrix (ECM) proteins and disassemble focal adhesions, thus clearing the way for migrating cells.

Whereas the mechanisms controlling MSC recruitment towards a tumor site including endothelial rolling, arrest and extravasation, are thought to be similar to that seen during leukocyte recruitment, chemotactic migration through tissue appears to follow a different set of mechanisms (Bear and Haugh 2014). Both leukocytes and MSCs sense chemotactic gradients, which drive signaling and cytoskeletal responses. The mode of trafficking in 3D settings, though, differs with regard to speed and mechanism. Fast leukocytes twist through tissues using strongly polarized protrusions, called

pseudopods, and only marginally rely on anchor points on the ECM or other cells. Mesenchymal cells, by contrast, migrate slower and are less efficiently polarized. Their mode of locomotion is poorly understood, but is thought to be composed of a different set of mechanisms. Mesenchymal cells usually display multiple protrusions, called lamellipodia and filopodia, and show strong adhesion to the ECM. In leukocytes, the cytoskeleton is organized into a pushing uropod opposite to the cell front. In mesenchymal cells, the cytoskeleton forms contractile actin stress fibers anchored to focal adhesions all over the cell. Thus, they rather pull themselves forward, especially when they move in a so called haptotactic mode: MSCs translocate along immobilized ligands on the ECM to which their integrins bind and form focal adhesions as anchor points for contractile stress fibers (Rattigan et al. 2010, Bear and Haugh 2014).

Surface molecules such as chemokine receptors and integrins are involved both in the homing of MSCs from the peripheral circulation towards tumor sites, and in their migration along chemotactic gradients within the tumor tissue. Thus, effects that positively impact invasion into spheroids may similarly enhance the general efficiency of systemically injected MSC recruitment to tumor settings.

This was demonstrated in a parallel study of the effects of thyroid hormones on MSC recruitment that made use of the invasion assay developed within this thesis. Thyroid hormones act via cytoplasmic hormone receptors, but also via signaling through the $\alpha\beta3$ integrin. This signaling can be blocked by the competitive binding of tetraiodothyroacetic acid (tetrac) (Bergh et al. 2005). Exposing primary human MSCs to the thyroid hormones triiodo-l-thyronine (T3) and l-thyroxine (T4) was found to enhance their *in vitro* migration towards hepatocellular carcinoma cell HUH7-derived conditioned medium, and to specifically enhance their invasion into HUH7 spheroids (see appendix, 11.4, **Figure 27**). Importantly, this effect could be replicated in an *in vivo* setting that showed both enhanced MSC recruitment and tumor infiltration of adoptively applied MSCs in the context of hyperthyroid conditions. The $\alpha\beta3$ integrin-specific inhibitor tetrac could reverse those effects (published in Schmohl et al. 2015). As outlined above, integrins play a role in arrest of circulating cells on the endothelium and the hapto-/chemotactic migration of mesenchymal cells. This may help explain the positive effects of integrin stimulation with T3 and T4 thyroid hormones, on both the homing of MSCs and their invasion into *in vivo* and *in vitro* tumor tissue.

7.2.3 Pre-conditioning and growth conditions can enhance MSC homing and tumor infiltration

The efficiency of adoptively applied MSCs to migrate to damaged tissue can be enhanced (Becker and van Riet 2016). The general biology and biodistribution of MSCs after their systemic injection is poorly understood. Due to their relatively large size after *in vitro* expansion, MSCs become entrapped in lung and splenic microvessels within minutes after intravenous injection. They are cleared from the microvasculature within a few days, and subsequently home to liver and secondary lymphatics, and

at lower frequencies, to other organs such as skin, intestines, kidney and bone marrow (Karp and Leng Teo 2009, Leibacher and Henschler 2016). When compared to intravenous injection, intra-arterial injection was shown to significantly reduce the initial localization within the lung and enhance homing to peripheral sites. Importantly, the presence of inflammatory signals alters the biodistribution of MSCs towards sites of tissue injury or cancer. MSCs were shown to be cleared significantly faster from the circulation of mice bearing tumors, as compared to healthy mice. They were found to actively home to solid tumors and metastases (Xie et al. 2017). Still, also homing to pathophysiological sites is sought to be optimized.

As seen with the thyroid hormone enhanced integrin dependent effects, many homing related molecules are involved in several substeps. Thus, pre-conditioning related effects seen in tumor spheroid invasion may also positively impact previous recruitment processes.

The tumor spheroid invasion assay revealed an enhanced invasive activity of MSCs that were cultured for an increased number of passages, and when FCS was used for cell culture in the place of human serum components. Although a positive effect of autocrine signaling via cytokines secreted by MSCs in culture has been described (Boomsma and Geenen 2012), expanded growth *in vitro* is mostly reported to downregulate chemokine receptors and decrease homing behavior (Becker and van Riet 2016). The enhanced invasion potential identified here of MSCs between passage three and five may be due in part to the switch in culture medium from human serum to FCS conditions. Indeed, FCS culture was shown to enhance SDF-1 α secretion by MSCs and their migration *in vitro* (Goedecke et al. 2011). MSCs cultured in FCS containing medium also display an increase in focal adhesions and stress fibers, mediating a stronger interaction with the surrounding matrix (Fernandez-Rebollo et al. 2017). As detailed earlier, MSCs depend on these focal adhesions for locomotion.

However, the use of FCS in clinical applications is contraindicated. MSCs expanded in FCS may expose patients to the risk of zoonotic infections, for example transmissible spongiform encephalopathy (TSE) variants like bovine spongiform encephalopathy (BSE) or Creutzfeldt-Jakob disease (CJD) (Asher 1999). Thus, human serum components are required instead in the manufacturing processes of biological agents. But although human platelet lysate is thought to be a safer culture supplement than FCS, and MSCs show similar or even enhanced proliferation when it is used (Fekete et al. 2012, Fernandez-Rebollo et al. 2017), one or several components of the fetal serum may still represent a useful culture supplement to enhance MSC homing efficiency. The invasion assay, in line with other *in vitro* assays that evaluate homing mechanisms, provides a tool to screen systematically for those components to identify safe and effective pre-conditioning supplements during MSC expansion.

In conclusion, the invasion assay developed here can be used to measure effects of growth conditions and pre-conditioning treatments on the invasive behavior of MSCs. In this regard, it provides a new *in vitro* tool for testing parameters linked to the recruitment of MSCs to tumor sites. By mimicking an important step in recruitment, the invasion of MSCs into the depth of tumors, the spheroid invasion assay closes a gap. It provides a model of the target structure and general milieu. Although all steps in tumor homing are essential for a successful application of cellular therapy, the spheroid invasion assay is able to predict tumor infiltration and potential activation of engineered MSCs. Within the scope of this thesis, it was successfully included into the test pipeline of primary human MSCs isolated, expanded and engineered for anti-tumor therapy and revealed important effects of different manufacturing processes on their invasion potential.

7.3 Assessing CTL activity *in vitro*

The design and application of therapeutic T cells represents a balancing act between efficiency and safety. Naturally occurring T cells with tumor antigen recognizing T cell receptors are often too weak to eliminate a malignancy. Issues that are addressed when considering CTL-based immune therapy of cancer include the low avidity of endogenous anti-tumor T cell receptors, a lack of co-stimulation, or an active inhibition of T cells, due either to a hostile tumor milieu characterized by high levels of lactic acid, or the expression of inhibitory molecules on the tumor cells (Hadrup et al. 2013, Vinay et al. 2015). Each of these issues can contribute to the phenomenon of T cell exhaustion often seen in tumor settings leading to a shutdown of their cytolytic activity (Pauken and Wherry 2015, Roufas et al. 2018). Although transgenic high avidity TCRs or CARs can improve a CTL response (Wilde et al. 2009), they may still not allow persistent anti-tumor activity *in vivo* (Janicki et al. 2008). Moreover, they may increase the risk of potential side effects. Unphysiologically high T cell avidity has been shown to critically enhance CTL action against healthy cells expressing tumor associated antigens at low levels (on-target off-tissue) (Johnson et al. 2009). In addition, artificially modified TCRs have a high risk to generate off-target off-tissue activity, as was observed with a high avidity TCR against melanoma associated antigen MAGE-A3 that attacked cardiomyocytes with fatal consequences (Linette et al. 2013). The use of standard CTL assays and mouse models failed to detect important cross-reactivity of the respective TCR directed against the human titin antigen. Cameron et al. described a method to predict possible target peptides by identifying the amino acids essential for TCR binding and using an *in silico* approach to search for respective homologues among endogenous peptides (Cameron et al. 2013). However, this requires an elaborate process and altering a TCR binding domain remains risky. By contrast, the use of chimeric co-stimulatory receptor designs may offer a safer approach to enhance CTL activity that turns the inhibition normally mediated by PD-1 via PD-L1 expressed on many tumor cells, into stimulatory signals (Prosser et al. 2012; Ankri et al. 2013). This approach may allow functional enhancement and application of naturally selected, thus safer, intermediate or low avidity TCRs heterologously expressed on CTLs. As observed here, low avidity D115-TCR CTLs with anti-melanoma activity displayed a lower cytotoxicity against SKMel23 spheroids, but became almost as effective as the high avidity T58-TCR CTLs when the chimeric receptors PD-1:28 or PD-1:BB designed in our laboratory were co-expressed. The application of these chimeric co-stimulatory receptors brings naturally occurring TILs with endogenous anti-tumor TCRs back into play for adoptive T cell therapy, as well as a large library of known low avidity TCRs.

Current standard CTL *in vitro* assays are often insufficient in their prediction of effective *in vivo* CTL responses. For example, the cross-reactive anti-MAGE-A3 CTLs described above were not found to

attack cardiac-derived cells *in vitro*, due to the downregulated titin expression that occurred in 2D culture. A physiologic titin expression, and a resulting anti-cardiomyocyte CTL response, could only be established in special cultures of induced pluripotent stem cell-derived cardiomyocytes (Cameron et al. 2013). Culture conditions that better reflect physiological phenotypes are therefore needed to predict the sensitive crosstalk of immunological processes. In the case of the chimeric co-stimulatory constructs evaluated here, analysis of effects that depended on PD-L1 expression benefitted from the increased PD-L1 expression on SKMel23 melanoma cells seen when grown as spheroids. This is an additional example of the potential benefit of using spheroid cultures in the context of physiological assay systems.

The study of immune cell and tumor cell biology using 3D spheroids was found to have significant advantages as compared to classical 2D immune assays. Sutherland et al. were the first to study immune cell interactions with tumor cell spheroids, and suggested beneficial insights with regards to immune cell – tumor infiltration and interaction (Sutherland et al. 1977). As discussed earlier, some of the tumor characteristics that spheroid based assays model include low oxygen levels and lactic acid accumulation. Hypoxia can potentially alter the surface expression of target or inhibitory molecules as described here. Elevated lactate levels in tumor spheroids allow the investigation of a potential inhibition of immune cells via this pathophysiological factor (Gottfried et al. 2006). In addition, spheroid invasion assays can better reflect aspects regarding immune cell distribution, ratio to target cells, and general geometrical interactions of effector and target cells than those seen in 2D cultures. How these spatial characteristics can influence CTL efficiency, and what this implies for *in vitro* assay systems will be discussed in the following sections.

Since its implementation in 1961, the chromium release assay has become the *in vitro* gold standard to determine specific cell lysis by immune system components (Goodman 1961; Brunner et al. 1968). In this assay, target cells are first loaded with radioactive ^{51}Cr . Upon cell lysis, ^{51}Cr is released and detectable in the culture supernatant. This is then used to determine the specific quantifiable cytotoxicity by CTLs *in vitro*. Although it has been thought to be a reliable, quick and relatively precise assay, the chromium release assay can be seen as limited by the somewhat artificial conditions needed. Due to cytotoxicity seen with ^{51}Cr itself, and the subsequent spontaneous lysis that occurs, it allows only relatively short incubation times, with a typical endpoint applied after 4 h. Short duration studies require the use of large numbers of T cells and high effector to target cell ratios to detect specific effects. Typical E:T ratios can reach levels up to 50:1. Alternative assays have been developed for real-time investigation of target cell killing, that run over longer time periods, and at lower E:T ratios (Noto et al. 2013; Peper et al. 2014). Still, these approaches generally rely on artificial 2D cell distributions. The same issues apply when using the cytokine secretion assays that are also broadly

applied to measure T cell response. These assays are based on the detection of cytokines like IFN- γ that are produced by activated T cells in 2D co-cultures. These studies are usually performed at lower E:T ratios of about 2:1 or 1:1, but cellular interactions also occur in a 2D environment.

One goal of this thesis was to determine if the tumor spheroid invasion assay developed here could be also used to better assess different CTL functions relevant for the evaluation of their efficiency. These include their general mobility or migration, cytokine production and target cytotoxicity, all studied in a more physiologic 3D tumor context. In the invasion assay established here, after 24 h co-incubation, approximately 1000 - 1500 CTLs could be detected per spheroid. Spheroids grew from an initial approximately 800 cells per hanging drop, to aggregates composed of about 6000 cells. This resulted in an E:T ratio of approximately 1:6. However, exact CTL numbers were not determinable at time points after three days due to the loss of CMFDA CellTracker signal. This dye is generally stable, and based on the manufacturer, can be detectable for longer than 72 h, and for up to three to six generations. The rapid decrease in signal strength observed here, as well as the increase in CTL numbers from about 300 CTLs/spheroid at 1 h to more than 1000 CTLs/spheroid at 24 h of invasion, suggests a high proliferation rate of CTLs within target spheroids. Kawai et al. tracked CTL proliferation in tumor spheroids over time. They observed strong CTL proliferation, and reported effective spheroid destruction after a few days when E:T ratios had reached levels $\geq 4:1$ (Kawai et al. 2001).

In any case, there are suggestions that rather than the final E:T ratio, the overall T cell density is more crucial for an effective immune response against cancer (Budhu et al. 2010). Given that approximately 1000 CTLs were detected in the tumor spheroids of roughly 0.02 mm³ volume, this would correlate with a concentration of 5×10^7 CTLs/ml. This value is in concordance with the general concentration of 10^7 CTLs/ml experimentally found to be necessary for successful melanoma cell eradication. Budhu et al. suggested that a constant presence of mouse OT-1 CTLs at these concentrations led to elimination of 100 % of mouse melanoma B16 cells in a 3D *in vitro* assay using collagen gel-based culture systems, that was independent of the E:T ratio. *In vivo*, however, the critical T-cell concentration was found to be about 10-fold higher. The authors suggest that this disparity was due to the presence of immune evasion mechanisms seen in solid tumors. Accordingly, the concentrations of human CTLs necessary to eradicate tumor spheroids as observed here might not be sufficient to eliminate tumor cells completely *in vivo*. In addition, the observed upregulation of MHC I HLA-A2 on SKMel23 spheroids can probably account for an unphysiologically high T cell response. In fact, *in vivo* MHC I is often downregulated on tumor cells due to immune selection (Garrido et al. 2016).

Complete tumor spheroid elimination at E:T ratios below 1 suggests the ability of CTLs for serial killing. A single CTL was found to be able to kill multiple targets, not only sequentially, but even simultaneously (Wiedemann et al. 2006). While cytokine production requires constant and strong

antigen stimulation, lytic granule delivery occurs at lower thresholds, and is delivered towards all targets a CTL is in contact with. This underscores the importance of the geometrical distribution of target cells around a CTL. Within spheroids, the kill mode and rate of CTLs are certainly much better reflected with regards to tumor biology *in vivo* than that seen in 2D assay conditions where T cells need to cross a plastic surface to migrate from cell to cell. Gadhamsetty et al. mathematically modelled T cell-target cell interactions as a function of their spatial environment, comparing 2D and 3D settings. They reported striking differences. In a 3D environment the maximal killing rate a CTL can exploit was achieved at lower CTL numbers than in 2D, because a given CTL can be simultaneously in contact with a higher number of potential targets. In addition, in a 3D environment the CTL – target cell contact stability was decreased, which was attributed to the pushing and pulling environment of migrating neighbor cells (Gadhamsetty et al. 2016).

This introduces an additional parameter concerning CTL-tumor cell interactions that the invasion assay can provide, and that is the effect of cell-to-cell migration. No hindrance of CTL infiltration into the depth of an experimental tumor spheroid was detected with high avidity TCRs. An early hypothesis proposed in the present study was that CTL binding to a target cell with high avidity would potentially prevent the cell from migrating deeper into the spheroid due to their constant triggering. We were able to show here that both D115- and T58-TCRs allowed CTLs to infiltrate through the entire spheroid within 24 h. Lymphocyte migration at a velocity of about 10 $\mu\text{m}/\text{min}$ is 10-fold faster than that seen with mesenchymal migration which occurs at less than 1 $\mu\text{m}/\text{min}$ (Bear and Haugh 2014). To determine if the incubation time of 24 h was too long to detect if one CTL type reached the spheroid core more rapidly, a shorter time frame was studied. An additional endpoint with spheroid fixation at 1 h after co-incubation and washing showed no difference between the depths invaded of high and low avidity CTLs. In addition, the measurement of live cell migration into spheroids by real-time imaging was attempted. Unfortunately, due to technical issues related to the confocal microscopy platform used, the sample numbers assessed here were rather small, with a maximum of seven spheroids tested per condition analyzed. However, the preliminary results suggested that CTL migration velocities rather depend on local concentrations of the CTLs, than on their TCR avidity (data not shown).

The spheroid invasion assay was used here to model the migration of engineered human CTLs within an experimental 3D tumor microenvironment. As discussed, migration was not found to be impaired by high avidity TCRs in a setting where a CTL is surrounded by potential targets. Mechanisms of cell-to-cell migration could be explained in part by Gadhamsetty et al.'s mathematical model that showed a frequent disruption of contacts in a 3D environment simply by physical forces. According to the *in vitro* data shown here, tumor infiltration was dependent on specific target recognition, but

independent of TCR avidity. Instead, the local CTL density seems to impact effective T cell activation and influences both migratory and cytotoxic efficiency. This is in concert with the critical T cell concentration concept reported by Budhu et al. and Kawai et al. who suggested that tumor spheroid elimination only occurred following considerable CTL proliferation (Budhu et al. 2010; Kawai et al. 2001). 3D assay systems such as the spheroid invasion assay implemented here, can provide better insight into these mechanisms. For effective tumor therapy, CTLs have to be generated with optimal responsive behavior. This not only includes high cytotoxicity at a single target cell level, but also an understanding of optimal behavior regarding simultaneous and serial killing, as well as accumulation, proliferation and persistence at the tumor site. In this regard, spheroid assays provide an important *in vitro* tool to analyze this behavior under physiological conditions with regard to cellular phenotypes and spatial distribution.

8 Conclusion

Tumor spheroids are currently used in drug development and as an *ex vivo* tool to predict cancer therapy outcome. The choice of therapeutic treatments ranges today from conventional surgical treatment, to radio- and chemotherapy up to sophisticated approaches that target diverse aspects of tumor biology. These include oncolytic viruses, cancer vaccines and therapeutic antibodies, and also the use of adoptively applied cellular approaches. Among these, mesenchymal stem cells are under development as tumor homing vehicles for the delivery of pro-apoptotic agents. Furthermore, the transfer of cytotoxic T cells carries the potential for both precise targeting and efficient tumor elimination and has been successfully employed in clinical applications. The tumor spheroid based invasion assay developed here offers a useful tool to further understand and analyze the migration and functional activity of these therapeutic cells and to select those with the best therapeutic behavior. Tumor spheroids used as an invasion matrix modeled physiologic tumor conditions and allowed the study of migratory and effector behavior, providing insight into therapy cell mode of action within the intervascular tumor niche. SPIM imaging was successfully used for the *in situ* analysis of the 3D distribution of therapeutic cells within the entire spheroid. The largely automatic image analysis developed here enabled a semi-high-throughput screening of different conditions, relevant for determining aspects of anti-tumor efficiency. The invasion assay appeared convenient to test the impact of pre-conditioning on the MSC tumor invasion potential, and could be applied to optimize a clinical product. With regards to the study of adoptive T cell therapy, the spheroid invasion assay was successfully used to model a complex tumor – immune cell interaction, including CTL infiltration and control of tumor growth. The results also suggest that the invasion assay could be employed in the context of a “personalized medicine” platform to help assess the potential sensitivity of a patient’s tumor to cell based therapies.

It is of note here that tumor spheroids do not reflect the complexity of a whole organism. The invasion assay therefore is not capable of modeling mechanisms that occur prior to therapeutic cell tumor infiltration, impacting clinical outcome as well. The investigation of activation, recruitment towards tumor sites and, importantly, off-target effects still often requires *in vivo* experiments. However, in the attempt to break down all essential steps involved in these processes to *in vitro* models (Smith et al. 2015), the invasion assay certainly has its *raison d’être*.

9 Abbreviations

2D	2-dimensional
2PM	Two-photon microscopy
3D	3-dimensional
⁵¹ Cr	⁵¹ chromium isotope
7-AAD	7-Aminoactinomycin
A594	Alexa Fluor 594
AA	Amino acid
AM	Acetoxymethyl
APC	Allophycocyanin
APC	Antigen presenting cell
ATP	Adenosine triphosphate
ATT	Adoptive T cell therapy
BSA	Bovine serum albumin
BSE	Bovine spongiform encephalopathy
Ca ²⁺	Calcium/calcium ions
CAF	Cancer associated fibroblast
CAR	Chimeric antigen receptor
CCD	Charge-coupled device
CCL5	Chemokine (C-C motif) ligand
CCR	Chemokine (C-C motif) receptor
CD	Cluster of differentiation
CJD	Creutzfeldt-Jakob disease
CLSM	Confocal laser scanning microscopy
CMFDA	5-Chloromethylfluorescein diacetate
CO ₂	Carbon dioxide
CoM	Centre of mass
CTL	Cytotoxic T lymphocyte
CTLA-4	Cytolytic T lymphocyte associated protein 4
CXCL	Chemokine (C-X-C motif) ligand
CXCR	Chemokine (C-X-C motif) receptor
DAPI	4',6-Diamidino-2'-phenylindole dihydrochloride
DC	Dendritic cell
DIC	Differential interference contrast
DMEM	Dulbecco's modified eagle medium
DMSO	Dimethyl sulfoxide
DNA	Deoxyribonucleic acid
DPBS	Dulbecco's phosphate buffered salt solution
e.g.	for example (lat. <i>exempli gratia</i>)
E:T ratio	Effector to target ratio
ECD	Extracellular domain
ECM	Extracellular matrix
EDTA	Ethylenediaminetetraacetic acid

EFS	Embryonal Fyn-Associated Substrate
ELISA	Enzyme-linked-immunosorbent assay
ER	Endoplasmatic reticulum
ERO 1- α	Endoplasmatic reticulum oxidoreductase 1- α
et al.	And others (lat. et alii)
etc.	And other similar things (lat. et cetera)
FACS	Fluorescence-activated cell sorting
FCS	Fetal calf serum
FDA	Food and Drug Administration
FFP	Fresh frozen plasma
FI	Fluorescence intensity
FITC	Fluorescein isothiocyanate
FMI	Forward migration index
GCV	Ganciclovir
GM-CSF	Granulocyte-macrophage colony-stimulating factor
GMP	Good manufacturing practice
H ₂ O	Dihydrogen monoxide, water
HA	Human influenza hemagglutinin
hBMSC	Human bone marrow derived mesenchymal stem cell
HEPES	4-(2-Hydroxyethyl)-1-piperazineethanesulfonic acid
HER2	Human epidermal growth factor receptor 2
HLA	Human leukocyte antigen
HSC	Hematopoietic stem cell
HSV-TK	Herpes simplex virus thymidine kinase
ICD	Intracellular domain
IFN	Interferon
IgG	Immunglobulin G
IL	Interleukin
ISCT	International Society of Cell Therapy
KCl	Potassium chloride
KH ₂ PO ₄	Monopotassium phosphate
KHCO ₃	Potassium bicarbonate
LMU	Ludwig-Maximilians-University
LSFM	Light sheet fluorescence microscopy
MAGE-A3	Melanoma associated antigen A3
MAP kinase	Mitogen-activated protein kinase
MESV	Murine embryonic stem cell virus
MHC	Major histocompatibility complex
MMP	Matrix metalloproteinase
MPSV-LTR	Murine myeloproliferative sarcoma virus - long terminal repeats
MSC	Mesenchymal stem cell
n	number
NA	Numerical aperture
Na ₂ CO ₃	Sodium carbonate
Na ₂ -EDTA	EDTA disodium salt
Na ₂ HPO ₄	Disodium phosphate

NaCl	Sodium chloride
NaHCO ₃	Sodium bicarbonate
NaN ₃	Sodium azide
NaOH	Sodium hydroxide
NH ₄ Cl	Ammonium chloride
NIH	National Institutes of Health
NK cell	Natural killer cell
ns	Not significant
p/p-value	Probability value
PBMC	Peripheral blood mononuclear cell
PBS	Phosphate buffered salt solution
PBST	Phosphate buffered saline with Tween-20
PD-1	Programmed cell death protein-1
PD-L	PD-1 ligand
PE	Phycoerythrin
PFA	Paraformaldehyde
PMT	Photomultiplier tube
polyHEMA	Poly (2-hydroxyethyl methacrylate)
RAM	Random access memory
RANTES	Regulated on activation, normal T cell expressed and secreted protein
rIL-2	Recombinant IL-2
RNA	Ribonucleic acid
RPMI	Roswell Park Memorial Institute
S2	Safety level 2
SD	Standard deviation
SDCM	Spinning disc confocal microscopy
SDF-1	Stromal cell-derived factor 1
SEM	Standard error of the mean
SPIM	Selective plane illumination microscopy
t	Time
T3	3,3',5-Triiodo-L-thyronine
T4	L-thyroxine
TAA	Tumor associated antigen
TCR	T cell receptor
Tetrac	Tetraiodothyroacetic acid
Th1	Type 1 T helper cell
Th2	Type 2 T helper cell
TIL	Tumor infiltrating lymphocyte
TK	Thrombozytenkonzentrat (Platelet concentrate)
TMD	Transmembrane domain
TNF- α	Tumor necrosis factor α
TRAIL	Tumor necrosis factor-related apoptosis induced ligand
TSE	Transmittable spongiform encephalopathy
Tyr	Tyrosinase
V(D)J	Variable, diversity and joining segments
VCAM-1	Vascular cell adhesion molecule 1

VLA-4	Very Late Antigen 4
WHO	World Health Organisation

Units

°	Degree
°C	Degree Celsius
μCi	Microcurie
μg	Microgram
μl	Microliter
μm	Micrometer
μM	Micromolar
Bp	Base pair
cm ²	Square centimeter
d	Day
g	Gram
GB	Gigabyte
GHz	Gigahertz
h	Hour
M	Molar
min	Minute
ml	Milliliter
mm	Millimeter
mM	Millimolar
mm ³	Cubic millimeter
ms	Millisecond
mW	Milliwatt
MW	Megawatt
ng	Nanogram
nm	Nanometer
s	Second
U/ml	Units per milliliter

10 References

Ankri, Chen; Shamalov, Katerina; Horovitz-Fried, Miryam; Mauer, Shmuel; Cohen, Cyrille J. (2013): Human T cells engineered to express a programmed death 1/28 costimulatory retargeting molecule display enhanced antitumor activity. In *Journal of immunology (Baltimore, Md. : 1950)* 191 (8), pp. 4121–4129. DOI: 10.4049/jimmunol.1203085.

Asher, D. M. (1999): Bovine sera used in the manufacture of biologicals. Current concerns and policies of the U.S. Food and Drug Administration regarding the transmissible spongiform encephalopathies. In *Developments in biological standardization* 99, pp. 41–44.

Bai, Lianhua; Lennon, Donald P.; Eaton, Valerie; Maier, Kari; Caplan, Arnold I.; Miller, Stephen D.; Miller, Robert H. (2009): Human bone marrow-derived mesenchymal stem cells induce Th2-polarized immune response and promote endogenous repair in animal models of multiple sclerosis. In *Glia* 57 (11), pp. 1192–1203. DOI: 10.1002/glia.20841.

Bao, Qi; Zhao, Yue; Niess, Hanno; Conrad, Claudius; Schwarz, Bettina; Jauch, Karl-Walter et al. (2012): Mesenchymal stem cell-based tumor-targeted gene therapy in gastrointestinal cancer. In *Stem cells and development* 21 (13), pp. 2355–2363. DOI: 10.1089/scd.2012.0060.

Barry, Frank P.; Murphy, J. Mary (2004): Mesenchymal stem cells. Clinical applications and biological characterization. In *The international journal of biochemistry & cell biology* 36 (4), pp. 568–584. DOI: 10.1016/j.biocel.2003.11.001.

Bear, James E.; Haugh, Jason M. (2014): Directed migration of mesenchymal cells. Where signaling and the cytoskeleton meet. In *Current opinion in cell biology* 30, pp. 74–82. DOI: 10.1016/j.ceb.2014.06.005.

Becker, Ann de; van Riet, Ivan (2016): Homing and migration of mesenchymal stromal cells. How to improve the efficacy of cell therapy? In *World journal of stem cells* 8 (3), pp. 73–87. DOI: 10.4252/wjsc.v8.i3.73.

Bergh, Joel J.; Lin, Hung-Yun; Lansing, Lawrence; Mohamed, Seema N.; Davis, Faith B.; Mousa, Shaker; Davis, Paul J. (2005): Integrin alphaVbeta3 contains a cell surface receptor site for thyroid hormone that is linked to activation of mitogen-activated protein kinase and induction of angiogenesis. In *Endocrinology* 146 (7), pp. 2864–2871. DOI: 10.1210/en.2005-0102.

Bissell, M. J.; Hall, H. G.; Parry, G. (1982): How does the extracellular matrix direct gene expression? In *Journal of theoretical biology* 99 (1), pp. 31–68.

Bolte, S.; Cordelières, F. P. (2006): A guided tour into subcellular colocalization analysis in light microscopy. In *Journal of microscopy* 224 (Pt 3), pp. 213–232. DOI: 10.1111/j.1365-2818.2006.01706.x.

- Boomsma, Robert A.; Geenen, David L. (2012): Mesenchymal stem cells secrete multiple cytokines that promote angiogenesis and have contrasting effects on chemotaxis and apoptosis. In *PloS one* 7 (4), e35685. DOI: 10.1371/journal.pone.0035685.
- Brunner, K. T.; Mauel, J.; Cerottini, J. C.; Chapuis, B. (1968): Quantitative assay of the lytic action of immune lymphoid cells on 51-Cr-labelled allogeneic target cells in vitro; inhibition by isoantibody and by drugs. In *Immunology* 14 (2), pp. 181–196.
- Budhu, Sadna; Loike, John D.; Pandolfi, Ashley; Han, Soo; Catalano, Geoffrey; Constantinescu, Andrei et al. (2010): CD8⁺ T cell concentration determines their efficiency in killing cognate antigen-expressing syngeneic mammalian cells in vitro and in mouse tissues. In *The Journal of experimental medicine* 207 (1), pp. 223–235. DOI: 10.1084/jem.20091279.
- Cameron, Brian J.; Gerry, Andrew B.; Dukes, Joseph; Harper, Jane V.; Kannan, Vivekanandan; Bianchi, Frayne C. et al. (2013): Identification of a Titin-derived HLA-A1-presented peptide as a cross-reactive target for engineered MAGE A3-directed T cells. In *Science translational medicine* 5 (197), 197ra103. DOI: 10.1126/scitranslmed.3006034.
- Caplan, A. I. (1991): Mesenchymal stem cells. In *Journal of orthopaedic research : official publication of the Orthopaedic Research Society* 9 (5), pp. 641–650. DOI: 10.1002/jor.1100090504.
- Cartellieri, Marc; Bachmann, Michael; Feldmann, Anja; Bippes, Claudia; Stamova, Slava; Wehner, Rebekka et al. (2010): Chimeric antigen receptor-engineered T cells for immunotherapy of cancer. In *Journal of biomedicine & biotechnology* 2010, p. 956304. DOI: 10.1155/2010/956304.
- Chamberlain, Giselle; Fox, James; Ashton, Brian; Middleton, Jim (2007): Concise Review. Mesenchymal Stem Cells: Their Phenotype, Differentiation Capacity, Immunological Features, and Potential for Homing. In *Stem cells (Dayton, Ohio)* 25 (11), pp. 2739–2749. DOI: 10.1634/stemcells.2007-0197.
- Chen, Lieping; Flies, Dallas B. (2013): Molecular mechanisms of T cell co-stimulation and co-inhibition. In *Nature reviews. Immunology* 13 (4), pp. 227–242. DOI: 10.1038/nri3405.
- Chen, Q.; Shou, P.; Zheng, C.; Jiang, M.; Cao, G.; Yang, Q. et al. (2016): Fate decision of mesenchymal stem cells. Adipocytes or osteoblasts? In *Cell death and differentiation* 23 (7), pp. 1128–1139. DOI: 10.1038/cdd.2015.168.
- Chinni, Sreenivasa R.; Sivalogan, Sivasakthy; Dong, Zhong; Filho, J. Carlos Trindade; Deng, Xiyun; Bonfil, R. Daniel; Cher, Michael L. (2006): CXCL12/CXCR4 signaling activates Akt-1 and MMP-9 expression in prostate cancer cells. The role of bone microenvironment-associated CXCL12. In *The Prostate* 66 (1), pp. 32–48. DOI: 10.1002/pros.20318.
- Chivu, Mihaela; Dima, Simona O.; Stancu, Cosmin I.; Dobrea, Camelia; Uscatescu, Valentina; Necula, Laura G. et al. (2009): In vitro hepatic differentiation of human bone marrow mesenchymal stem cells under differential

exposure to liver-specific factors. In *Translational research : the journal of laboratory and clinical medicine* 154 (3), pp. 122–132. DOI: 10.1016/j.trsl.2009.05.007.

Coleman, M. L.; Sahai, E. A.; Yeo, M.; Bosch, M.; Dewar, A.; Olson, M. F. (2001): Membrane blebbing during apoptosis results from caspase-mediated activation of ROCK I. In *Nature cell biology* 3 (4), pp. 339–345. DOI: 10.1038/35070009.

Colter, D. C.; Class, R.; DiGirolamo, C. M.; Prockop, D. J. (2000): Rapid expansion of recycling stem cells in cultures of plastic-adherent cells from human bone marrow. In *Proceedings of the National Academy of Sciences of the United States of America* 97 (7), pp. 3213–3218. DOI: 10.1073/pnas.070034097.

Crisan, Mihaela; Yap, Solomon; Casteilla, Louis; Chen, Chien-Wen; Corselli, Mirko; Park, Tea Soon et al. (2008): A perivascular origin for mesenchymal stem cells in multiple human organs. In *Cell stem cell* 3 (3), pp. 301–313. DOI: 10.1016/j.stem.2008.07.003.

Cui, X.; Hartanto, Y.; Zhang, H. (2017): Advances in multicellular spheroids formation. In *Journal of the Royal Society, Interface* 14 (127). DOI: 10.1098/rsif.2016.0877.

Djouad, Farida; Plence, Pascale; Bony, Claire; Tropel, Philippe; Apparailly, Florence; Sany, Jacques et al. (2003): Immunosuppressive effect of mesenchymal stem cells favors tumor growth in allogeneic animals. In *Blood* 102 (10), pp. 3837–3844. DOI: 10.1182/blood-2003-04-1193.

Dominici, M.; Le Blanc, K.; Mueller, I.; Slaper-Cortenbach, I.; Marini, Fc; Krause, Ds et al. (2006): Minimal criteria for defining multipotent mesenchymal stromal cells. The International Society for Cellular Therapy position statement. In *Cytotherapy* 8 (4), pp. 315–317. DOI: 10.1080/14653240600855905.

Edelstein, Arthur; Amodaj, Nenad; Hoover, Karl; Vale, Ron; Stuurman, Nico (2010): Computer control of microscopes using μ Manager. In *Current protocols in molecular biology* Chapter 14, Unit14.20. DOI: 10.1002/0471142727.mb1420s92.

Einem, Jobst C. von; Peter, Sylvia; Günther, Christine; Volk, Hans-Dieter; Grütz, Gerald; Salat, Christoph et al. (2017): Treatment of advanced gastrointestinal cancer with genetically modified autologous mesenchymal stem cells - TREAT-ME-1 - a phase I, first in human, first in class trial. In *Oncotarget* 8 (46), pp. 80156–80166. DOI: 10.18632/oncotarget.20964.

Fan, Hongye; Zhao, Guangfeng; Liu, Liu; Liu, Fei; Gong, Wei; Liu, Xianqin et al. (2012): Pre-treatment with IL-1 β enhances the efficacy of MSC transplantation in DSS-induced colitis. In *Cellular & molecular immunology* 9 (6), pp. 473–481. DOI: 10.1038/cmi.2012.40.

Feder-Mengus, C.; Ghosh, S.; Weber, W. P.; Wyler, S.; Zajac, P.; Terracciano, L. et al. (2007): Multiple mechanisms underlie defective recognition of melanoma cells cultured in three-dimensional architectures by antigen-specific cytotoxic T lymphocytes. In *British journal of cancer* 96 (7), pp. 1072–1082. DOI: 10.1038/sj.bjc.6603664.

- Fekete, Natalie; Gadelorge, Mélanie; Fürst, Daniel; Maurer, Caroline; Dausend, Julia; Fleury-Cappelleso, Sandrine et al. (2012): Platelet lysate from whole blood-derived pooled platelet concentrates and apheresis-derived platelet concentrates for the isolation and expansion of human bone marrow mesenchymal stromal cells. Production process, content and identification of active components. In *Cytotherapy* 14 (5), pp. 540–554. DOI: 10.3109/14653249.2012.655420.
- Fernandez-Rebollo, Eduardo; Mentrup, Birgit; Ebert, Regina; Franzen, Julia; Abagnale, Giulio; Sieben, Torsten et al. (2017): Human Platelet Lysate versus Fetal Calf Serum. These Supplements Do Not Select for Different Mesenchymal Stromal Cells. In *Scientific reports* 7 (1), p. 5132. DOI: 10.1038/s41598-017-05207-1.
- Fischer, Robert S.; Wu, Yicong; Kanchanawong, Pakorn; Shroff, Hari; Waterman, Clare M. (2011): Microscopy in 3D. A biologist's toolbox. In *Trends in cell biology* 21 (12), pp. 682–691. DOI: 10.1016/j.tcb.2011.09.008.
- Flier, J. S.; Underhill, L. H.; Dvorak, H. F. (1986): Tumors: Wounds That Do Not Heal. In *N Engl J Med* (315 (26)), pp. 1650–1659.
- Flies, Dallas B.; Chen, Lieping (2007): The new B7s. Playing a pivotal role in tumor immunity. In *Journal of immunotherapy (Hagerstown, Md. : 1997)* 30 (3), pp. 251–260. DOI: 10.1097/CJI.0b013e31802e085a.
- Freeman, G. J.; Long, A. J.; Iwai, Y.; Bourque, K.; Chernova, T.; Nishimura, H. et al. (2000): Engagement of the PD-1 immunoinhibitory receptor by a novel B7 family member leads to negative regulation of lymphocyte activation. In *The Journal of experimental medicine* 192 (7), pp. 1027–1034.
- Friedrich, Juergen; Ebner, Reinhard; Kunz-Schughart, Leoni A. (2007): Experimental anti-tumor therapy in 3-D. Spheroids--old hat or new challenge? In *International journal of radiation biology* 83 (11-12), pp. 849–871. DOI: 10.1080/09553000701727531.
- Friedrich, Juergen; Seidel, Claudia; Ebner, Reinhard; Kunz-Schughart, Leoni A. (2009): Spheroid-based drug screen. Considerations and practical approach. In *Nature protocols* 4 (3), pp. 309–324. DOI: 10.1038/nprot.2008.226.
- Gadhamsetty, Saikrishna; Marée, Athanasius F. M.; Boer, Rob J. de; Beltman, Joost B. (2016): Tissue Dimensionality Influences the Functional Response of Cytotoxic T Lymphocyte-Mediated Killing of Targets. In *Frontiers in immunology* 7, p. 668. DOI: 10.3389/fimmu.2016.00668.
- Gaedtke, Lars; Thoenes, Lilja; Culmsee, Carsten; Mayer, Barbara; Wagner, Ernst (2007): Proteomic analysis reveals differences in protein expression in spheroid versus monolayer cultures of low-passage colon carcinoma cells. In *Journal of proteome research* 6 (11), pp. 4111–4118. DOI: 10.1021/pr0700596.
- Gangji, Valérie; Hauzeur, Jean-Philippe; Matos, Celso; Maertelaer, Viviane de; Toungouz, Michel; Lambermont, Micheline (2004): Treatment of osteonecrosis of the femoral head with implantation of autologous bone-marrow cells. A pilot study. In *The Journal of bone and joint surgery. American volume* 86-A (6), pp. 1153–1160.

-
- Garrido, Federico; Romero, Irene; Aptsiauri, Natalia; Garcia-Lora, Angel M. (2016): Generation of MHC class I diversity in primary tumors and selection of the malignant phenotype. In *Int. J. Cancer* 138 (2), pp. 271–280. DOI: 10.1002/ijc.29375.
- Goedecke, Anja; Wobus, Manja; Krech, Mathias; Münch, Nadine; Richter, Katja; Hölig, Kristina; Bornhauser, Martin (2011): Differential effect of platelet-rich plasma and fetal calf serum on bone marrow-derived human mesenchymal stromal cells expanded in vitro. In *Journal of tissue engineering and regenerative medicine* 5 (8), pp. 648–654. DOI: 10.1002/term.359.
- Gojo, Satoshi; Gojo, Noriko; Takeda, Yukiji; Mori, Taisuke; Abe, Hitoshi; Kyo, Shunei et al. (2003): In vivo cardiovascularogenesis by direct injection of isolated adult mesenchymal stem cells. In *Experimental cell research* 288 (1), pp. 51–59.
- Goodman, Harold S. (1961): A General Method for the Quantitation of Immune Cytolysis. In *Nature* 190 (4772), pp. 269–270. DOI: 10.1038/190269a0.
- Gottfried, Eva; Kunz-Schughart, Leoni A.; Andreesen, Reinhard; Kreutz, Marina (2006): Brave little world. Spheroids as an in vitro model to study tumor-immune-cell interactions. In *Cell cycle (Georgetown, Tex.)* 5 (7), pp. 691–695. DOI: 10.4161/cc.5.7.2624.
- Hadrup, Sine; Donia, Marco; Thor Straten, Per (2013): Effector CD4 and CD8 T cells and their role in the tumor microenvironment. In *Cancer microenvironment : official journal of the International Cancer Microenvironment Society* 6 (2), pp. 123–133. DOI: 10.1007/s12307-012-0127-6.
- Halfter, Kathrin; Hoffmann, Oliver; Ditsch, Nina; Ahne, Mareike; Arnold, Frank; Paepke, Stefan et al. (2016): Testing chemotherapy efficacy in HER2 negative breast cancer using patient-derived spheroids. In *Journal of translational medicine* 14 (1), p. 112. DOI: 10.1186/s12967-016-0855-3.
- Hammer, Katharina; Kazcorowski, Adam; Liu, Li; Behr, Michael; Schemmer, Peter; Herr, Ingrid; Nettelbeck, Dirk M. (2015): Engineered adenoviruses combine enhanced oncolysis with improved virus production by mesenchymal stromal carrier cells. In *Int. J. Cancer* 137 (4), pp. 978–990. DOI: 10.1002/ijc.29442.
- Han, Xiao-Yan; Wei, Bo; Fang, Jia-Feng; Zhang, Shi; Zhang, Fu-Cheng; Zhang, Hai-Bo et al. (2013): Epithelial-mesenchymal transition associates with maintenance of stemness in spheroid-derived stem-like colon cancer cells. In *PloS one* 8 (9), e73341. DOI: 10.1371/journal.pone.0073341.
- Hirschberg, Henry; Sun, Chung-Ho; Krasieva, Tatiana; Madsen, Steen J. (2006): Effects of ALA-mediated photodynamic therapy on the invasiveness of human glioma cells. In *Lasers in surgery and medicine* 38 (10), pp. 939–945. DOI: 10.1002/lsm.20445.

-
- Hirschhaeuser, Franziska; Menne, Heike; Dittfeld, Claudia; West, Jonathan; Mueller-Klieser, Wolfgang; Kunz-Schughart, Leoni A. (2010): Multicellular tumor spheroids. An underestimated tool is catching up again. In *Journal of biotechnology* 148 (1), pp. 3–15. DOI: 10.1016/j.jbiotec.2010.01.012.
- Honczarenko, Marek; Le, Yi; Swierkowski, Marcin; Ghiran, Ionita; Glodek, Aleksandra M.; Silberstein, Leslie E. (2006): Human bone marrow stromal cells express a distinct set of biologically functional chemokine receptors. In *Stem cells (Dayton, Ohio)* 24 (4), pp. 1030–1041. DOI: 10.1634/stemcells.2005-0319.
- Huh, Dongeun; Hamilton, Geraldine A.; Ingber, Donald E. (2011): From 3D cell culture to organs-on-chips. In *Trends in cell biology* 21 (12), pp. 745–754. DOI: 10.1016/j.tcb.2011.09.005.
- Ishiguro, Tatsuya; Ohata, Hirokazu; Sato, Ai; Yamawaki, Kaoru; Enomoto, Takayuki; Okamoto, Koji (2017): Tumor-derived spheroids. Relevance to cancer stem cells and clinical applications. In *Cancer science* 108 (3), pp. 283–289. DOI: 10.1111/cas.13155.
- Janicki, Claire N.; Jenkinson, S. Rhiannon; Williams, Neil A.; Morgan, David J. (2008): Loss of CTL function among high-avidity tumor-specific CD8+ T cells following tumor infiltration. In *Cancer research* 68 (8), pp. 2993–3000. DOI: 10.1158/0008-5472.CAN-07-5008.
- Jenkins, M. R.; La Gruta, N. L.; Doherty, P. C.; Trapani, J. A.; Turner, S. J.; Waterhouse, N. J. (2009): Visualizing CTL activity for different CD8+ effector T cells supports the idea that lower TCR/epitope avidity may be advantageous for target cell killing. In *Cell death and differentiation* 16 (4), pp. 537–542. DOI: 10.1038/cdd.2008.176.
- Johnson, Laura A.; Morgan, Richard A.; Dudley, Mark E.; Cassard, Lydie; Yang, James C.; Hughes, Marybeth S. et al. (2009): Gene therapy with human and mouse T-cell receptors mediates cancer regression and targets normal tissues expressing cognate antigen. In *Blood* 114 (3), pp. 535–546. DOI: 10.1182/blood-2009-03-211714.
- Kajiwara, Toshimitsu; Tanaka, Tsutomu; Kukita, Kazuharu; Kutomi, Goro; Saito, Keita; Okuya, Koichi et al. (2016): Hypoxia augments MHC class I antigen presentation via facilitation of ERO1- α -mediated oxidative folding in murine tumor cells. In *European journal of immunology* 46 (12), pp. 2842–2851. DOI: 10.1002/eji.201646525.
- Kakinuma, Takashi; Hwang, Sam T. (2006): Chemokines, chemokine receptors, and cancer metastasis. In *Journal of leukocyte biology* 79 (4), pp. 639–651. DOI: 10.1189/jlb.1105633.
- Kanehira, M.; Xin, H.; Hoshino, K.; Maemondo, M.; Mizuguchi, H.; Hayakawa, T. et al. (2007): Targeted delivery of NK4 to multiple lung tumors by bone marrow-derived mesenchymal stem cells. In *Cancer Gene Ther* 14 (11), pp. 894–903. DOI: 10.1038/sj.cgt.7701079.
- Karnoub, Antoine E.; Dash, Ajeeta B.; Vo, Annie P.; Sullivan, Andrew; Brooks, Mary W.; Bell, George W. et al. (2007): Mesenchymal stem cells within tumour stroma promote breast cancer metastasis. In *Nature* 449 (7162), pp. 557–563. DOI: 10.1038/nature06188.

-
- Karp, Jeffrey M.; Leng Teo, Grace Sock (2009): Mesenchymal stem cell homing. The devil is in the details. In *Cell stem cell* 4 (3), pp. 206–216. DOI: 10.1016/j.stem.2009.02.001.
- Kawai, K.; Hayashi, H.; Ozaki, Y.; Saijo, K.; Liu, S. Q.; Akaza, H.; Ohno, T. (2001): Assessment of the number of local cytotoxic T lymphocytes required for degradation of micrometer-size tumor spheroids. In *Cytotechnology* 37 (1), pp. 31–40. DOI: 10.1023/A:1016139010531.
- Keefe, Dennis; Shi, Lianfa; Feske, Stefan; Massol, Ramiro; Navarro, Francisco; Kirchhausen, Tomas; Lieberman, Judy (2005): Perforin triggers a plasma membrane-repair response that facilitates CTL induction of apoptosis. In *Immunity* 23 (3), pp. 249–262. DOI: 10.1016/j.immuni.2005.08.001.
- Kern, Susanne; Eichler, Hermann; Stoeve, Johannes; Klüter, Harald; Bieback, Karen (2006): Comparative analysis of mesenchymal stem cells from bone marrow, umbilical cord blood, or adipose tissue. In *Stem cells (Dayton, Ohio)* 24 (5), pp. 1294–1301. DOI: 10.1634/stemcells.2005-0342.
- Komarova, Svetlana; Kawakami, Yosuke; Stoff-Khalili, Mariam A.; Curiel, David T.; Pereboeva, Larisa (2006): Mesenchymal progenitor cells as cellular vehicles for delivery of oncolytic adenoviruses. In *Molecular cancer therapeutics* 5 (3), pp. 755–766. DOI: 10.1158/1535-7163.MCT-05-0334.
- Krummel, M. F.; Allison, J. P. (1995): CD28 and CTLA-4 have opposing effects on the response of T cells to stimulation. In *The Journal of experimental medicine* 182 (2), pp. 459–465.
- Krummel, Matthew F.; Heath, William R.; Allison, Janette (1999): Differential Coupling of Second Signals for Cytotoxicity and Proliferation in CD8+ T Cell Effectors: Amplification of the Lytic Potential by B7. In *The Journal of Immunology* 163 (6), pp. 2999–3006.
- Kumar, Sanjay; Ponnazhagan, Selvarangan (2007): Bone homing of mesenchymal stem cells by ectopic alpha 4 integrin expression. In *FASEB journal : official publication of the Federation of American Societies for Experimental Biology* 21 (14), pp. 3917–3927. DOI: 10.1096/fj.07-8275com.
- Kyriakou, Charalampia; Rabin, Neil; Pizzey, Arnold; Nathwani, Amit; Yong, Kwee (2008): Factors that influence short-term homing of human bone marrow-derived mesenchymal stem cells in a xenogeneic animal model. In *Haematologica* 93 (10), pp. 1457–1465. DOI: 10.3324/haematol.12553.
- Lazarus, Hillard M.; Koc, Omer N.; Devine, Steven M.; Curtin, Peter; Maziarz, Richard T.; Holland, H. Kent et al. (2005): Cotransplantation of HLA-identical sibling culture-expanded mesenchymal stem cells and hematopoietic stem cells in hematologic malignancy patients. In *Biology of blood and marrow transplantation : journal of the American Society for Blood and Marrow Transplantation* 11 (5), pp. 389–398. DOI: 10.1016/j.bbmt.2005.02.001.
- Le Blanc, Katarina; Rasmusson, Ida; Sundberg, Berit; Götherström, Cecilia; Hassan, Moustapha; Uzunel, Mehmet; Ringdén, Olle (2004): Treatment of severe acute graft-versus-host disease with third party haploidentical

- mesenchymal stem cells. In *Lancet (London, England)* 363 (9419), pp. 1439–1441. DOI: 10.1016/S0140-6736(04)16104-7.
- Lee, Miyoung; Jeong, Sang Young; Ha, Jueun; Kim, Miyeon; Jin, Hye Jin; Kwon, Soon-Jae et al. (2014): Low immunogenicity of allogeneic human umbilical cord blood-derived mesenchymal stem cells in vitro and in vivo. In *Biochemical and biophysical research communications* 446 (4), pp. 983–989. DOI: 10.1016/j.bbrc.2014.03.051.
- Leibacher, Johannes; Henschler, Reinhard (2016): Biodistribution, migration and homing of systemically applied mesenchymal stem/stromal cells. In *Stem cell research & therapy* 7, p. 7. DOI: 10.1186/s13287-015-0271-2.
- Lin, Jiaying; Liu, Xishi; Ding, Ding (2015): Evidence for epithelial-mesenchymal transition in cancer stem-like cells derived from carcinoma cell lines of the cervix uteri. In *International journal of clinical and experimental pathology* 8 (1), pp. 847–855.
- Linette, Gerald P.; Stadtmauer, Edward A.; Maus, Marcela V.; Rapoport, Aaron P.; Levine, Bruce L.; Emery, Lyndsey et al. (2013): Cardiovascular toxicity and titin cross-reactivity of affinity-enhanced T cells in myeloma and melanoma. In *Blood* 122 (6), pp. 863–871. DOI: 10.1182/blood-2013-03-490565.
- Lüttichau, Irene von; Notohamiprodjo, Mike; Wechselberger, Alexandra; Peters, Christina; Henger, Anna; Seliger, Christian et al. (2005): Human adult CD34- progenitor cells functionally express the chemokine receptors CCR1, CCR4, CCR7, CXCR5, and CCR10 but not CXCR4. In *Stem cells and development* 14 (3), pp. 329–336. DOI: 10.1089/scd.2005.14.329.
- Maione, C.; Botti, C.; Coppola, C. A.; Silvestroni, C.; Lillo, S.; Schiavone, V. et al. (2013): Effect of autologous transplantation of bone marrow cells concentrated with the MarrowXpress system in patients with critical limb ischemia. In *Transplantation proceedings* 45 (1), pp. 402–406. DOI: 10.1016/j.transproceed.2012.10.031.
- Maude, Shannon L.; Laetsch, Theodore W.; Buechner, Jochen; Rives, Susana; Boyer, Michael; Bittencourt, Henrique et al. (2018): Tisagenlecleucel in Children and Young Adults with B-Cell Lymphoblastic Leukemia. In *The New England journal of medicine* 378 (5), pp. 439–448. DOI: 10.1056/NEJMoa1709866.
- Mayer, B.; Klement, G.; Kaneko, M.; Man, S.; Jothy, S.; Rak, J.; Kerbel, R. S. (2001): Multicellular gastric cancer spheroids recapitulate growth pattern and differentiation phenotype of human gastric carcinomas. In *Gastroenterology* 121 (4), pp. 839–852.
- Mesnil, M.; Yamasaki, H. (2000): Bystander effect in herpes simplex virus-thymidine kinase/ganciclovir cancer gene therapy. Role of gap-junctional intercellular communication. In *Cancer research* 60 (15), pp. 3989–3999.
- Moolten, F. L. (1986): Tumor chemosensitivity conferred by inserted herpes thymidine kinase genes. Paradigm for a prospective cancer control strategy. In *Cancer research* 46 (10), pp. 5276–5281.
- Morgan, Richard A.; Yang, James C.; Kitano, Mio; Dudley, Mark E.; Laurencot, Carolyn M.; Rosenberg, Steven A. (2010): Case report of a serious adverse event following the administration of T cells transduced with a chimeric

antigen receptor recognizing ERBB2. In *Molecular therapy : the journal of the American Society of Gene Therapy* 18 (4), pp. 843–851. DOI: 10.1038/mt.2010.24.

Moscona, A. (1957): The development in vitro of chimeric aggregates of dissociated embryonic chick and mouse cells. In *Proceedings of the National Academy of Sciences of the United States of America* 43 (1), pp. 184–194.

Murphy, Kenneth M.; Weaver, Casey (2017): Janeway's immunobiology. With assistance of Allan Mowat, Leslie Berg, David Chaplin, Charles Janeway, Paul Travers, Mark Walport. 9th edition. New York, London: GS Garland Science Taylor & Francis Group.

Nakamizo, Akira; Marini, Frank; Amano, Toshiyuki; Khan, Asadullah; Studeny, Matus; Gumin, Joy et al. (2005): Human bone marrow-derived mesenchymal stem cells in the treatment of gliomas. In *Cancer research* 65 (8), pp. 3307–3318. DOI: 10.1158/0008-5472.CAN-04-1874.

Neelapu, Sattva S.; Locke, Frederick L.; Bartlett, Nancy L.; Lekakis, Lazaros J.; Miklos, David B.; Jacobson, Caron A. et al. (2017): Axicabtagene Ciloleucel CAR T-Cell Therapy in Refractory Large B-Cell Lymphoma. In *The New England journal of medicine* 377 (26), pp. 2531–2544. DOI: 10.1056/NEJMoa1707447.

Nicholas, T. W.; Read, S. B.; Burrows, F. J.; Kruse, C. A. (2003): Suicide gene therapy with Herpes simplex virus thymidine kinase and ganciclovir is enhanced with connexins to improve gap junctions and bystander effects. In *Histology and histopathology* 18 (2), pp. 495–507. DOI: 10.14670/HH-18.495.

Niess, Hanno; Bao, Qi; Conrad, Claudius; Zischek, Christoph; Notohamiprodjo, Mike; Schwab, Felix et al. (2011): Selective targeting of genetically engineered mesenchymal stem cells to tumor stroma microenvironments using tissue-specific suicide gene expression suppresses growth of hepatocellular carcinoma. In *Annals of surgery* 254 (5), 767-74; discussion 774-5. DOI: 10.1097/SLA.0b013e3182368c4f.

Niess, Hanno; Einem, Jobst C. von; Thomas, Michael N.; Michl, Marlies; Angele, Martin K.; Huss, Ralf et al. (2015): Treatment of advanced gastrointestinal tumors with genetically modified autologous mesenchymal stromal cells (TREAT-ME1). Study protocol of a phase I/II clinical trial. In *BMC cancer* 15, p. 237. DOI: 10.1186/s12885-015-1241-x.

NIH. U.S. National Library of Medicine (2018): ClinicalTrials.gov - Mesenchymal stem cells. Available online at <https://clinicaltrials.gov/ct2/results?cond=&term=mesenchymal+stem+cells&cntry=&state=&city=&dist=>, checked on 2/12/2018.

Noman, Muhammad Zaeem; Desantis, Giacomo; Janji, Bassam; Hasmim, Meriem; Karray, Saoussen; Dessen, Philippe et al. (2014): PD-L1 is a novel direct target of HIF-1 α , and its blockade under hypoxia enhanced MDSC-mediated T cell activation. In *The Journal of experimental medicine* 211 (5), pp. 781–790. DOI: 10.1084/jem.20131916.

Noto, Alessandra; Ngauv, Pearline; Trautmann, Lydie (2013): Cell-based flow cytometry assay to measure cytotoxic activity. In *Journal of visualized experiments : JoVE* (82), e51105. DOI: 10.3791/51105.

-
- Olive, Peggy L.; Vikse, Charlene; Trotter, Martin J. (1992): Measurement of oxygen diffusion distance in tumor cubes using a fluorescent hypoxia probe. In *International Journal of Radiation Oncology*Biophysics* 22 (3), pp. 397–402. DOI: 10.1016/0360-3016(92)90840-E.
- Ollion, Jean; Cochenec, Julien; Loll, François; Escudé, Christophe; Boudier, Thomas (2013): TANGO. A generic tool for high-throughput 3D image analysis for studying nuclear organization. In *Bioinformatics (Oxford, England)* 29 (14), pp. 1840–1841. DOI: 10.1093/bioinformatics/btt276.
- openspim.org. Available online at http://openspim.org/Welcome_to_the_OpenSPIM_Wiki, checked on 3/19/2018.
- Orimo, Akira; Gupta, Piyush B.; Sgroi, Dennis C.; Arenzana-Seisdedos, Fernando; Delaunay, Thierry; Naeem, Rizwan et al. (2005): Stromal Fibroblasts Present in Invasive Human Breast Carcinomas Promote Tumor Growth and Angiogenesis through Elevated SDF-1/CXCL12 Secretion. In *Cell* 121 (3), pp. 335–348. DOI: 10.1016/j.cell.2005.02.034.
- Pampaloni, Francesco; Ansari, Nariman; Stelzer, Ernst H. K. (2013): High-resolution deep imaging of live cellular spheroids with light-sheet-based fluorescence microscopy. In *Cell and tissue research* 352 (1), pp. 161–177. DOI: 10.1007/s00441-013-1589-7.
- Pauken, Kristen E.; Wherry, E. John (2015): Overcoming T cell exhaustion in infection and cancer. In *Trends in immunology* 36 (4), pp. 265–276. DOI: 10.1016/j.it.2015.02.008.
- Peper, Janet Kerstin; Schuster, Heiko; Löffler, Markus W.; Schmid-Horch, Barbara; Rammensee, Hans-Georg; Stevanović, Stefan (2014): An impedance-based cytotoxicity assay for real-time and label-free assessment of T-cell-mediated killing of adherent cells. In *Journal of immunological methods* 405, pp. 192–198. DOI: 10.1016/j.jim.2014.01.012.
- Pickl, M.; Ries, C. H. (2009): Comparison of 3D and 2D tumor models reveals enhanced HER2 activation in 3D associated with an increased response to trastuzumab. In *Oncogene* 28 (3), pp. 461–468. DOI: 10.1038/onc.2008.394.
- Pitrone, Peter G.; Schindelin, Johannes; Stuyvenberg, Luke; Preibisch, Stephan; Weber, Michael; Eliceiri, Kevin W. et al. (2013): OpenSPIM. An open-access light-sheet microscopy platform. In *Nature methods* 10 (7), pp. 598–599. DOI: 10.1038/nmeth.2507.
- Preibisch, Stephan; Amat, Fernando; Stamataki, Evangelia; Sarov, Mihail; Singer, Robert H.; Myers, Eugene; Tomancak, Pavel (2014): Efficient Bayesian-based multiview deconvolution. In *Nature methods* 11 (6), pp. 645–648. DOI: 10.1038/nmeth.2929.
- Preibisch, Stephan; Saalfeld, Stephan; Schindelin, Johannes; Tomancak, Pavel (2010): Software for bead-based registration of selective plane illumination microscopy data. In *Nature methods* 7 (6), pp. 418–419. DOI: 10.1038/nmeth0610-418.

-
- Prosser, Megan E.; Brown, Christine E.; Shami, Andrew F.; Forman, Stephen J.; Jensen, Michael C. (2012): Tumor PD-L1 co-stimulates primary human CD8(+) cytotoxic T cells modified to express a PD1:CD28 chimeric receptor. In *Molecular immunology* 51 (3-4), pp. 263–272. DOI: 10.1016/j.molimm.2012.03.023.
- Qi, Yu; Jiang, Dongsheng; Sindrilaru, Anca; Stegemann, Agatha; Schatz, Susanne; Treiber, Nicolai et al. (2014): TSG-6 released from intradermally injected mesenchymal stem cells accelerates wound healing and reduces tissue fibrosis in murine full-thickness skin wounds. In *The Journal of investigative dermatology* 134 (2), pp. 526–537. DOI: 10.1038/jid.2013.328.
- Quarto, R.; Mastrogiacomo, M.; Cancedda, R.; Kutepov, S. M.; Mukhachev, V.; Lavroukov, A. et al. (2001): Repair of large bone defects with the use of autologous bone marrow stromal cells. In *The New England journal of medicine* 344 (5), pp. 385–386. DOI: 10.1056/NEJM200102013440516.
- Rangel-Sosa, Martha Montserrat; Aguilar-Córdova, Estuardo; Rojas-Martínez, Augusto (2017): Immunotherapy and gene therapy as novel treatments for cancer. In *Colombia medica (Cali, Colombia)* 48 (3), pp. 138–147. DOI: 10.25100/cm.v48i3.2997.
- Rattigan, Yanique; Hsu, Jing-Mei; Mishra, Pravin J.; Glod, John; Banerjee, Debabrata (2010): Interleukin 6 mediated recruitment of mesenchymal stem cells to the hypoxic tumor milieu. In *Experimental cell research* 316 (20), pp. 3417–3424. DOI: 10.1016/j.yexcr.2010.07.002.
- Reagan, Michaela R.; Seib, F. Philipp; McMillin, Douglas W.; Sage, Elizabeth K.; Mitsiades, Constantine S.; Janes, Sam M. et al. (2012): Stem Cell Implants for Cancer Therapy. TRAIL-Expressing Mesenchymal Stem Cells Target Cancer Cells In Situ. In *Journal of breast cancer* 15 (3), pp. 273–282. DOI: 10.4048/jbc.2012.15.3.273.
- Rodieck, R. W. (1965): Quantitative analysis of cat retinal ganglion cell response to visual stimuli. In *Vision research* 5 (11), pp. 583–601.
- Rosenberg, Steven A.; Yang, James C.; Sherry, Richard M.; Kammula, Udai S.; Hughes, Marybeth S.; Phan, Gao Q. et al. (2011): Durable complete responses in heavily pretreated patients with metastatic melanoma using T-cell transfer immunotherapy. In *Clinical cancer research : an official journal of the American Association for Cancer Research* 17 (13), pp. 4550–4557. DOI: 10.1158/1078-0432.CCR-11-0116.
- Roufas, Constantinos; Chasiotis, Dimitrios; Makris, Anestis; Efstathiades, Christodoulos; Dimopoulos, Christos; Zaravinos, Apostolos (2018): The Expression and Prognostic Impact of Immune Cytolytic Activity-Related Markers in Human Malignancies. A Comprehensive Meta-analysis. In *Frontiers in oncology* 8, p. 27. DOI: 10.3389/fonc.2018.00027.
- Rüster, Brigitte; Göttig, Stephan; Ludwig, Ralf J.; Bistrrian, Roxana; Müller, Stefanie; Seifried, Erhard et al. (2006): Mesenchymal stem cells display coordinated rolling and adhesion behavior on endothelial cells. In *Blood* 108 (12), pp. 3938–3944. DOI: 10.1182/blood-2006-05-025098.

-
- Sadelain, Michel (2017): CD19 CAR T Cells. In *Cell* 171 (7), p. 1471. DOI: 10.1016/j.cell.2017.12.002.
- Sanchez-Ramos, J.; Song, S.; Cardozo-Pelaez, F.; Hazzi, C.; Stedeford, T.; Willing, A. et al. (2000): Adult bone marrow stromal cells differentiate into neural cells in vitro. In *Experimental neurology* 164 (2), pp. 247–256. DOI: 10.1006/exnr.2000.7389.
- Schindelin, Johannes; Arganda-Carreras, Ignacio; Frise, Erwin; Kaynig, Verena; Longair, Mark; Pietzsch, Tobias et al. (2012): Fiji. An open-source platform for biological-image analysis. In *Nature methods* 9 (7), pp. 676–682. DOI: 10.1038/nmeth.2019.
- Schlenker, Ramona (2015): Chimeric co-stimulatory receptors as a strategy to improve the performance of T cells in the tumor environment: turning PD-1-mediated inhibition into activation. Dissertation. Ludwig-Maximilians-University, Munich. Medizinische Fakultät. Available online at <https://edoc.ub.uni-muenchen.de/21381/>.
- Shi, Mingxia; Li, Jing; Liao, Lianming; Chen, Bin; Li, Bingzong; Chen, Lei et al. (2007): Regulation of CXCR4 expression in human mesenchymal stem cells by cytokine treatment. Role in homing efficiency in NOD/SCID mice. In *Haematologica* 92 (7), pp. 897–904.
- Shield, Kristy; Ackland, M. Leigh; Ahmed, Nuzhat; Rice, Gregory E. (2009): Multicellular spheroids in ovarian cancer metastases. Biology and pathology. In *Gynecologic oncology* 113 (1), pp. 143–148. DOI: 10.1016/j.ygyno.2008.11.032.
- Shinagawa, Kei; Kitadai, Yasuhiko; Tanaka, Miwako; Sumida, Tomonori; Kodama, Michiyo; Higashi, Yukihito et al. (2010): Mesenchymal stem cells enhance growth and metastasis of colon cancer. In *Int. J. Cancer* 127 (10), pp. 2323–2333. DOI: 10.1002/ijc.25440.
- Smith, Chris L.; Chaichana, Kaisorn L.; Lee, Young M.; Lin, Benjamin; Stanko, Kevin M.; O'Donnell, Thomas et al. (2015): Pre-exposure of human adipose mesenchymal stem cells to soluble factors enhances their homing to brain cancer. In *Stem cells translational medicine* 4 (3), pp. 239–251. DOI: 10.5966/sctm.2014-0149.
- Spranger, Stefani; Spaapen, Robbert M.; Zha, Yuanyuan; Williams, Jason; Meng, Yuru; Ha, Thanh T.; Gajewski, Thomas F. (2013): Up-regulation of PD-L1, IDO, and T(regs) in the melanoma tumor microenvironment is driven by CD8(+) T cells. In *Science translational medicine* 5 (200), 200ra116. DOI: 10.1126/scitranslmed.3006504.
- Stagg, John; Lejeune, Laurence; Paquin, André; Galipeau, Jacques (2004): Marrow stromal cells for interleukin-2 delivery in cancer immunotherapy. In *Human gene therapy* 15 (6), pp. 597–608. DOI: 10.1089/104303404323142042.
- Storb, Rainer (2012): Edward Donnall Thomas (1920–2012). In *Nature* 491 (7424), p. 334. DOI: 10.1038/491334a.
- Studeny, Matus; Marini, Frank C.; Champlin, Richard E.; Zompetta, Claudia; Fidler, Isaiah J.; Andreeff, Michael (2002): Bone marrow-derived mesenchymal stem cells as vehicles for interferon-beta delivery into tumors. In *Cancer research* 62 (13), pp. 3603–3608.

-
- Sutherland, R. (1988): Cell and environment interactions in tumor microregions. The multicell spheroid model. In *Science* 240 (4849), pp. 177–184. DOI: 10.1126/science.2451290.
- Sutherland, R. M.; MacDonald, H. R.; Howell, R. L. (1977): Multicellular spheroids: a new model target for in vitro studies of immunity to solid tumor allografts. In *Journal of the National Cancer Institute* 58 (6), pp. 1849–1853.
- Sutherland, Robert M.; Inch, W. Rodger; McCredie, John A.; Kruuv, Jack (1970): A Multi-component Radiation Survival Curve Using an in Vitro Tumour Model. In *International Journal of Radiation Biology and Related Studies in Physics, Chemistry and Medicine* 18 (5), pp. 491–495. DOI: 10.1080/09553007014551401.
- Tang, J.; Shalabi, A.; Hubbard-Lucey, V. M. (2018): Comprehensive analysis of the clinical immuno-oncology landscape. In *Annals of oncology : official journal of the European Society for Medical Oncology* 29 (1), pp. 84–91. DOI: 10.1093/annonc/mdx755.
- Tao, Hongyan; Han, Zhibo; Han, Zhong Chao; Li, Zongjin (2016): Proangiogenic Features of Mesenchymal Stem Cells and Their Therapeutic Applications. In *Stem cells international* 2016, p. 1314709. DOI: 10.1155/2016/1314709.
- Tse, William T.; Pendleton, John D.; Beyer, Wendy M.; Egalka, Matthew C.; Guinan, Eva C. (2003): Suppression of allogeneic T-cell proliferation by human marrow stromal cells. Implications in transplantation. In *Transplantation* 75 (3), pp. 389–397. DOI: 10.1097/01.TP.0000045055.63901.A9.
- Verveer, Peter J.; Swoger, Jim; Pampaloni, Francesco; Greger, Klaus; Marcello, Marco; Stelzer, Ernst H. K. (2007): High-resolution three-dimensional imaging of large specimens with light sheet-based microscopy. In *Nature methods* 4 (4), pp. 311–313. DOI: 10.1038/nmeth1017.
- Viganò, Selena; Utzschneider, Daniel T.; Perreau, Matthieu; Pantaleo, Giuseppe; Zehn, Dietmar; Harari, Alexandre (2012): Functional avidity. A measure to predict the efficacy of effector T cells? In *Clinical & developmental immunology* 2012, p. 153863. DOI: 10.1155/2012/153863.
- Vinay, Dass S.; Ryan, Elizabeth P.; Pawelec, Graham; Talib, Wamidh H.; Stagg, John; Elkord, Eyad et al. (2015): Immune evasion in cancer. Mechanistic basis and therapeutic strategies. In *Seminars in cancer biology* 35 Suppl, S185-S198. DOI: 10.1016/j.semcancer.2015.03.004.
- Vinci, Maria; Box, Carol; Eccles, Suzanne A. (2015): Three-dimensional (3D) tumor spheroid invasion assay. In *Journal of visualized experiments : JoVE* (99), e52686. DOI: 10.3791/52686.
- Vlachogiannis, Georgios; Hedayat, Somaieh; Vatsiou, Alexandra; Jamin, Yann; Fernández-Mateos, Javier; Khan, Khurum et al. (2018): Patient-derived organoids model treatment response of metastatic gastrointestinal cancers. In *Science* 359 (6378), pp. 920–926. DOI: 10.1126/science.aao2774.
- Wang, Ching-Wei; Budiman Gosno, Eric; Li, Yen-Sheng (2015): Fully automatic and robust 3D registration of serial-section microscopic images. In *Scientific reports* 5, p. 15051. DOI: 10.1038/srep15051.

-
- Wang, Jishi; Ma, Dan; Li, Yan; Yang, Yuan; Hu, Xiaoyan; Zhang, Wei; Fang, Qin (2014): Targeted delivery of CYP2E1 recombinant adenovirus to malignant melanoma by bone marrow-derived mesenchymal stem cells as vehicles. In *Anti-cancer drugs* 25 (3), pp. 303–314. DOI: 10.1097/CAD.0000000000000046.
- WHO (2018): Cancer - Fact sheet. Available online at <http://www.who.int/mediacentre/factsheets/fs297/en/>, updated on February 2018, checked on 2/12/2018.
- Wiedemann, Aurelie; Depoil, David; Faroudi, Mustapha; Valitutti, Salvatore (2006): Cytotoxic T lymphocytes kill multiple targets simultaneously via spatiotemporal uncoupling of lytic and stimulatory synapses. In *Proceedings of the National Academy of Sciences of the United States of America* 103 (29), pp.10985–10990. DOI: 10.1073/pnas.0600651103.
- Wilde, Susanne; Sommermeyer, Daniel; Frankenberger, Bernhard; Schiemann, Matthias; Milosevic, Slavoljub; Spranger, Stefani et al. (2009): Dendritic cells pulsed with RNA encoding allogeneic MHC and antigen induce T cells with superior antitumor activity and higher TCR functional avidity. In *Blood* 114 (10), pp. 2131–2139. DOI: 10.1182/blood-2009-03-209387.
- Williams, Adam R.; Trachtenberg, Barry; Velazquez, Darcy L.; McNiece, Ian; Altman, Peter; Rouy, Didier et al. (2011): Intramyocardial stem cell injection in patients with ischemic cardiomyopathy. Functional recovery and reverse remodeling. In *Circulation research* 108 (7), pp. 792–796. DOI: 10.1161/CIRCRESAHA.111.242610.
- Witt Hamer, P. C. de; van Tilborg, A. A. G.; Eijk, P. P.; Sminia, P.; Troost, D.; van Noorden, C. J. F. et al. (2008): The genomic profile of human malignant glioma is altered early in primary cell culture and preserved in spheroids. In *Oncogene* 27 (14), pp. 2091–2096. DOI: 10.1038/sj.onc.1210850.
- Witt Hamer, Philip C. de; Leenstra, Sieger; van Noorden, Cornelis J. F.; Zwinderman, Aeilko H. (2009): Organotypic glioma spheroids for screening of experimental therapies. How many spheroids and sections are required? In *Cytometry. Part A : the journal of the International Society for Analytical Cytology* 75 (6), pp. 528–534. DOI: 10.1002/cyto.a.20716.
- Xie, Chengying; Yang, Zhangru; Suo, Yuanzhen; Chen, Qianqian; Wei, Dan; Weng, Xiaofu et al. (2017): Systemically Infused Mesenchymal Stem Cells Show Different Homing Profiles in Healthy and Tumor Mouse Models. In *Stem cells translational medicine* 6 (4), pp. 1120–1131. DOI: 10.1002/sctm.16-0204.
- Yamout, Bassem; Hourani, Roula; Salti, Haytham; Barada, Wissam; El-Hajj, Taghrid; Al-Kutoubi, Aghiad et al. (2010): Bone marrow mesenchymal stem cell transplantation in patients with multiple sclerosis. A pilot study. In *Journal of neuroimmunology* 227 (1-2), pp. 185–189. DOI: 10.1016/j.jneuroim.2010.07.013.
- Zhuang, Yu; Chen, Xin; Xu, Ming; Zhang, Lei-yang; Xiang, Fei (2009): Chemokine stromal cell-derived factor 1/CXCL12 increases homing of mesenchymal stem cells to injured myocardium and neovascularization following myocardial infarction. In *Chinese medical journal* 122 (2), pp. 183–187.

11 Appendix

11.1 Fiji macros and workflow for SPIM data processing

All SPIM data files were processed semi-automatically using the Fiji Multiview Reconstruction plugin according to the following workflow:

1. Data files were processed automatically with a macro combining the Fiji Multiview Reconstruction plugin functions to split original files into single channels, define datasets for multiview reconstruction, resave in HDF5 format, detect interest points and register datasets based on interest points:

1_SplitDefineHDF5DetectRegister.py

2. To reduce image size a bounding box was defined manually for each dataset on the HDF5 files using the MultiView Reconstruction Application.

3. Data files were processed automatically with a macro to fuse and deconvolve datasets:

3_FuseAndDeconvolve.py

Macros:

1_SplitDefineHDF5DetectRegister.py

```
By David Hoerl
from ij import IJ;
from ij import ImagePlus;
from ij import ImageStack;
from ij.process import ImageProcessor;
from ij.io import DirectoryChooser
import os.path;
import os;
import glob;
import re
import xml.etree.ElementTree as ET

# input directory goes here
dc = DirectoryChooser("Choose directory to process!")
inputDir = dc.getDirectory()
# set to True if you want to process all subdirectories of input
# or False if you only want to process the one input dir
processSubdirs = True;
# subdirectories to be ignored
ignoreDirectories = ["488", "561", "562", "convert", "mv-workspace"]

xdist = ".650"
ydist = ".650"
zdist = "6"
channelWithBeads = "1"
radius1 = "1"
radius2 = "2"
sigma1 = '1.8'
threshold = "0.002"
```



```

threshold_dog = '0.008'
# channelsToFuse = [1,2]
channelsToDeconvolve = ["1"]
downsample=1
nIterations = 10

def splitChannelsForMV(path):
    if not path.endswith(os.sep):
        path += os.sep;
    # create output directory
    if not os.path.exists(path + "mv-workspace"):
        os.makedirs(path + "mv-workspace");
    if os.path.exists(os.path.join(path, "mv-workspace", "OSPLITDONE")):
        print("Already processed that dir. To redo it, delete the OSPLITDONE file!")
        return
    # get all image files (*.ome.tif)
    imageFiles = glob.glob(path + "*.ome.tif");
    for f in imageFiles:
        img = IJ.openImage(f);
        # create new Stack for each channel
        channelStacks = [];
        nChannels = img.getNChannels();
        for i in range(nChannels):
            channelStacks.append(img.createEmptyStack());
        # print(img.getNSlices());
        for i in range(1, img.getNSlices() + 1):
            for j in range(1, nChannels+1):
                img.setC(j);
                img.setZ(i);
                channelStacks[j-1].addSlice(img.getProcessor());
        channelImgs = [];
        for i in range(1, nChannels + 1):
            channelImgs.append(ImagePlus("channel " + str(i), channelStacks[i-1]));
        for i in range(1, nChannels + 1):
            (h, t) = os.path.split(f);
            newFile = h + "/mv-workspace/" + t.split(".ome.tif")[0] + "_Channel" + str(i) + ".ome.tif"
            print("saving: " + newFile);
            IJ.saveAsTiff(channelImgs[i-1], newFile);
        open(os.path.join(path, "mv-workspace", "OSPLITDONE"), 'a').close()

def anyMatches(strings, regex):
    # check wether any of the strings in strings ends with a suffix
    p = re.compile(regex)
    for s in strings:
        if p.match(s):
            return True
    return False

def registerMV(path, doDoG = True):
    if os.path.exists(os.path.join(path, "1REGISTERDONE")):
        print("Already processed that dir. To redo it, delete the 1REGISTERDONE file!")
        return
    files = os.walk(path).next()[2]
    pref = set()
    posnrs = set()
    chnrs = set()
    p = re.compile("(.*_Pos(\\d+)_Channel(\\d+).ome.tif")

    for f in files:
        m = p.match(f)
        if m:
            pref.add(m.groups()[0])
            posnrs.add(m.groups()[1])
            chnrs.add(m.groups()[2])

    if len(pref) != 1:
        print("Filenames in this dir don't match. Please name files in the form: *_Pos{a}_Channel{c}.ome.tif")
        return
    filepattern = iter(pref).next() + "Pos{a}_Channel{c}.ome.tif"

    ### DEFINE DATASET
    datadef = "Define Multi-View Dataset"
    commandDatadef = ("type_of_dataset=[Image Stacks (ImageJ Opener)]

```

```

        xml_filename=dataset.xml      multiple_timepoints=[NO      (one      time-point)]
multiple_channels=[YES (one file per channel)]
        _____multiple_illumination_directions=[NO      (one      illumination      direction)]
multiple_angles=[YES (one file per angle)]
        image_file_directory="" + path
        + "" image_file_pattern="" + filepattern
        + " channels_" + ",".join(chnrs) + " acquisition_angles_" + ",".join(posnrs) +
        "" calibration_type=[Same voxel-size for all views] calibration_definition=[User define
voxel-size(s)]
        imglib2_data_container=[ArrayImg (faster)]
        pixel_distance_x="" + xdist + " pixel_distance_y="" + ydist + " pixel_distance_z="" +
zdist + " pixel_unit=um"
    )

IJ.run(datadef, commandDatadef)

### DETECT INTEREST POINTS
detectip = "Detect Interest Points for Registration"

if not doDoG:
    commandDetectIP = ("select_xml="" + os.path.join(path, "dataset.xml") +
        " process_angle=[All angles] process_channel=[Single channel (Select from List)]" +
        " process_illumination=[All illuminations] process_timepoint=[All Timepoints]" +
        "processing_channel=[channel      "+"      channelWithBeads      +"]"]
type_of_interest_point_detection=[Difference-of-Mean (Integral image based)]"+
        " label_interest_points=beads subpixel_localization=[3-dimensional quadratic fit]"
interest_point_specification=[Advanced ...]" +
        "radius_1="+radius1+" radius_2="+radius2+" threshold="+threshold+" find_maxima"
    )
else:
    commandDetectIP = ("select_xml="" + os.path.join(path, "dataset.xml") +
        " process_angle=[All angles] process_channel=[Single channel (Select from List)]" +
        " process_illumination=[All illuminations] process_timepoint=[All Timepoints]" +
        "processing_channel=[channel      "+"      channelWithBeads      +"]"]
type_of_interest_point_detection=Difference-of-Gaussian"+
        " label_interest_points=beads downsample_images subpixel_localization=[3-
dimensional quadratic fit] interest_point_specification=[Advanced ...]" +
        "downsample_xy=2x downsample_z=1x sigma="+ str(sigma1) + " threshold="" +
str(threshold_dog) + " find_maxima compute_on=[CPU (Java)]"
    )

IJ.run(detectip, commandDetectIP)

### REGISTER
register = "Register Dataset based on Interest Points"
commandRegister = ("select_xml="" + os.path.join(path, "dataset.xml") +
    " process_angle=[All angles] process_illumination=[All illuminations] process_timepoint=[All
Timepoints]" +
    " registration_algorithm=[Fast 3d geometric hashing (rotation invariant)]" +
    "type_of_registration=[Register timepoints individually] interest_points_channel_1="" +
    "beads" if channelWithBeads == "1" else "[DO NOT register this channel]" +
    " interest_points_channel_2="" + "beads" if channelWithBeads == "2" else "[DO NOT register this
channel]" +
    "fix_tiles=[Fix first tile]" +
    "map_back_tiles=[Do not map back (use this if tiles are fixed)]" +
    "transformation=Affine allowed_error_for_ransac=5"
    )

IJ.run(register, commandRegister)

### COPY REGISTRATION TO ALL CHANNELS

dupTransform = "Duplicate Transformations"
commandDupTransform = ("apply=[One channel to other channels]" +
    " select_xml="" + os.path.join(path, "dataset.xml") +
    " apply_to_angle=[All angles] apply_to_illumination=[All illuminations]" +
    "apply_to_timepoint=[All Timepoints] source="" + channelWithBeads + " target=[All
Channels]" +
    "duplicate_which_transformations=[Replace all transformations]" )

IJ.run(dupTransform, commandDupTransform)

open(os.path.join(path, "1REGISTERDONE"), 'a').close()

```

```

def checkBoundingBoxAlreadyExists(xml, bbName='My Bounding Box'):
    tree = ET.parse(xml)
    root = tree.getroot()

    bbs = root.find('BoundingBoxes')
    bb = [bbi for bbi in bbs.findall('BoundingBoxDefinition') if bbi.get('name') == bbName]
    return len(bb) < 1

### HDF5
def hDF(path):
    asHDF = "As HDF5"
    commandAsHDF = ("select_xml=" + os.path.join(path, "dataset.xml") +
        " resave_channel=[All channels] resave_illumination=[All illuminations] resave_timepoint=[All Timepoints]
subsampling_factors=[{ {1,1,1}, {2,2,1}, {4,4,1} }]" +
        "hdf5_chunk_sizes=[{ {32,32,4}, {32,32,4}, {16,16,16} }]" + "timepoints_per_partition=1 setups_per_partition=0
use_deflate_compression " +
        "export_path=" + os.path.join(path, "dataset.xml"))

    IJ.run(asHDF,commandAsHDF)

#### CHANNEL SPLITTING
### main()
## handle subdirs
if processSubdirs:
    dirs = os.walk(inputDir)
    sdirs = list()
    for d in dirs:
        skip = False
        for di in ignoreDirectories:
            if di in d[0].split(os.sep):
                skip = True

        if skip: continue
        if anyMatches(d[2], ".*Pos\d+\.ome\.tif"):
            sdirs.append(d[0])

    print("-- Handling multiple input directories:");
    for i in sdirs:
        print("- Handling dir: " + i);
        splitChannelsForMV(i);

## handle only one directory
else:
    print("-- Handling one input directory: " + inputDir);
    splitChannelsForMV(inputDir);

print("Finished.");

#### REGISTRATION
### main()
## handle subdirs
if processSubdirs:
    dirs = os.walk(inputDir)
    sdirs = list()
    for d in dirs:
        if d[0].endswith("mv-workspace"):
            sdirs.append(d[0])

    print("-- Handling multiple input directories:");
    for i in sdirs:
        print("- Handling dir (Registration): " + i);
        registerMV(i);

## handle only one directory
else:
    print("-- Handling one input directory: " + inputDir);
    registerMV(inputDir);

print("Finished.");

#### HDF5
### main()
## handle subdirs
if processSubdirs:

```

```

dirs = os.walk(inputDir)
sdirs = list()
for d in dirs:
    if d[0].endswith("mv-workspace"):
        sdirs.append(d[0])

print("-- Handling multiple input directories:");
for i in sdirs:
    print("- Handling dir (HDF5): " + i);
    hDF(i);

## handle only one directory
else:
    print("-- Handling one input directory: " + inputDir);
    hDF(inputDir);

print("Finished.");

```

3_FuseAndDeconvolve.py

```

By David Hoerl
from ij import IJ;
from ij import ImagePlus;
from ij import ImageStack;
from ij.process import ImageProcessor;
from ij.io import DirectoryChooser
import os.path;
import os;
import glob;
import re
import xml.etree.ElementTree as ET

# input directory goes here
dc = DirectoryChooser("Choose directory to process!")
inputDir = dc.getDirectory()
# set to True if you want to process all subdirectories of input
# or False if you only want to process the one input dir
processSubdirs = True;
# subdirectories to be ignored
ignoreDirectories = ["488", "561", "562", "convert", "mv-workspace"]

xdist = ".650"
ydist = ".650"
zdist = "6"
channelWithBeads = "1"
radius1 = "1"
radius2 = "2"
sigma1 = '1.8'
threshold = "0.002"
threshold_dog = '0.008'
channelsToFuse = [1,2]
channelsToDeconvolve = ["1","2"]
downsample=1
nIterations = 10

def checkBoundingBoxAlreadyExists(xml, bbName='My Bounding Box'):
    tree = ET.parse(xml)
    root = tree.getroot()
    bbs = root.find('BoundingBoxes')
    bb = [bbi for bbi in bbs.findall('BoundingBoxDefinition') if bbi.get('name') == bbName]
    return len(bb) < 1

def fuseAllChannels(path, bbEstimateBG=1, bbName="My Bounding Box"):
    fuse = "Fuse/Deconvolve Dataset"
    fuseCmd = ("select_xml="+ os.path.join(path, "dataset.xml") +
              " process_angle=[All angles] process_channel=[All channels] process_illumination=[All
illuminations] [process_timepoint]=[All Timepoints]"+
              " processing_channel=[channel 1] type_of_image_fusion=[Weighted-average fusion]"+
              " bounding_box=[Use pre-defined Bounding Box] +
              " fused_image=[Save as TIFF stack] bounding_box_title=[" + bbName + "]" +
              "downsample=" + str(downsample) + " pixel_type=[32-bit floating point]
imglib2_container=[CellImg (large images)]"+

```

```

        "process_views_in_parallel=All blend interpolation=[Linear Interpolation] "+
        "output_file_directory=" + os.path.join(path, ""))

    IJ.run(fuse, fuseCmd)

def deconvolveAllChannels(path):
    deconvolve = "Fuse/Deconvolve Dataset"
    deconvolveCmd = ("select_xml="+os.path.join(path, "dataset.xml")+
        " process_angle=[All angles] process_channel=[All channels]"+
        " process_illumination=[All illuminations] process_timepoint=[All Timepoints] "+
        " type_of_image_fusion=[Multi-view deconvolution]"+
        " bounding_box=[Use pre-defined Bounding Box] )" +
        "fused_image=[Save as TIFF stack] "+
        "imglib2_container=[CellImg (large images)] imglib2_container_ffts=ArrayImg
type_of_iteration="+
        "[Efficient Bayesian - Optimization I (fast, precise)] image_weights=[Virtual weights (less
memory, slower)] "+
        "osem_acceleration=[1 (balanced)] number_of_iterations="+str(nIterations)+
        " use_tikhonov_regularization tikhonov_parameter=0.0060 "+
        "compute=[in 512x512x512 blocks] compute_on=[GPU (Nvidia CUDA via JNA)] "+
        "psf_estimation=[Extract from beads] psf_display=[Do not show PSFs] "+
        "cuda_directory=/home/ruehland/Fiji.app/lib/linux64
select_native_library_for_cudafourierconvolution=libFourierConvolutionCUDALib.so " +
        "gpu_1 detections_to_extract_psf_for_channel_1=beads
detections_to_extract_psf_for_channel_1=[Same PSF as channel 1] " +
        "psf_size_x=19 psf_size_y=19 psf_size_z=25 " +
        "output_file_directory="+path)

    IJ.run(deconvolve, deconvolveCmd)

def checkBoundingBoxNotEmpty(xml, bbName='My Bounding Box'):
    tree = ET.parse(xml)
    root = tree.getroot()
    bbs = root.find('BoundingBoxes')
    bb = iter([bbi for bbi in bbs.findall('BoundingBoxDefinition') if bbi.get('name') == bbName]).next()
    mins = bb.find('min').text.split(' ')
    maxs = bb.find('max').text.split(' ')
    empty = False
    for i in range(len(mins)):
        if mins[i] >= maxs[i]:
            empty = True
    return not empty

def fuseMV(path):
    if os.path.exists(os.path.join(path, "2FUSEDONE")):
        print("Already processed that dir. To redo it, delete the 2FUSEDONE file!")
        return
    #fuseAllChannels(path)
    deconvolveAllChannels(path)
    open(os.path.join(path, "2FUSEDONE"), 'a').close()

##### FUSION
### main()
## handle subdirs
if processSubdirs:
    dirs = os.walk(inputDir)
    sdirs = list()
    for d in dirs:
        if d[0].endswith("mv-workspace"):
            sdirs.append(d[0])

    print("-- Handling multiple input directories:");
    for i in sdirs:
        print("- Handling dir (Fusion): " + i);
        fuseMV(i);

## handle only one directory
else:
    print("-- Handling one input directory: " + inputDir);
    fuseMV(inputDir);

print("Finished.");

```

11.2 Fiji macros and workflow for invasion assay analysis

All SPIM data files were processed and analyzed semi-automatically using different Fiji plugins according to the following workflows and with respective macros:

11.2.1 Cytoplasmic segmentation of MSC clusters

4. Spheroid and MSCs were segmented and invaded depths measured automatically.

4_InvasionAnalysisOld.py

Macro:

4_InvasionAnalysisOld.py

```
# author: David Hoerl
from Utilities import Counter3D
from mcib3d.geom import Object3D, Vector3D, Point3D
from mcib3d.geom import Object3DPoint, Object3DSurface
from mcib3d.image3d import Segment3DImage
from javax.vecmath import Point3f
from java.util import ArrayList
from java.lang import Integer
from ij.plugin import Resizer
from ij.io import DirectoryChooser, OpenFileDialog
from ij import IJ, ImagePlus
from ij.process import StackConverter, StackProcessor
import os
import re
import sys

# USER DEFINED PARAMETERS
channelWithMSC = "1"
channelWithSphero = "1"
spheroThreshold = 13
spheroMin = 80000
# spheroMax = Integer.MAX_VALUE
mscThreshold = 40
mscMin = 800
# mscMax = Integer.MAX_VALUE
downsampleXY = 1
downsampleZ = downsampleXY
# handle Directories starting with any of this
# dirPrefixes = ["F", "G"]
# END USER DEFINED PARAMETERS

def startsWithAny(s, prefixes):
    """
    check whether s starts with any of the prefixes in prefixes
    """
    for p in prefixes:
        if s.startswith(p):
            return True
    return False

def assayMV(path, spheroT=spheroThreshold, mscT=mscThreshold, segmentWholeSpheroVolume=False):
    """
    run the invasion assay - image files should be in directory path
    @return: list of distances (in pixels, consider downsampling)
    """
    files = os.walk(path).next()[2]
    fileMSC = ""
```

```

fileSphero = ""
# fused/deconvolved (.tif) files should start with TP0_Ch + channel nr.
reMSC = re.compile("TP0_Ch" + channelWithMSC + ".*?tif")
reSphero = re.compile("TP0_Ch" + channelWithSphero + ".*?tif")

for f in files:
    # find the two input files
    if reMSC.match(f):
        fileMSC = os.path.join(path, f)
    if reSphero.match(f):
        fileSphero = os.path.join(path, f)

print fileMSC
print fileSphero
# load images
imageMSC = IJ.openImage(fileMSC)
imageSphero = IJ.openImage(fileSphero)

# convert to 8bit (TODO: set min/max?)
StackConverter(imageMSC).convertToGray8()
StackConverter(imageSphero).convertToGray8()

# downsample images
imageMSC = Resizer().zScale(imageMSC, int(imageMSC.getNSlices() * downsampleZ), 0)
newW = int(imageMSC.getWidth() * downsampleXY)
newH = int(imageMSC.getHeight() * downsampleXY)
imageMSC.setStack(StackProcessor(imageMSC.getStack()).resize(newW, newH))

imageSphero = Resizer().zScale(imageSphero, int(imageSphero.getNSlices() * downsampleZ), 0)
newW = int(imageSphero.getWidth() * downsampleXY)
newH = int(imageSphero.getHeight() * downsampleXY)
imageSphero.setStack(StackProcessor(imageSphero.getStack()).resize(newW, newH))

# segment cells and get objects
IJ.log("segmenting cells...")
mscSegmenter = Segment3DImage(imageMSC, mscT, Integer.MAX_VALUE)
mscSegmenter.setMinSizeObject(mscMin)
mscSegmenter.segment()
mscObjects = mscSegmenter.getSurfaceObjectsImage3D().getObjects3D()
IJ.log("segmenting cells... done.")
IJ.log("found " + str(len(mscObjects)) + " cells.")

# segment the spheroid
IJ.log("segmenting spheroid...")
spheroSegmenter = Segment3DImage(imageSphero, spheroT, Integer.MAX_VALUE)
spheroSegmenter.setMinSizeObject(spheroMin)
spheroSegmenter.segment()

### Segment the whole sphero instead of just the surface
# this allows checking whether a cell lies inside the volume
# however, the whole volume will be colored in the control image!
if segmentWholeSpheroVolume:
    spheroObjects = spheroSegmenter.getLabelledObjectsImage3D().getObjects3D()
else:
    spheroObjects = spheroSegmenter.getSurfaceObjectsImage3D().getObjects3D()
IJ.log("segmenting spheroid... done.")

# skip dataset if no sphero was found
if len(spheroObjects) == 0:
    IJ.log("ERROR: no spheroid could be found")
    return(list(), None)

maxVolume = 0
biggestObject = 0
for i in range(len(spheroObjects)):
    if spheroObjects[i].getVolumePixels() > maxVolume:
        biggestObject = i
        maxVolume = spheroObjects[i].getVolumePixels()

spheroObject = spheroObjects[biggestObject]

if len(spheroObjects) != 1:
    IJ.log("WARNING: found " + str(len(mscObjects)) + " spheroid objects. Using the biggest.")

```

```

# color copy of msc-image to label segmentations in
imageControl = imageMSC.duplicate()
StackConverter(imageControl).convertToRGB()
# mark spheroid in red
spheroObject.draw(imageControl.getStack(), 255, 0, 0)
#closedSphero = spheroObject.getObject3DSurface()
#closedSphero.draw(imageControl.getStack(), 0, 0, 255)

# calculate distances
distances = list()
nCells = len(mscObjects)
curCell = 1
for o in mscObjects:
    IJ.log("handling cell " + str(curCell) + " of " + str(nCells))
    curCell += 1

    cellCenter = Point3D(o.getCenterX(), o.getCenterY(), o.getCenterZ())

    # skip cells not inside sphero ONLY IF whole sphero was segmented
    if not spheroObject.inside(cellCenter) and segmentWholeSpheroVolume:
        IJ.log("not inside spheroid, skipping.")
        continue

    distances.append(o.distCenterBorderUnit(spheroObject))
    # IJ.log(str(o.distCenterBorderUnit(spheroObject)))
    # mark mscs in green
    o.draw(imageControl.getStack(), 0, 255, 0)

# save control image
# IJ.save(imageControl, os.path.join(path, "control.tif"))
# save distances as CSV
outfile = os.path.join(path, "distances.csv")
outfd = open(outfile, "w+")
outfd.write("distance\r")

for d in distances:
    strValue = str(d)
    strValue = strValue.replace('.', ',')
    outfd.write(strValue + "\r")

outfd.close()
return (distances, imageControl)

# MAIN SCRIPT
# let user pick a directory, process all subdirs
dc = DirectoryChooser("Choose directory to process!")
inputDir = dc.getDirectory()
dc2 = OpenFileDialog("Choose parameter file!")
paramFile = open(os.path.join(dc2.getDirectory(), dc2.getFileName()), "r")
paramDict = dict()

for l in paramFile:
    ls = l.split(",")
    print(ls[3].startswith("CELLSOUTSIDE"))
    # if ls[1]:
    #     paramDict["_" + ls[0:4]] = (int(ls[5]), int(ls[4]), ls[6].startswith("CELLSOUTSIDE"))
    if ls[0]:
        paramDict[ls[0]] = (int(ls[2]), int(ls[1]), ls[3].startswith("CELLSOUTSIDE"))

if inputDir.endswith(os.path.sep):
    inputDir = inputDir[:-1]

dirs = os.walk(inputDir)
sdirs = list()
# process only the "mv-workspace" directories
# of directories starting with specified prefixes
for d in dirs:
    print(d[0])
    if d[0].split(os.path.sep)[-1] in paramDict.keys() and "mv-workspace" in d[1]:
        #if "mv-workspace" in d[1]:
        sdirs.append(os.path.join(d[0], "mv-workspace"))

```

```
resultFd = open(os.path.join(inputDir, "resultsCELLSOUTSIDE.csv"), "w")
delimiter = ";"

IJ.log("-- Handling multiple input directories:");
for i in sdirs:
    experimentName = i.split(os.path.sep)[-2]
    IJ.log("- Handling dir: " + i);
    IJ.log("sphero Threshold: " + str(paramDict[experimentName][0]))
    IJ.log("MSC Threshold: " + str(paramDict[experimentName][1]))
    (tDists, resImage) = assayMV(i, paramDict[experimentName][0], paramDict[experimentName][1],
    paramDict[experimentName][2]);
    resultFd.write(experimentName + delimiter)
    resultFd.write(delimiter.join(map(str, tDists)).replace('.', ','))
    resultFd.write("\n")

    if resImage:
        IJ.save(resImage, os.path.join(inputDir, experimentName + "_control.tif"))
resultFd.close()
```

11.2.2 Nuclear segmentation of single MSCs

4. Segmentation of MSCs is done automatically with a macro. All nuclei within the spheroid are segmented individually based on the 7-AAD nuclear staining with a Difference of Gaussians and a 3D watershed algorithm. The spheroid is segmented based on its autofluorescence signal in the 488 nm channel. Within that mask the CMFDA signal is segmented. All MSC nuclei are determined within CMFDA signal masks.

4_NuclearSegmentationMSC.ijm

5. A macro automatically adds the segmented spheroid objects and their respective MSC objects to the 3D Roi Manager and calculates the shortest distance of each MSC to the spheroid surface.

5_InvasionAnalysis_NuclearSegmentation.ijm

Macros:

4_NuclearSegmentationMSC.ijm

```
// Open Image
input = getDirectory("pick Input directory!");
output = input;
ch1 = "TP0_Ch1_Ill0_Ang1,0,2,3,4";
ch2 = "TP0_Ch2_Ill0_Ang1,0,2,3,4";
spheroThreshold = 12;
mscThreshold = 60;

// loop to process whole folder
list = getFileList(input);
for (i = 0; i < list.length; i++){
    //segmentation(input, output, list[i]);
    masks(input, output, list [i]);
}

function segmentation(input, output, file) {
    // Open image:
    print(input + file + "mv-workspace/" + ch2 + ".tif");
    open(input + file + "mv-workspace/" + ch2 + ".tif");
    setMinAndMax(0, 0.23);
    run("8-bit");
    run("Duplicate...", "duplicate");
    selectWindow(ch2 + ".tif");
    run("Gaussian Blur 3D...", "x=2 y=2 z=2");
    selectWindow(ch2 + "-1.tif");
    run("Gaussian Blur 3D...", "x=4 y=4 z=4");
    imageCalculator("Subtract create stack", ch2 + ".tif", ch2 + "-1.tif");
    run("Bin...", "x=2 y=2 z=2 bin=Max");
    run("3D Watershed", "seeds_threshold=3 image_threshold=0 image=Result seeds=Automatic radius=7.5");
    // Save segmented image
    selectWindow("Watershed");
    saveAs("tiff", input + file + "Watershed.tif");
    print("Watershed finished. Saved " + input + file + "Watershed.tif");
    //Close Images
    selectWindow(ch2 + ".tif");
    close();
    selectWindow(ch2 + "-1.tif");
    close();
    selectWindow("Result of " + ch2 + ".tif");
    close();
}

function masks(input, output, file) {
    // Create Sphero mask
```

```

open(input + file + "mv-workspace/" + ch1 + ".tif");
selectWindow(ch1 + ".tif");
Stack.getStatistics(null, null, min, max);
setMinAndMax(min, max);
run("8-bit");
run("Bin...", "x=2 y=2 z=2 bin=Max");
run("3D OC Options", "show_masked_image_(redirection_required) redirect_to=Watershed.tif");
run("3D Objects Counter", "threshold=" + spheroThreshold + " slice=100 min.=10000 max.=45925560 objects");
selectWindow("Objects map of " + ch1 + ".tif redirect to Watershed.tif");
saveAs("tiff", input + file + "SpheroObject.tif");
print("Saved " + input + file + "SpheroObject.tif");

selectWindow("Masked image for " + ch1 + ".tif redirect to Watershed.tif");
saveAs("tiff", input + file + "SpheroWatershed.tif");
print("Saved " + input + file + "SpheroWatershed.tif");
close();
selectWindow(ch1 + ".tif");
close();

// Create CMFDA mask
open(input + file + "mv-workspace/" + ch1 + ".tif");
Stack.getStatistics(null, null, min, max);
setMinAndMax(min, max);
run("8-bit");
run("Bin...", "x=2 y=2 z=2 bin=Max");
selectWindow("SpheroObject.tif");
run("3D OC Options", "show_masked_image_(redirection_required) redirect_to=" + ch1 + ".tif");
run("3D Objects Counter", "threshold=1 slice=100 min.=10000 max.=45925560 objects");
selectWindow("SpheroObject.tif");
close();
selectWindow("Objects map of SpheroObject.tif redirect to " + ch1 + ".tif");
close();

selectWindow("Masked image for SpheroObject.tif redirect to " + ch1 + ".tif");
run("3D OC Options", "show_masked_image_(redirection_required) redirect_to=Watershed.tif");
run("3D Objects Counter", "threshold=" + mscThreshold + " slice=100 min.=50 max.=45925560 objects");

selectWindow("Objects map of Masked image for SpheroObject.tif redirect to " + ch1 + ".tif redirect to
Watershed.tif");
saveAs("tiff", input + file + "MSCObject.tif");
print("Saved " + input + file + "MSCObject.tif");
close();

selectWindow("Masked image for Masked image for SpheroObject.tif redirect to " + ch1 + ".tif redirect to
Watershed.tif");
saveAs("tiff", input + file + "MSCWatershed.tif");
print("Saved " + input + file + "MSCWatershed.tif");
close();
selectWindow("Masked image for SpheroObject.tif redirect to " + ch1 + ".tif");
close();
selectWindow("Watershed.tif");
close();
selectWindow(ch1 + ".tif");
close();
}

```

5_InvasionAnalysis_NuclearSegmentation.ijm

```

input = getDirectory("pick Input directory!");
output = input + "/ResultsFiltered/";
Objects = "MSCWatershed.tif";
Sphero = "SpheroObject.tif" ;

run("Clear Results");
// loop to process whole folder
list = getFileList(input);
for (i = 0; i < list.length; i++){
    distances(input, output, list[i]);
}

// function

```

```

function distances(input, output, filename) {
    open (input + filename + Objects);
    open (input + filename + Sphero);
// distances
    run("3D Manager");
    selectWindow(Sphero);
    Ext.Manager3D_AddImage();
    Ext.Manager3D_Count(nb);
// initialize min and max
    Ext.Manager3D_Measure3D(0,"Vol",V);
    max=V;
    maxobj=0;
// loop to find max and min volumes
    for(i=1;i<nb;i++) {
        Ext.Manager3D_Measure3D(i,"Vol",V);
        if(V>max) {
            max=V; maxobj=i;
        }
    }
// delete all objects except of the largest
    Ext.Manager3D_GetName(maxobj, maxname);
    for(i=0;i<nb;i++) {
        Ext.Manager3D_GetName(i,actname)
        if(actname!=maxname){
            Ext.Manager3D_MonoSelect();
            Ext.Manager3D_Select(i);
            Ext.Manager3D_Delete();
            Ext.Manager3D_Count(nb);
        }
    }
// measure and save spheroid volume
    Ext.Manager3D_Measure3D(0,"Vol", vol);
    index = lastIndexOf(filename, "/");
    if (index!=-1) filename = substring(filename, 0, index);
    setResult(filename,0,vol);
    selectWindow(Objects);
    Ext.Manager3D_AddImage();
    Ext.Manager3D_Count(nb);
// delete all nuclei smaller than certain volume
    toDelete = newArray();
    toDelete = Array.concat(toDelete, 1);
    for (i = 2; i < nb; i++) {
        Ext.Manager3D_Measure3D(i,"Vol",V);
        if(V<300){
            toDelete = Array.concat(toDelete, i);
        }
    }
    Ext.Manager3D_DeselectAll();
    Ext.Manager3D_MultiSelect();
    for (i = 0; i < toDelete.length; i++){
        Ext.Manager3D_Select(toDelete[i]);
    }
    Ext.Manager3D_Delete();

// measure distances
    Ext.Manager3D_Count(nb_obj);
    for (i = 1; i < nb_obj-1; i++) {
        Ext.Manager3D_Dist2(0,i,"c2b1",dist);
        index = lastIndexOf(filename, "/");
        if (index!=-1) filename = substring(filename, 0, index);
        setResult(filename,i,dist);
    }
// save results
    run("Set Measurements...", " mean limit redirect=None decimal=0");
    saveAs ("Results", output + filename + ".txt");
    Ext.Manager3D_Close();
    close(filename);
    close(Sphero);
    close(Objects);
}

```

11.2.3 Cytoplasmic segmentation of single CTLs

4. Datasets were opened, converted to 8-bit, downsampled and saved automatically with a macro, thresholds for spheroid and cell segmentation were defined manually.

4_FindThresholdsManually.ijm

5. Segmentation of objects of interest is done automatically with a macro. The spheroid is segmented based on the 7-AAD nuclear staining signal and its mask applied to both 488 nm and 561 nm channels. All nuclei within the spheroid are segmented individually based on the 7-AAD nuclear staining and all T cells are segmented individually based on their cytoplasmic CMFDA signal. Single cell segmentation is based on a 3D watershed algorithm.

5_TC-Nuclear-Segmentation.ijm

6. All datasets are opened and merged automatically with their respective binary segmented object files to control spheroid and cell segmentation.

6_ControlComposites.ijm

7. A macro automatically adds the segmented spheroid objects and their respective T cell objects to the 3D Roi Manager and calculates the shortest distance of each T cell to the spheroid surface.

7_InvasionAnalysis.ijm

8. Since the distance to the spheroid surface is not a reliable parameter for cell invasion in case of cytotoxic T cells, a macro finally calculates the shortest distance of each T cell to the spheroid centroid with the 3D Roi Manager.

8_Centroids.ijm

Macros:

4_FindThresholdsManually.ijm

```
input = getDirectory("pick Input directory!");
ch1 = "TP0_Ch1_III0_Ang0,1,2,3,4";
ch2 = "TP0_Ch2_III0_Ang0,1,2,3,4";

open(input + "mv-workspace/" + ch1 + ".tif");
setMinAndMax(0, 0.1);
run("8-bit");
run("Bin...", "x=2 y=2 z=2 bin=Max");
saveAs("tiff", input + "ch1Binned.tif");

open(input + "mv-workspace/" + ch2 + ".tif");
setMinAndMax(0, 2);
run("8-bit");
run("Bin...", "x=2 y=2 z=2 bin=Max");
saveAs("tiff", input + "ch2.tif");
```

5_TCAndNuclearSegmentation.ijm

```
// Open Image
input = getDirectory("pick Input directory!");
output = input;
ch1 = "TPO_Ch1_Ill0_Ang0,1,2,3,4";
ch2 = "TPO_Ch2_Ill0_Ang0,1,2,3,4";
thresholds = File.openAsString(input + "thresholds.csv");

// loop to process whole folder
list = getFileList(input);
for (i = 0; i < list.length; i++){
    masks(input, output, list [i]);
}

function threshold(file) {
    rows=split(thresholds, "\n");
    for(i=0; i<rows.length; i++){
        columns=split(rows[i], ",");
        if (columns[0] == file) {
            spheroThreshold = parseInt(columns[1]);
            TC = parseInt(columns[2]);
            IT = parseInt(columns[3]);
            print(spheroThreshold, TC, IT);
        }
    }
}

function masks(input, output, file) {
    rows=split(thresholds, "\n");
    thresholdfound = false;
    for(i=0; i<rows.length; i++){
        columns=split(rows[i], ",");
        if (columns[0] == file) {
            spheroThreshold = parseInt(columns[1]);
            TC = parseInt(columns[2]);
            IT = parseInt(columns[3]);
            print("SpheroThreshold = " + spheroThreshold + ", TC = " + TC + ", IT = " + IT);
            print("SpheroThreshold = " + spheroThreshold);
            thresholdfound = true;
        }
    }
    if (!thresholdfound) {
        print("Thresholds not found.");
        return;
    };
}

// Create Sphero-masked images of Channel 1 and 2
print("Processing " + file);
open(input + file + "ch2.tif");
open(input + file + "ch1Binned.tif");
selectWindow("ch2.tif");
run("3D OC Options", "show_masked_image_(redirection_required) redirect_to=ch1Binned.tif");
run("3D Objects Counter", "threshold=" + spheroThreshold + " slice=100 min.=10000 max.=45925560 objects");
selectWindow("Objects map of ch2.tif redirect to ch1Binned.tif");
saveAs("tiff", input + file + "SpheroObject.tif");
print("Saved " + input + file + "SpheroObject.tif");
selectWindow("SpheroObject.tif");
close();
selectWindow("ch1Binned.tif");
close();

// nuclear segmentation
selectWindow("ch2.tif");
run("3D Watershed", "seeds_threshold=30 image_threshold=26 image=ch2 seeds=Automatic radius=3");
saveAs("tiff", input + file + "Nuclei.tif");
print("Saved " + input + file + "Nuclei.tif");
close();
selectWindow("ch2.tif");
close();

// segment TCells
selectWindow("Masked image for ch2.tif redirect to ch1Binned.tif");
```

```

        saveAs("tiff", input + file + "ch1.tif");
        run("3D Watershed", "seeds_threshold=" + TC + " image_threshold=" + IT + " image=ch1 seeds=Automatic
radius=3");
        saveAs("tiff", input + file + "TCObjects.tif");
        print("Saved " + input + file + "TCObjects.tif");
        close();
        selectWindow("ch1.tif");
        close();
    }

```

6_ControlComposites.ijm

```

input = getDirectory("pick Input directory!");

// loop to process whole folder
list = getFileList(input);
for (i = 0; i < list.length; i++){
    composite(input, list [i]);
}

function composite(input, file) {
    open(input + file + "ch1.tif");
    open(input + file + "ch2.tif");
    open(input + file + "TCObjects.tif");
    run("8-bit");
    open(input + file + "SpheroObject.tif");
    setThreshold(1, 255);
    run("Convert to Mask", "method=Default background=Dark");
    run("3D Fill Holes");
    run("Merge Channels...", "c1=TCObjects.tif c3=SpheroObject.tif c4=ch1.tif c5=ch2.tif create");
    selectWindow("Composite");
    rename(file);
}

```

7_InvasionAnalysis.ijm

```

input = getDirectory("pick Input directory!");
output = getDirectory("pick Output directory!");
TC = "TCObjects.tif";
Sphero = "SpheroObject.tif" ;

// loop to process whole folder
list = getFileList(input);
run("Clear Results");
for (i = 0; i < list.length; i++){
    distances(input, output, list[i]);
}

// save results
run("Set Measurements...", " mean limit redirect=None decimal=0");
saveAs ("Results", output + "Results.txt");

// function to measure spheroid volume, T cell and apoptotic cell distances in pixel
function distances(input, output, filename) {
    open (input + filename + TC);
    open (input + filename + Sphero);
    setThreshold(1, 255);
    run("Convert to Mask", "method=Default background=Dark");
    run("3D Fill Holes");
    run("3D Manager");
    selectWindow(Sphero);
    Ext.Manager3D_AddImage();
    Ext.Manager3D_Count(nb);
// initialize min and max
    Ext.Manager3D_Measure3D(0,"Vol",V);
    max=V;
    maxobj=0;
// loop to find max and min volumes
    for(i=1;i<nb;i++) {
        Ext.Manager3D_Measure3D(i,"Vol",V);
        if(V>max) {

```

```

        max=V; maxobj=i;
    }
}
// delete all objects except of the largest
Ext.Manager3D_GetName(maxobj, maxname);
for(i=0;i<nb;i++) {
    Ext.Manager3D_GetName(i,actname)
    if(actname!=maxname){
        Ext.Manager3D_MonoSelect();
        Ext.Manager3D_Select(i);
        Ext.Manager3D_Delete();
        Ext.Manager3D_Count(nb);
        i=i-1;
    }
}

// measure and save spheroid volume
Ext.Manager3D_Measure3D(0,"Vol", vol);
index = lastIndexOf(filename, "_");
end = lastIndexOf(filename, "/");
if (index!=-1) type = substring(filename, 0, index);
if (index!=-1) series = substring(filename, index + 1, end);
n = nResults();
setResult("Type",n, type);
setResult("Series",n, series);
setResult("Variable",n, "Volume");
setResult("Value",n, vol);
print("Spheroid volume saved.");

// measure T cells
selectWindow(TC);
Stack.getStatistics(area,mean);
if (mean >0) {
    Ext.Manager3D_AddImage();
    Ext.Manager3D_Count(nb);
}

// delete all cells smaller than certain volume
Ext.Manager3D_DeselectAll();
for (i = 1; i < nb; i++) {
    Ext.Manager3D_Measure3D(i,"Vol",V);
    if(V<100){
        Ext.Manager3D_MonoSelect();
        Ext.Manager3D_Select(i);
        Ext.Manager3D_Delete();
        Ext.Manager3D_Count(nb);
        i=i-1;
    }
}

// measure distances
Ext.Manager3D_Count(nb_obj);
for (i = 1; i < nb_obj-1; i++) {
    Ext.Manager3D_Dist2(0,i,"c2b1",dist);
    index = lastIndexOf(filename, "_");
    end = lastIndexOf(filename, "/");
    if (index!=-1) type = substring(filename, 0, index);
    if (index!=-1) series = substring(filename, index + 1, end);
    n = nResults();
    setResult("Type",n,type);
    setResult("Series",n,series);
    setResult("Variable",n, "TC");
    setResult("Value",n, dist);
}
}
Ext.Manager3D_Close();
close(Sphero);
close(TC);
}

```

8_InvasionAnalysisCentroids.ijm

```

input = getDirectory("pick Input directory!");
output = input;

```



```

// loop to process whole folder
list = getFileList(input);
for (i = 0; i < list.length; i++){
    centroids(input, output, list [i]);
}

// save results
run("Set Measurements...", " mean limit redirect=None decimal=0");
saveAs ("Results", output + "CentroidResults.txt");

function centroids(input, output, file) {

// Create Sphero Centroid

    print("Processing " + file);
    open(input + file + "SpheroObject.tif");
    open(input + file + "TCObjects.tif");
    selectWindow("SpheroObject.tif");
    run("3D Objects Counter", "threshold=1 slice=100 min.=10000 max.=45925560 centroids");
    selectWindow("Centroids map of SpheroObject.tif");
    saveAs("tiff", input + file + "SpheroCentroid.tif");
    selectWindow("SpheroObject.tif");
    close();
    run("3D Manager");
    selectWindow("SpheroCentroid.tif");
    Ext.Manager3D_AddImage();

// measure T cells
    selectWindow("TCObjects.tif");
    Stack.getStatistics(area,mean);
    if (mean >0) {
        Ext.Manager3D_AddImage();
        Ext.Manager3D_Count(nb);

// delete all cells smaller than certain volume

        Ext.Manager3D_DeselectAll();
        for (i = 1; i < nb; i++) {
            Ext.Manager3D_Measure3D(i,"Vol",V);
            if(V<100){
                Ext.Manager3D_MonoSelect();
                Ext.Manager3D_Select(i);
                Ext.Manager3D_Delete();
                Ext.Manager3D_Count(nb);
                i=i-1;
            }
        }

// measure distances
        Ext.Manager3D_Count(nb_obj);
        for (i = 1; i < nb_obj-1; i++) {
            Ext.Manager3D_Dist2(0,i,"c2b1",dist);
            index = lastIndexOf(file, "_");
            end = lastIndexOf(file, "/");
            if (index!=-1) type = substring(file, 0, index);
            if (index!=-1) series = substring(file, index + 1, end);
            n = nResults();
            setResult("Type",n,type);
            setResult("Series",n,series);
            setResult("Variable",n, "TC-Centroid");
            setResult("Value",n, dist);
        }

        Ext.Manager3D_Close();
        close("SpheroCentroid.tif");
        close("TCObjects.tif");
    }
}

```

11.3 MSC attachment to tumor spheroids depends on tumor cell line

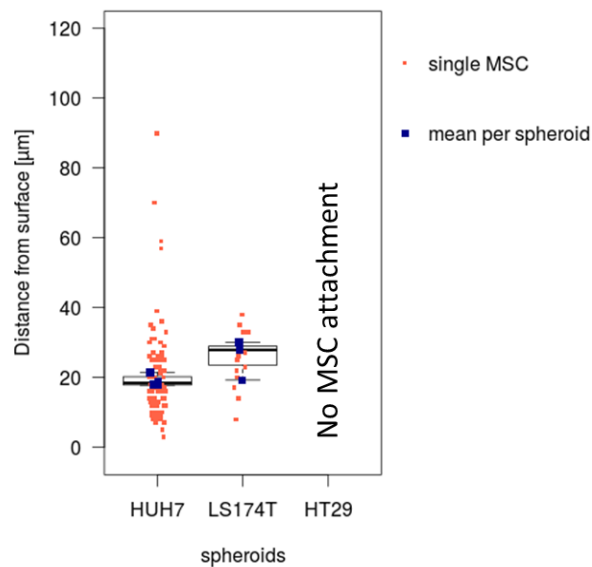


Figure 26 Invasion potential of primary bone marrow-derived MSCs into different tumor spheroids. Invasion was evaluated with CMFDA stained MSCs that invaded spheroids from human hepatocellular carcinoma HUH7 cell line and the human colorectal adenocarcinoma lines LS174T and HT29. Spheroids were grown on polyHEMA to a size of approximately 300 µm diameter. Invaded spheroids were fixed after 24 h, stained with 7-AAD and analyzed via nuclear single cell segmentation and measurement of the shortest distance of each MSC to the spheroid surface. Three spheroids per condition were analyzed. Red scatterplots show distant measurements of single MSCs, blue scatterplots depict mean distances per spheroid and whisker-boxplots their distribution, with boxes showing the quartiles and median values and whiskers the rest of the distribution without outliers.

11.4 Effect of thyroid hormones and tetrac on MSC invasion into tumor spheroids

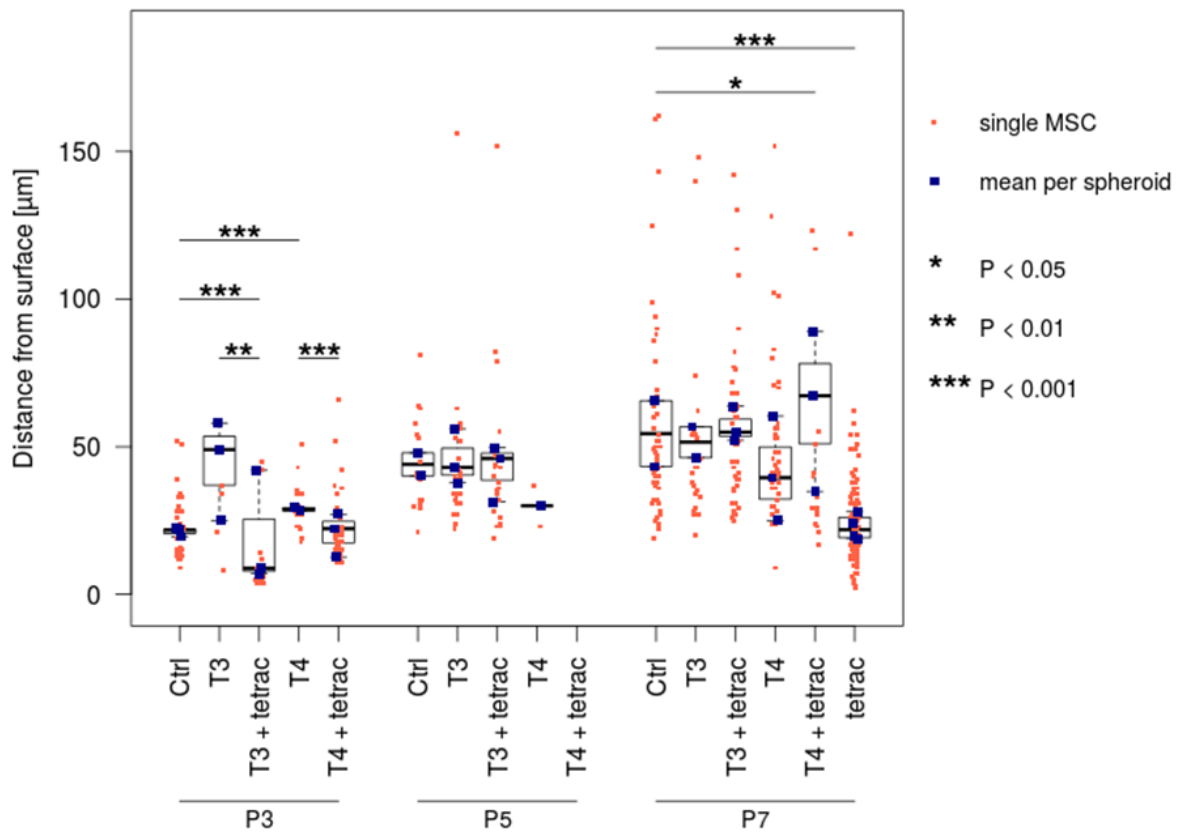


Figure 27 Invasion potential of primary human MSCs (AP99) into HUH7 spheroids upon stimulation with thyroid hormones triiodo-L-thyronine (T3) or L-thyroxine (T4) and integrin $\alpha\beta 3$ inhibitor tetrac. MSCs of passages 3, 5 and 7 were grown for 24 h in DMEM + 10 % charcoal-stripped FCS and stimulated for another 24 h with either 1 nM T3 or 1 μ M T4, with or without 100 nM tetrac. They were CMFDA labeled and invaded for 24 h into HUH7 tumor spheroids grown on polyHEMA with a diameter of about 300 μ m. After invasion they were fixed and imaged using SPIM. Automated analysis of invasion depths was conducted via cytoplasmic segmentation and measurement of the shortest distance of each MSC to the spheroid surface. Red scatterplots show measurements of single MSCs, blue scatterplots depict mean distances per spheroid and whisker-boxplots their distribution, with boxes showing the quartiles and median values and whiskers the rest of the distribution without outliers; Mann-Whitney U test, *p-value < 0.05, **p-value < 0.01, ***p-value < 0.001.

11.5 Effect of chimeric co-stimulatory constructs on CTL cytotoxicity in SKMel23 spheroids - single experiments

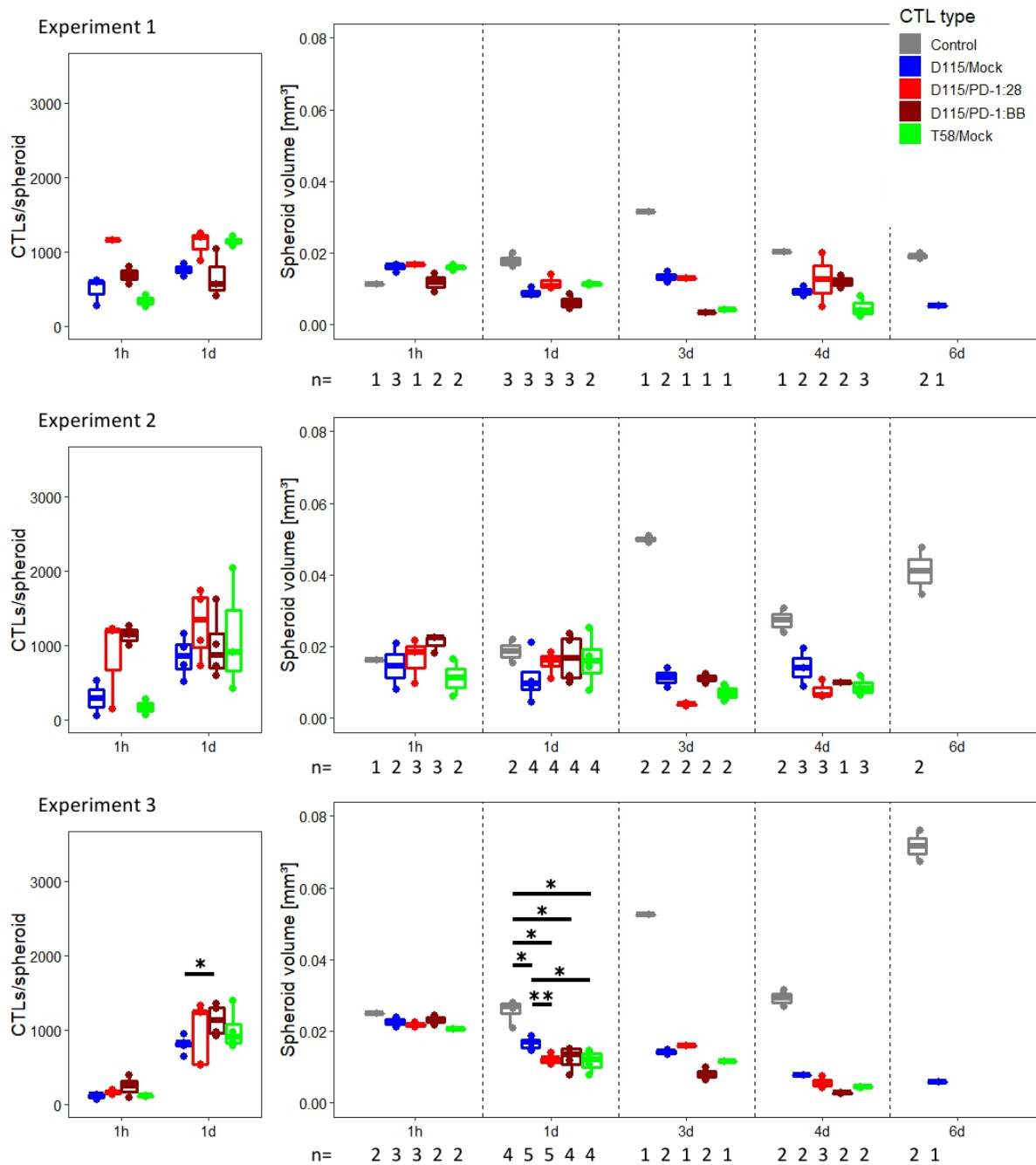


Figure 28 Invasion assay single experiments with chimeric co-stimulatory receptors. Three independent invasion experiments (Experiment 1 – 3) have been conducted as described in **Figure 19** with PD-1:28 and PD-1:BB expressing D115 CTLs in comparison to D115/Mock and T58/Mock CTLs, with a total number of analyzed spheroids per group as indicated (n). Shown are numbers of watershed segmented CTLs per spheroid after 1 h or 1 d invasion and spheroid volumes after incubation for the times indicated; Mann-Whitney U test, * p-value < 0.05, ** p-value < 0.01.

Curriculum Vitae

Name	Svenja Rühland
Address	Brudermühlstraße 34a, 81371 Munich
Date of birth	20.03.1989
Place of birth	Hamburg, Germany
Nationality	German

Education

01/2015 – present	Doctoral studies to obtain the degree Dr. rer. nat. at the Faculty of Medicine, Ludwig-Maximilians University Munich
10/2011 – 08/2014	Master of Science in Biology, Ludwig-Maximilians University Munich, Final mark: 1.49 (very good)
10/2008 – 08/2011	Bachelor of Science in Biology, Ludwig-Maximilians University Munich, Final mark: 1.87 (good)
06/2008	Abitur, Gymnasium Oberhaching, Final mark: 1.4

Publications

Rühland, Svenja; Wechselberger, Alexandra; Spitzweg, Christine; Huss, Ralf; Nelson, Peter J.; Harz, Hartmann; 2015.

Quantification of in vitro mesenchymal stem cell invasion into tumor spheroids using selective plane illumination microscopy.

In *Journal of biomedical optics* 20 (4), p. 40501. DOI: 10.1117/1.JBO.20.4.040501.

Schmohl, Kathrin A.; Müller, Andrea M.; Wechselberger, Alexandra; **Rühland, Svenja**; Salb, Nicole; Schwenk, Nathalie; Heuer, Heike; Carlsen, Janette; Göke, Burkhard; Nelson, Peter J.; Spitzweg, Christine; 2015.

Thyroid hormones and tetrac. New regulators of tumour stroma formation via integrin $\alpha\beta 3$.

In *Endocrine-related cancer* 22 (6), pp. 941–952. DOI: 10.1530/ERC-15-0245.

Schlenker, Ramona; Olguín-Contreras, Luis Felipe; Leisegang, Matthias; Schnappinger, Julia; Disovic, Anja; **Rühland, Svenja**; Nelson, Peter J.; Leonhardt, Heinrich; Harz, Hartmann; Wilde, Susanne; Schendel, Dolores J.; Uckert, Wolfgang; Willimsky, Gerald; Noessner, Elfriede; 2017.

Chimeric PD-1:28 Receptor Upgrades Low-Avidity T cells and Restores Effector Function of Tumor-Infiltrating Lymphocytes for Adoptive Cell Therapy.

In *Cancer research* 77 (13), pp. 3577–3590. DOI: 10.1158/0008-5472.CAN-16-1922.

Data of this thesis have been published and presented as follows:

Tumor Immunology Meets Oncology XIII Workshop, Halle, 2017, poster presentation:

Rühland, Svenja; Schmohl, Kathrin A.; Müller, Andrea M.; Schnappinger, Julia; Spitzweg, Christine; Leonhardt, Heinrich; Harz, Hartmann; Nelson, Peter J.; Nößner, Elfriede.

Therapeutic potential of mesenchymal stem cells and cytotoxic T cells analyzed using tumor spheroids.

Center for Advanced Light Microscopy, Ludwig-Maximilians-University Munich, 2017, science podcast:

Rühland, Svenja; Keller, Erik; Fay, Chris; Bleese, Carolin; Hoerl, David; Nelson, Peter J.; Leonhardt, Heinrich; Harz, Hartmann.

Light Sheet Sheds Light on Tumor Therapy.

Available online: https://www.youtube.com/watch?v=HWt9j_1RXSk&t=3s

Acknowledgements

I am thankful to everyone who supported me during my thesis.

First, I want to thank my supervisor Prof. Peter Nelson for the opportunity to work on this exciting project, for many discussions and always a quick advice.

Thanks go to Prof. Heinrich Leonhardt for the opportunity to use his microscopes, office and lab space as well as consultation. Thanks to Prof. Christine Spitzweg for the fruitful collaboration. And to Prof. Elfriede Nößner, thank you so much for this very exciting second half of my work, for hours of fruitful discussions about science, and life.

Big and special thanks to Dr. Hartmann Harz, who always helped me to focus – at the microscope and in general. I enjoyed our scientific and philosophic discourses, without you it would have been much harder to see this through.

Thanks to all the groups I had the pleasure to work in or collaborate with:

to the AG Leonhardt for accomodating me, with special thanks to my office co-workers Dr. Katharina Thanisch, Dr. Patricia Wolf, David Hörl – with extra special thanks for all the coding – and to Andreas Stengl and Katharina Brandstetter for the lunch and coffee breaks; thank you a lot, Dr. Elisabeth Karg, for all the chats in between, and Elke Hammerbacher, for your lovely presence;

to the AG Nelson, with a big thank to Alexandra Wechselberger who did so much for me to find into the project;

to the apceth crew, for a lot of cells and fruitful discussions;

to the AG Spitzweg, with special thanks to Kathrin Schmohl and Dr. Andrea Müller for our talks in between experiments;

and to the research group of Prof. Nößner at the Helmholtz Zentrum, especially to Julia Schnappinger, Dr. Anna Mendler, Anna Brandl and Barbara Mosetter, for the interesting lab meetings, fruitful collaboration and for always welcoming me warmly.

I also want to thank my former students Simon Dedic, Miriam Rodi, Julia Wolst and Cara Sickinger for being open and interested and giving more than taking from me.

I thank my parents for being supportive, understanding and so very relaxed all the years.

Thanks to my siblings Stefan, Jana and Sina, who are the best family I could imagine. And thank you Jonathan for being who you are.

Affidavit

Rühland, Svenja

I hereby declare that the submitted thesis, entitled

“3D imaging and analysis of human mesenchymal stem cells and cytotoxic T lymphocytes invading tumor spheroids”

is my own work. I have only used the sources indicated and have not made unauthorized use of services of a third party. Where the work of others has been quoted or reproduced, the source is always given.

I further declare that the submitted thesis or parts thereof have not been presented as part of an examination degree to any other university.

Munich, 11.01.2019

Place, date

Svenja Rühland

Doctoral candidate